

Electronic Thesis and Dissertation Repository

11-15-2016 12:00 AM

Evaluation System for Craniosynostosis Surgeries with Computer Simulation and Statistical Modelling

Jing Jin

The University of Western Ontario

Supervisor

Roy Eagleson

The University of Western Ontario

Graduate Program in Biomedical Engineering

A thesis submitted in partial fulfillment of the requirements for the degree in Doctor of Philosophy

© Jing Jin 2016

Follow this and additional works at: <https://ir.lib.uwo.ca/etd>



Part of the [Other Biomedical Engineering and Bioengineering Commons](#)

Recommended Citation

Jin, Jing, "Evaluation System for Craniosynostosis Surgeries with Computer Simulation and Statistical Modelling" (2016). *Electronic Thesis and Dissertation Repository*. 4248.

<https://ir.lib.uwo.ca/etd/4248>

This Dissertation/Thesis is brought to you for free and open access by Scholarship@Western. It has been accepted for inclusion in Electronic Thesis and Dissertation Repository by an authorized administrator of Scholarship@Western. For more information, please contact wlsadmin@uwo.ca.

Abstract

Craniosynostosis is a pathology in infants when one or more sutures prematurely closes, leading to abnormal skull shape. It has been classified according to the specific suture that has been closed, each of which has a typical skull shape. Surgery is the common treatment to correct the deformed skull shape and to reduce the excessive intracranial pressure. Since every case is unique, cranial facial teams have difficulty selecting an optimum solution for each specific patient from multiple options. In addition, there is no standard quantified measurement to help cranial facial teams to evaluate their surgeries.

We aimed to develop a head model of a craniosynostosis patient which allows neurosurgeons to practice any potential surgeries so as to simulate postoperative head development. Our model allows neurosurgeons to foresee the potential surgical results and select the optimal approach. In this thesis, we have developed a normal head model, and built mathematical models for possible dynamic growth. We also modified this model by closing one or two sutures to simulate common types of craniosynostosis. The abnormal simulation results showed a qualitative match with real cases and the normal simulation indicated a higher growth rate of the cranial index than clinical data. We believe that this discrepancy was caused by the rigidity of our skull plates, which will be adapted to deformable skull models in the future.

In order to help neurosurgeons better evaluate any surgery, we hope to develop an algorithm to quantify the level of deformity of a skull. We have designed a set work flow and targeted curvatures as the primary variable. A training data was carefully selected to search for an optimal system to characterize different types of shapes. A set of test data was used to

validate our algorithm to assess the performance of the optimal system. With a stable assessment system, we can evaluate a surgery by comparing the preoperative and postoperative skull shapes of a patient. A surgery can be considered effective when the postoperative skull has shifted toward a normal shape.

Keywords

Craniosynostosis, computer simulation, virtual reality, skull development, skull shape measurement, surgical evaluation.

Acknowledgments

I would first and foremost like to thank my supervisors Prof. Roy Eagleson and Dr. Sandrine de Ribaupierre. During my Ph. D and master, they have always provided constructive and invaluable ideas to lead me progress in my research. I would also like to acknowledge them for dedicating their valuable time for having weekly meetings, always providing positive feedbacks to any of my work so as to encourage me toward progressing my thesis. In addition, I would be appreciated that they provide me a good study atmosphere with a well equipped office and nice group mates (Arezoo Tony, Trinette Wright and Ryan Armstrong), from which we are able to help and learn from each other.

I would also like to thank John Lloyd from University of British Columbia for his great support in providing information and technical help on the simulation software Artisynth they have developed. It is very generous to share their valuable research experience and let us to use their updated research outcome.

At the end, I would like to thank to Jonason Lau, who contributed his time on collecting CT scans of their craniosynostosis patients for me. These are valuable data for me to support me develop our machine learning algorithm that measures skull shapes.

Table of Contents

Abstract.....	i
Acknowledgments.....	iii
Table of Figures	viii
Table of Equations	xviii
Chapter 1.....	1
1 Introduction.....	1
1.1 Overview.....	1
1.2 Normal Head Development	2
1.2.1 The Anatomy of Skull.....	2
1.2.2 Development of Cranial Bones	5
1.2.3 Cranial Sutures and Closure.....	9
1.3 Craniosynostosis: The Abnormality of Skull Development	12
1.3.1 Overview.....	12
1.3.2 Types of Craniosynostosis	13
1.3.3 Current Treatment Methods	16
1.4 Medical Imaging	18
1.4.1 Overview.....	18
1.4.2 Radiography	18
1.4.3 Computer Tomography (CT)	19
1.4.4 Digital Imaging and Communication in Medicine (DICOM)	19
1.5 Previous Work.....	20
1.5.1 Overview.....	20
1.5.2 Surgical Evaluation Tool for Craniosynostosis	20
1.5.3 Finite Element Analysis of Craniosynostosis Adjustment.....	21

1.5.4	Automated Diagnosis of the Types of Craniosynostosis	22
1.5.5	Statistical Model to Predict Craniosynostosis by the Snake Algorithm ...	23
1.6	Thesis Rationale.....	24
1.6.1	Motivation.....	24
1.6.2	Hypothesis and Objectives.....	25
1.6.3	Outline.....	27
Chapter 2	29
2	Head Development Simulation with Pressure Based Hybrid Model	29
2.1	Overview.....	29
2.2	Framework of Our Simulation System	29
2.3	Simulation Software: Artisynth	32
2.4	The Generation of a Head Model.....	33
2.5	Mechanical Properties Setup.....	42
2.6	Dynamic Simulation for Each Object.....	45
2.6.1	Brain Expansion.....	45
2.6.2	Suture Stretch.....	47
2.6.3	Skull Extension	49
2.7	Set Land Markers On the Skull.....	60
2.8	Results.....	61
2.8.1	Simulations with Only Brain Expansion.....	61
2.8.2	Simulations with Skull Plates Extension Added	66
2.8.3	Results Discussion	76
Chapter 3	77
3	Head Development Simulation with Force Based Model	77
3.1	An Alternative Simulation System	77

3.1.1	Algorithm Specification.....	77
3.1.2	Parameter Specifications.....	78
3.2	Results.....	80
3.2.1	Anterior Plagiocephaly	80
3.2.2	Normal Head Development	86
3.2.3	Scaphocephaly	90
3.2.4	Trigonocephaly	94
3.3	Discussions	97
3.4	Conclusions and Future work	102
Chapter 4.....		104
4	Evaluation Tool for Craniosynostosis Surgery	104
4.1	Overview.....	104
4.2	Curvatures in Differential Geometry	105
4.2.1	Curves and Surfaces.....	106
4.2.2	The First Fundamental Form.....	108
4.2.3	The Second Fundamental Form.....	109
4.2.4	Normal curvature	110
4.2.5	Principal curvatures.....	112
4.2.6	Gauss Map and Weingarten Map	116
4.3	Estimation of Curvatures for Discrete Surface	120
4.3.1	Curvature Estimation Review	121
4.3.2	Gauss Bonnet Scheme.....	125
4.3.3	Algorithm of Curvature Estimation	126
4.4	Skull Shape Evaluation Tool utilizing Statistical Modeling.....	130
4.4.1	Material Preparation.....	132

4.4.2	Skull segmentation and surface generation.....	133
4.4.3	Intracranial Volume Normalization	135
4.4.4	Curvature Distribution for One Skull Shape.....	137
4.4.5	Statistical Modeling	139
4.5	Results of Evaluating System	141
4.5.1	System Optimization.....	142
4.5.2	Result Discussions	158
4.5.3	Surgical Assessments	162
4.5.4	Conclusions and Future Work.....	169
Chapter 5	172
5	Conclusion.....	172
5.1	Overview.....	172
5.2	The Simulation of Head Development.....	172
5.3	Skull Shape Measurements	174
References	177
Appendices	185
Curriculum Vitae	189

Table of Figures

Figure 1.1: The left view of the anatomy of an adult skull	3
Figure 1.2: The outside appearance of an mature occipital bone.....	4
Figure 1.3: Infant skull anatomy from both right and top views	7
Figure 1.4: Cartilaginous bone in the cranial base is derived from mesodermal sclerotome in blue and neural crest cells in red.....	9
Figure 1.5: Infant suture and fontanelle distributions	10
Figure 1.6: Common types of craniosynostosis. The left top skull was scaphocephaly, the right top skull was trigonocephaly, the left bottom skull was brachycephaly, and the right bottom one was anterior plagiocephaly.	15
Figure 2.1: Unit shapes that are alternative to form volumetric mesh.....	30
Figure 2.2: The flow chart of the procedure of our head development simulation.....	31
Figure 2.3: A screenshot of the GUI of Artisynth.....	33
Figure 2.4: A slice of CT scans for the normal baby, using automatic segmentation method in Amira to label out the skull bone with light blue color.	35
Figure 2.5: A slide of the CT scans from the normal baby. We use 100 as the threshold value to label out the skull structure out of the head, using different color to indicate different skull plate.....	37

Figure 2.6: Surface model of a normal head, generated according to segmentation labels. Different color indicates different skull plates..... 38

Figure 2.7: The volumetric mesh of a simplified and smoothed brain 39

Figure 2.8: Skull plates were imported in the Artisynt, with gaps between each two plates. 40

Figure 2.9: The suture model was indicated with blue color, manually generated with hexahedral meshes. 41

Figure 2.10: An indication of sutures that secrete cartilaginous bone cells. These types of suture have higher values of Young's modulus. 42

Figure 2.11: The development of circumferences of babies aged within 36 months, where the horizontal-axis represent the age with respect to months, and the vertical-axis indicates the values of circumferences with unit of centimeter (cm)..... 46

Figure 2.12: Green spheres in this Figure were nodes that were attached onto the closest skull surface whereas red spheres were not attached to any surface. 48

Figure 2.13: This Figure indicates that while the brain volume is expanding, the skull plates at the suture side are leaving from each, leading to the stretchiness of the suture. 49

Figure 2.14: This Figure shows two ways to expand a skull plate. Left one indicates that the plate was cut at the edge, and make new mesh to fill in, whereas the right one shows to scale the skull plates to achieve the same effect. 51

Figure 2.15: A skull plate using one sphere to explore the edge. The width of the edge at the top and bottom is too thick to be accepted. 53

Figure 2.16: The skull plate that connected with cranial facial. The red points on the bone plate indicates this skull edge..... 53

Figure 2.17: Illustration of skull edge of right front bone. The red points denote the vertices we added into the edge list. 54

Figure 2.18: An indication of suture stretch. The six blue squares are part of suture, and the dashed line shows the stretch of the suture. 56

Figure 2.19: An indication that changes of the width of a suture could be variant under some circumstances. 56

Figure 2.20: The attached suture nodes in green are the centers of each sub-regions. In order to make this picture clear, we make other plates invisible except this right frontal bone. 58

Figure 2.21: The suture shrink back to normal size along the direction of the tension exerted on it. The blue squares are represented as the cross-sectional view of the suture, where the shapes outlined with black lines indicated as skull plates. 59

Figure 2.22: Six reference markers are set on our normal skull model, to calculate the skull width, length, and height. The six markers are indicated as red spheres, located at the left, right, front, back, top and bottom of the skull respectively. 61

Figure 2.23: The length, width, height and volume measurement with respect to time during brain-skull growth. Left Y-axis represented the scale of skull with unit of millimeter (mm),

right Y-axis indicated the volume of the skull with unit of dm^3 , and x-axis represented time with seconds.....	63
Figure 2.24: The values of cranial index over time during the simulation, which is the relation between skull width and skull length.....	64
Figure 2.25: A screen shot of our head model in the middle of the simulation with color map of stress showing minimum as no tension to maximum as red.....	65
Figure 2.26: A screen shot of our normal head model at the end of the simulation.	66
Figure 2.27: Original status of our normal skull model, and the brain model was placed inside the skull. The red spheres are reference markers.	67
Figure 2.28: A deformation of our head model at the end of our simulation, left indicated from top view, and right displayed from front view.	68
Figure 2.29: A screen shot of our normal head model in the end of the simulation, left showed from left view, and right indicated from back view.	68
Figure 2.30: The values of cranial index calculated at each time intervals during the simulation, where x-axis represented time in seconds, y-axis denoted cranial index.	70
Figure 2.31: The original status of our scaphocephaly model, where the sagittal suture is closed.	71
Figure 2.32: A screenshot of our scaphocephaly at the end of the simulation, showing a long head shape.	72

Figure 2.33: Cranial index values of the simulation of scaphocephaly.	72
Figure 2.34: Initial status of our trigonocephaly where the frontal suture was closed.	74
Figure 2.35: The result of the simulation with closed frontal suture.	74
Figure 2.36: Cranial index values during the simulation of trigonocephaly model.....	75
Figure 2.37: a) Initial plagiocephaly model. b) Plagiocephaly model in the middle of simulation.....	76
Figure 3.1: An indication of the relationship between face normal and the force fo'i.....	78
Figure 3.2: a) One of the suture that was segmented from original model, crossing the cranial facial bones. b) The other suture we segmented, located at the cranial base.....	80
Figure 3.3: Initial model of anterior plagiocephaly by closing the right side of coronal suture.	81
Figure 3.4: Top view of our plagiocephaly model in the end of the simulation, the opened frontal bone was protruded while the affected side remained original status.	82
Figure 3.5: Front view of our initial plagiocephaly model.	83
Figure 3.6: Front view of the result from plagiocephaly simulation.	84
Figure 3.7: The scales of the skull during the simulation of plagiocephaly head development.	85
Figure 3.8: Cranial indices during the simulation of anterior plagiocephaly.....	85

Figure 3.9: Top view of our normal head model, left presented the initial status and right was captured in the middle of the simulation. 86

Figure 3.10: Front view of our normal head model, left presented the initial status and right was captured in the middle of the simulation. 87

Figure 3.11: Side view of our normal head model, left presented the initial status and right was captured in the middle of the simulation. 87

Figure 3.12: The scales of the skull during the simulation of normal head development. 89

Figure 3.13: Cranial indices with respect to time during the normal head development simulation. 89

Figure 3.14: Top view of our scaphocephaly head model, left presented the initial status and right was captured in the middle of the simulation. 90

Figure 3.15: Front view of our scaphocephaly head model, left presented the initial status and right was captured in the middle of the simulation. 91

Figure 3.16: Side view of our scaphocephaly head model, left presented the initial status and right was captured in the middle of the simulation. 91

Figure 3.17: The scales of the skull during the simulation of scaphocephaly head development. 93

Figure 3.18: Cranial indices with respect to time during the scaphocephaly head development simulation. 93

Figure 3.19: Top view of our trigonocephaly head model, left presented the initial status and right was captured in the middle of the simulation. 94

Figure 3.20: Front view of our trigonocephaly head model, left presented the initial status and right was captured in the middle of the simulation. 95

Figure 3.21: Side view of our trigonocephaly head model, left presented the initial status and right was captured in the middle of the simulation. 95

Figure 3.22: The scales of the skull during the simulation of scaphocephaly head development. 96

Figure 3.23: Cranial indices with respect to time during the trigonocephaly head development simulation. 97

Figure 3.24: Cranial index statistics from (Likus et al. 2014) 98

Figure 3.25: Top view of normal head model during the simulation with deformable skull plates. 101

Figure 3.26: Side view of normal head model during the simulation with deformable skull plates. 101

Figure 4.1: This is the flow chart of our statistical modeling, where $\omega_{1,2,3}$ will be adapted while more input data are involved in the training. 132

Figure 4.2: Curvature distributions of patients that from various types of skull shapes. 139

Figure 4.3: Results from training data, which the number of faces of each surface mesh is 50000.....	144
Figure 4.4: Quantified results with the second mesh simplification method, which reduces the number of faces to the limitations.	145
Figure 4.5: NRK vs cranial index with different skull shapes, which number of faces were halved four times.....	146
Figure 4.6: NRK vs cranial index with different skull shapes, which number of vertices were at the same level.....	146
Figure 4.7: Skulls without normalization.....	147
Figure 4.8: The measurements of skull shapes with bin=0.0005.....	148
Figure 4.9: The measurements of skull shapes with bin=0.001.....	149
Figure 4.10: The measurements of skull shapes with bin=0.01.....	149
Figure 4.11: The measurements of skull shapes with bin=0.004.....	150
Figure 4.12: The measurements of skull shapes with bin=0.005.....	151
Figure 4.13: The measurements of skull shapes with bin=0.006.....	151
Figure 4.14: The measurements of skull shapes with bin=0.008.....	152
Figure 4.15: The measurements of skull shapes from test data with bin=0.005.....	153
Figure 4.16: The measurements of skull shapes from test data with bin=0.008.....	154

Figure 4.17: The quantified results of skull shapes with new data added.	156
Figure 4.18: Top view of trigonocephaly skulls, the left one is a typical shape and the right one is an untypical case.....	156
Figure 4.19: Side view of trigonocephaly skulls, the left one is a typical shape and the right one is an untypical case.....	157
Figure 4.20: Comparison of skull shapes from top view, the left one is from a brachycephaly patient and the right one is from plagiocephaly case 1.	157
Figure 4.21: Comparison of skull shapes from top view, the left one is from plagiocephaly case 1 and the right one is plagiocephaly case 2.	158
Figure 4.22: An indication of expected areas of shape results for each type of skull shapes.	161
Figure 4.23: A comparison of local shapes between two scaphocephaly patients (right is case 1 and left is case 2), indicated by color map of curvature values showing from blue as 0 to red as higher than 0.1.	162
Figure 4.24: Surgical evaluation of a scaphocephaly case with one preoperative and one postoperative skull shapes.	164
Figure 4.25: Surgical evaluation of another scaphocephaly patient with one preoperative and one postoperative skull shapes.	164
Figure 4.26: Surgical evaluation of a trigonocephaly patient with one preoperative and one postoperative skull shapes.	165

Figure 4.27: Surgical evaluation of a brachycephaly patient with one preoperative and one postoperative skull shapes.....	166
Figure 4.28: Surgical evaluation of a plagiocephaly patient with one preoperative and one postoperative skull shapes.....	167
Figure 4.29: Surgical evaluation of another plagiocephaly patient with one preoperative and one postoperative skulls.....	168
Figure 4.30: Skull shapes with color map of curvature values, showing from blue as 0 to red as higher than 0.1. The left skull was taken preoperatively and the right one was postoperative.....	168
Figure 4.31: Top view of two scaphocephaly skull model.....	170

Table of Equations

Equation 2.1: Brain center calculation.	47
Equation 2.2: The position of brain nodes updating equation over time.	47
Equation 3.1: The calculation of forces applied on the interior surface of skull.	78
Equation 4.1: The expression of a surface by two parameters.....	106
Equation 4.2: The definition of a space curve on a surface.	107
Equation 4.3: The definition of tangent vector on a surface.	107
Equation 4.4: The expression of the tangent surface at a given location of a surface.	107
Equation 4.5: The distance calculation between two points on the surface that is infinitely close to each other.....	108
Equation 4.6: The approximation of the arc length between two close points on the surface.	108
Equation 4.7: The first fundamental form.....	109
Equation 4.8: The expression of first fundamental form in matrix.	109
Equation 4.9: The second fundamental form.	110
Equation 4.10: The matrix expression of the second fundamental form.	110
Equation 4.11: The unit tangent vector interpreted with respect to arc length.	111

Equation 4.12: The definition of curvature.	111
Equation 4.13: The definition of normal curvature.....	111
Equation 4.14: The normal curvature with respect to the fundamental forms.....	112
Equation 4.15: An alternative way to express normal curvature.	112
Equation 4.16: The normal curvature expression at extreme values.	112
Equation 4.17: The relationship between the coefficients at extreme values.	113
Equation 4.18: Extended expression of normal curvature at extreme values.	113
Equation 4.19: The quadratic equation of normal curvature at extreme values.	113
Equation 4.20: Gaussian curvature.	114
Equation 4.21: Mean curvature.	114
Equation 4.22: Principal curvatures.	114
Equation 4.23: Gauss map.	116
Equation 4.24: The tangential map derived from the Gauss map.	116
Equation 4.25: The definition of Weingarten map.	117
Equation 4.26: The projection of tangent vector by Weingarten map.	117
Equation 4.27: The second fundamental form represented by Weingarten map.	117
Equation 4.28: The normal vector interpreted by Weingarten map.....	117

Equation 4.29: The relationship between the principal curvatures and any normal curvature on a given location of a surface.	118
Equation 4.30: The definition of the shape operator.....	119
Equation 4.31: The relationship between Gaussian curvature and the shape operator.	119
Equation 4.32: The interpretation of Gaussian curvature with respect to Gauss map.	120
Equation 4.33: An alternative way to calculate the value of Gaussian curvature.	120
Equation 4.34: The estimation of normal for each vertex.	127
Equation 4.35: The estimation of normal curvature.	128
Equation 4.36: The calculation of the tangent vector associated with a specific normal curvature.....	128
Equation 4.37: The expression of normal curvature with a given coordinate system.	129
Equation 4.38: The estimation of Gaussian, Mean and Principal curvatures.	130
Equation 4.39: The calculation of the centroid of the skull model.	136
Equation 4.40: The normal vector of the sagittal plane.	136
Equation 4.41: The formula to check whether a vertex in on the sagittal plane.	137
Equation 4.42: The definition of mean.	140
Equation 4.43: The expression of variance.	140

Equation 4.44: The equation to calculate skewness.....	140
Equation 4.45: The definition of kurtosis	141

Chapter 1

1 Introduction

1.1 Overview

During the first year of human life, an infant's skull develops from several pieces, connected with each other by a type of soft tissue, which plays a key role in the development of the skull. The gap between each of two skull plates is referred to as one suture. During the first year, sutures are ossified one by one at different times. Each suture is closed until finally the skull is combined into one piece. The timing of the closing sutures determines how the skull will be shaped. However, there is a pathology that occurs in infants wherein one or more sutures are closed prematurely, leading to a malformed skull shape. Given the importance of appearance and proper neurological development, surgery is a regular treatment to attempt to correct the skull shape.

In this chapter, we will first introduce how the skull and sutures are formed while in utero and how they develop in the first year after birth. Next, we will introduce craniosynostosis, including the types, the causes, and treatments. Studies by other research groups that try to facilitate neurosurgeons' performance of surgeries for craniosynostosis will be discussed. Finally, we will explain the structure of our two projects intended to improve the surgical treatment of craniosynostosis and how it differs from other approaches.

1.2 Normal Head Development

The skull plates of an infant start to develop while in utero, and the sutures are formed a few weeks before delivery. Approximately six months after delivery, the sutures start to close, which begins to secure the skull shape. In this section, we will first briefly introduce the anatomy of a skull, our primary interest is with the cranium, including its development from several pieces above the brain. Subsequently, the formation of sutures will be discussed, as well as the role they play in establishing skull shape during infancy.

1.2.1 The Anatomy of Skull

The human skull is a bony structure supported by the spinal column, and is composed of two parts, the cranium and the facial skeleton (Clemente 1985; Larsen 2002). In our research, we are only concerned with the cranium. The cranium of an adult, which protects the brain, consists of eight skull plates: the occipital, frontal, sphenoidal, and ethmoidal, left and right parietal, and left and right temporal respectively. All these plates are joined together by sutures, which are classified as rigid articulations that rarely allow movements in adults (Ellis and Mahadevan 2010; Hartwig 2008). Figure 1.1 below shows the left view of an adult skull, where most of the cranial plates and sutures are illustrated.

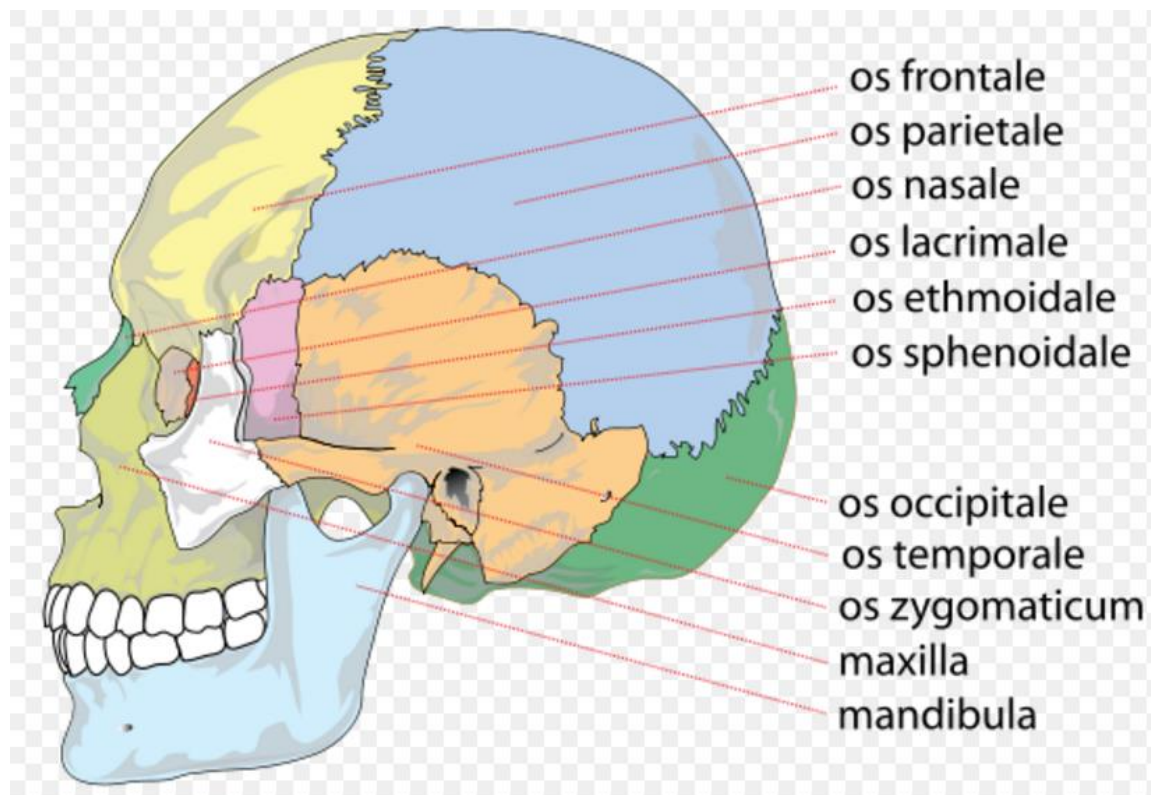


Figure 1.1: The left view of the anatomy of an adult skull

[https://en.wikipedia.org/wiki/Skull#/media/File:Human_skull_side_bones.svg]

The occipital bone (shown in Figure 1.2), located at the back and inferior part of the cranium, has a large aperture called the foramen magnum, which translates to big hole, where the vertebral canal connects to the skull (Larsen 2002). The occipital bone consists of four parts. With reference to the foramen magnum, the squama portion is a scale shaped plate above this hole, developed from membrane, while the basilar part is beneath the hole and the lateral parts are on either side. With the exception of the squama, the other parts are derived from cartilage.

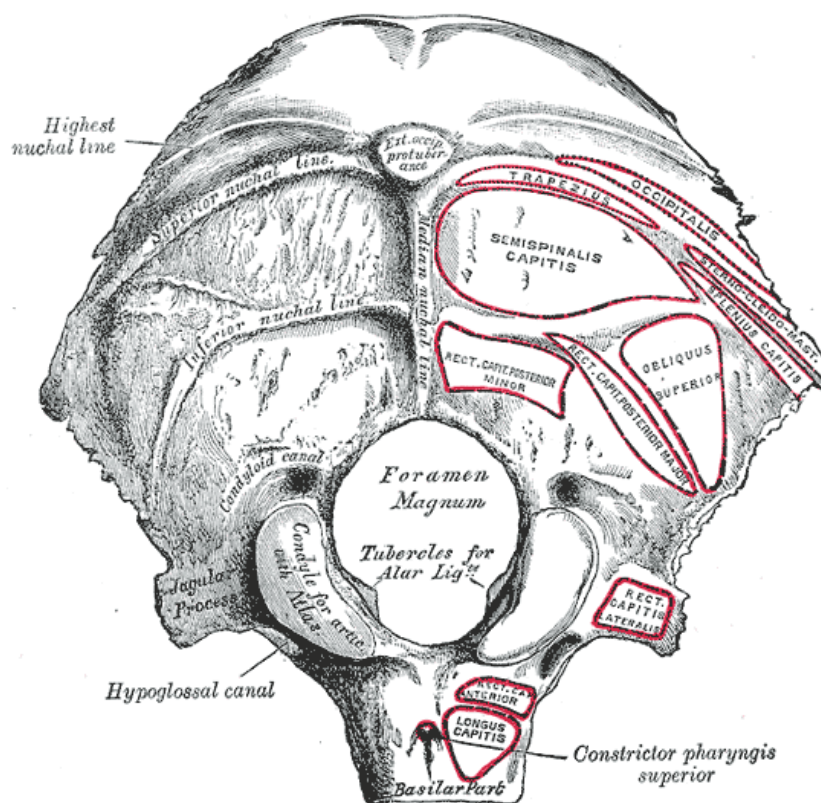


Figure 1.2: The outside appearance of an mature occipital bone

[https://en.wikipedia.org/wiki/Occipital_bone#/media/File:Gray129.png]

The frontal bone is composed of three structures: the forehead, the top of the eye sockets, and the forepart of the cranial roof. It is separated by the frontal suture into left and right parts at the very beginning of human life, which is fused after the second month of fetal development, and disappears by age 6-8 (Tortora and Nielsen 2010).

The two temporal bones constitute the bottom of the cranial sides and part of the cranial base. Each temporal bone is categorized into five parts according to its anatomical structure: squama, petrous, mastoid, tympanic, and the styloid process. At the end of fetal growth, each temporal bone has three major portions: the squama, which is a relative flat and orbicular shaped bone derived from membrane; the petromastoid portion, developed

from cartilage in the ear capsule; and the tympanic ring, to which the tympanic membrane is attached. The styloid process is formed after birth.

The larger part of the cranium sides and roof consist of two parietal plates, each of which looks like an irregular quadrilateral with four borders and two surfaces (Hartwig 2008). At the center of the cranial cavity is the sphenoid bone, which is called the "keystone of the cranial floor" because it associates with all the other bones in the cranium (Tortora and Nielsen 2010). Its shape is similar to a bat with two pairs of extended wings (greater wings and lesser wings). The ethmoid bone is situated in the middle of the anterior cranial base and between the two eye sockets, constituting the roof of the nose (Ellis and Mahadevan 2010). It is an extremely light weight and porous structure (Clemente 1985).

1.2.2 Development of Cranial Bones

The human cranium is composed of two different bone tissues, which categorize the cranium into two parts: intramembranous bone is the cranial vault or calvaria (which includes the roof and sides of the neurocranium and the face) and cartilaginous bone which is the cranial base (called chondrocranium) (Moss 1954). These two essential components of bone tissue are created during fetal development (Dye 2000; Steinbock 2011).

The cranium is formed from mesenchymal cells, which first appear as membrane enclosing the growing brain (Sperber, Sperber, and Guttman 2010). This membrane contains two layers: the internal layer, known as the endomeninx, which is derived from the neural crest cells; and the external layer known as the ectomeninx, which is derived

from both the paraxial mesodermal and neural crest cells. The endomeninx gives rise to two further layers: the pia mater and the arachnoid that cover the brain. The ectomeninx also forms two distinct layers: the unossified internal dura mater that covers the brain and an external membrane, which either ossifies into bones at the cranial vault, or condries into cartilage at the cranial base. The structure of the membrane is shown in the following Figure 1.3. The dura mater that encircles the brain prevents the brain from developing into a complete sphere, and acts as the endocranial periosteum, which also affects the shape of the cranial vault. Some researchers have also pointed out that dura mater is necessary for intramembranous bone formation, by serving a role in ossification induction (Opperman 2000).

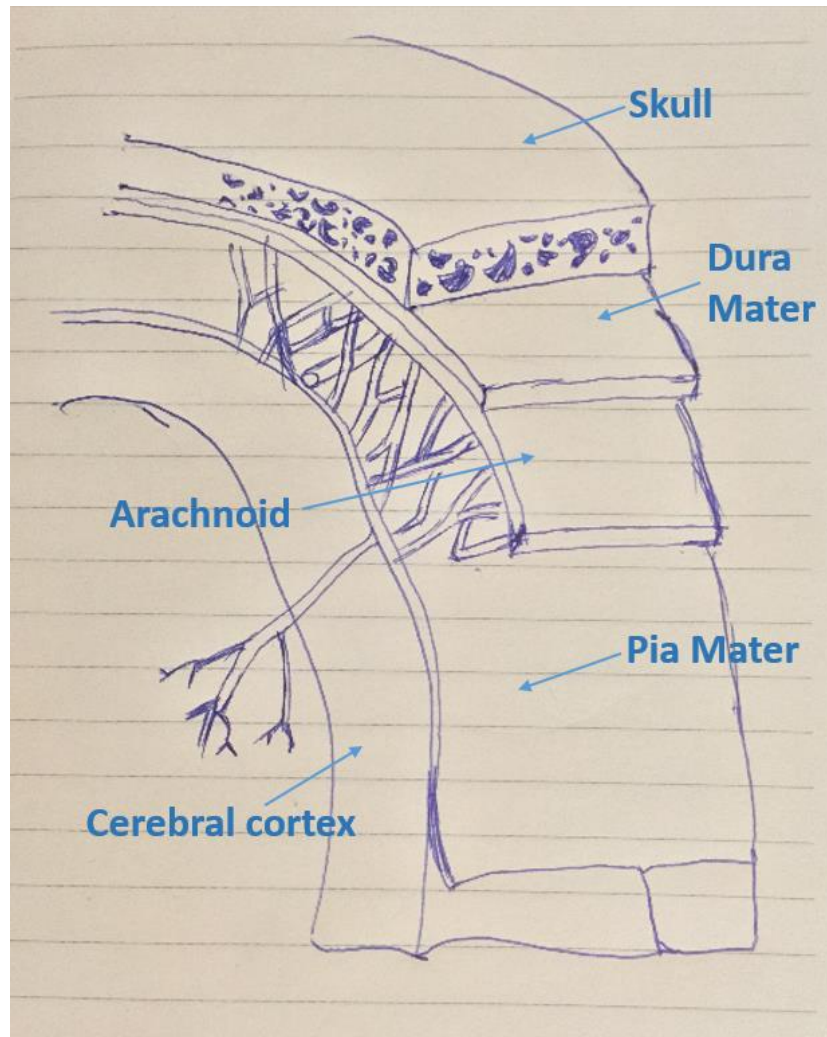


Figure 1.3: Infant skull anatomy from both right and top views

On the external layer of the ectomeninx, several primary and secondary ossification centers are formed and spread out as individual flat bones (Moore, Persaud, and Torchia 2011). The ectomeninx originates from two different sources, the mesodermal cells which form major parts of the frontal, parietal, sphenoid, petrous temporal and occipital bones, and the neural crest cells, which give rise to the squamous, temporal, lacrimal, nasal, zygomatic bones, etc... (Sperber, Sperber, and Guttman 2010). Around eight-weeks post conception (pc), two single primary ossification centers form at the left and

right superciliary arch and ossify into the left and right frontal bones. Secondary centers subsequently arise at each side of the zygomatic processes, nasal spine, and trochlear fossae, then fuse together with each primary frontal center. Each of the parietal bones emerge from two primary ossification centers at eight-weeks pc, which fuse together after two months. The squamous part of the temporal bone develops from solitary centers, whereas the tympanic ring develops from four. The fusion of these two parts occurs at birth, while the rest of the temporal bone develops from cartilage. Although most of the ossification centers arise around the seventh and eighth week pc, the outward extension of the ossification continues after birth.

At the fourth week pc, mesenchyme aggregates around the notochord that is beneath the hindbrain, beginning to form the floor of the external layer of ectomeninx. The notochord is formed during the embryonic stage, and will form the midline axis as well as play a role inducing the development of surrounding tissues. The sella turcica is a saddle-shaped region of the sphenoid bone of the human skull and contains the pituitary fossa at its centre (shown in Figure 1.4). Bones located anterior to this point are formed by neural crest cells, which labeled in blue in Figure 1.4, whereas bones posterior to it, indicated in red in Figure 1.4, are formed by the mesodermal sclerotome. The condrocranium also begins from separated cartilage centers, which occur at certain locations and periods, then fuse together to form either entire or partial plates of the cranial bones. For example, the sphenoid, and the ethmoidal bones are entirely formed from cartilage, whereas the only base of the occipital plate, the petrous and mastoid parts of the temporal plate are formed by cartilage.

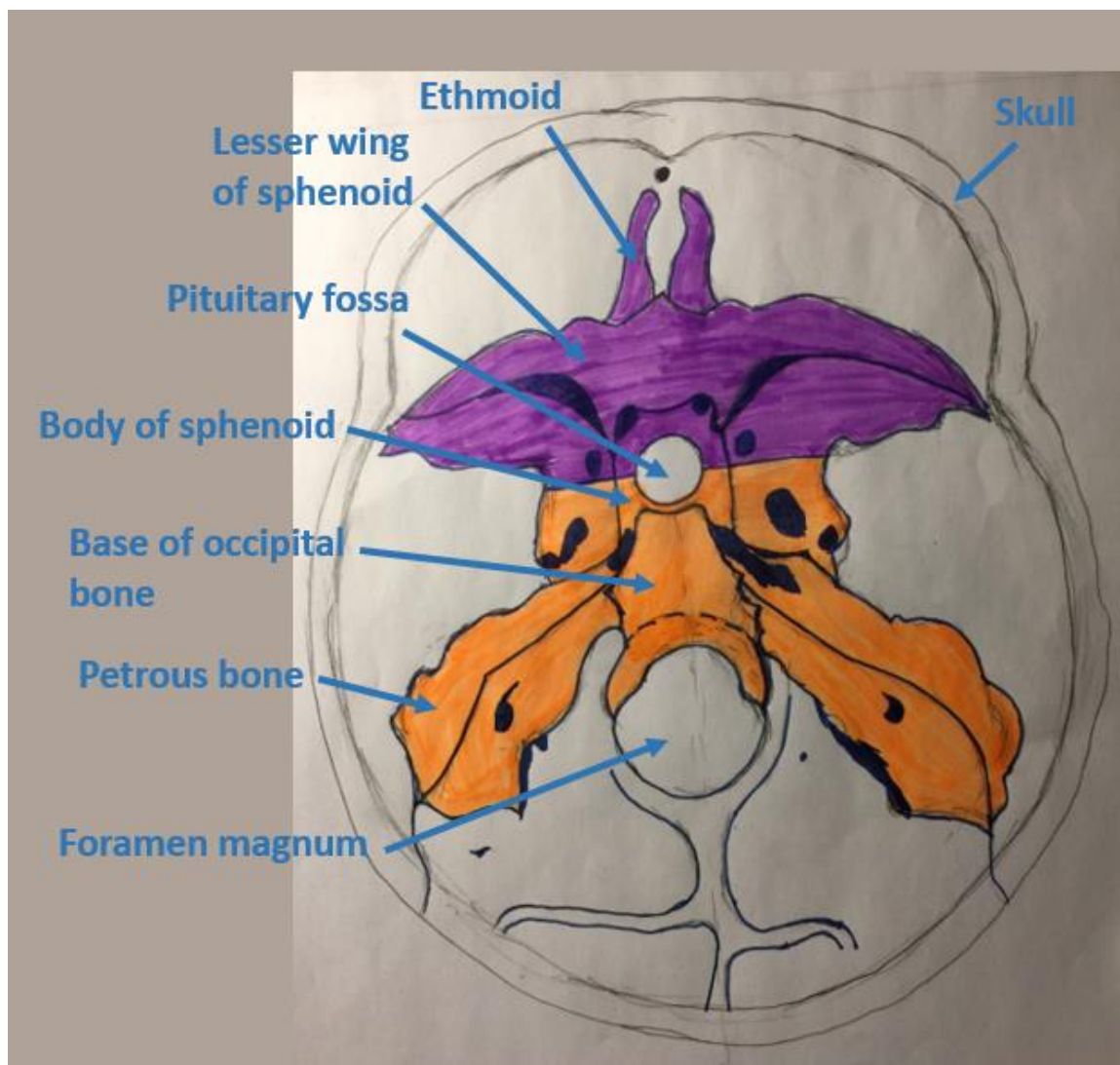


Figure 1.4: Cartilaginous bone in the cranial base is derived from mesodermal sclerotome in blue and neural crest cells in red

[<http://skeletalsystemdev.weebly.com/development-of-skull.html>]

1.2.3 Cranial Sutures and Closure

Although the ossification of intramembranous bones spreads out after each primary center appears, these bones become broadly separated because of the faster growth of the brain. After brain expansion slows down, the bones approach each other as ossification

continues. The mesenchyme between the bones is induced by underlying dura mater to develop fibrous tissues, named sutures, but only when two bone fronts are close enough to each other. A similar process occurs with the development of fontanelles, though they consist of an interface of more than two bones (Opperman 2000; Moss 1954).

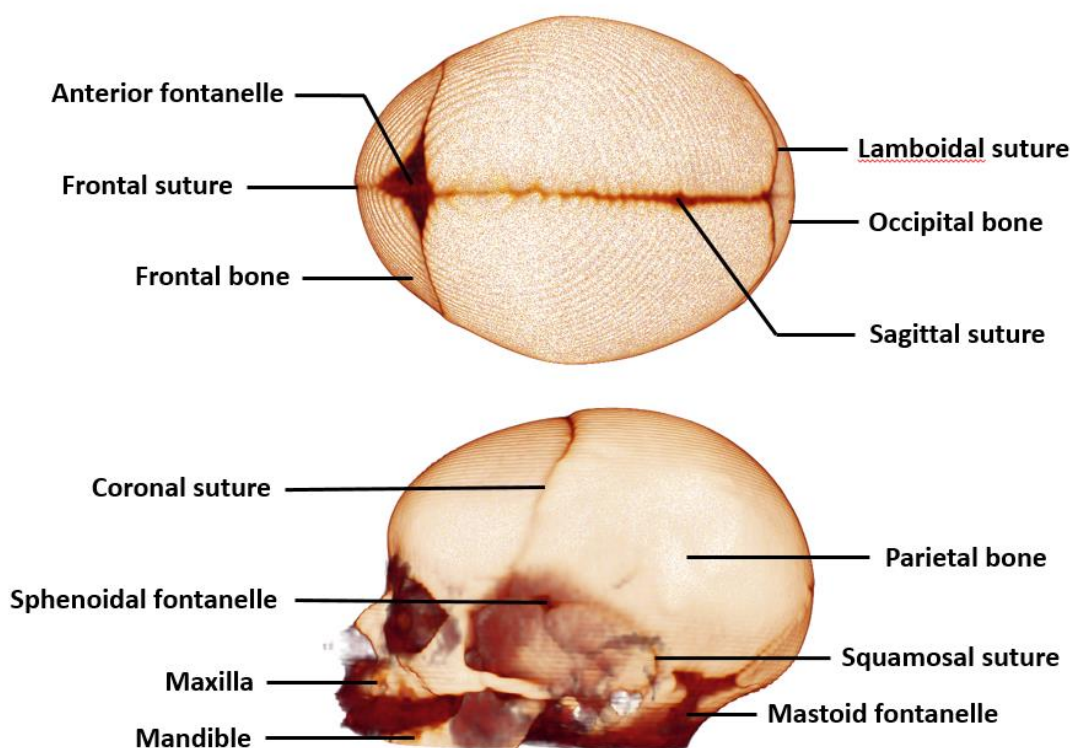


Figure 1.5: Infant suture and fontanelle distributions

Figure 1.5 above depicts all the sutures and fontanelles that develop during infancy. The frontal suture, also known as the metopic suture, is between the left and right frontal bones. This suture starts to close from front to back around the second month pc and normally disappears between nine months and two years. The sagittal suture is the midline of the left and right Parietal bones, while the lambdoid suture is located between

the Parietal bones and the Occipital bone. The left and right coronal sutures are between the left frontal and parietal bones and the right frontal and parietal bones respectively. Unlike the frontal suture, the fusion of these sutures is from back to front or from side to center, occurring at different times for each individual.

The anterior fontanelle (closes later from 1 to 3 years) is a soft spot at the front top of the cranium, converged upon by the frontal, sagittal, and coronal sutures. The Posterior fontanelle is at the back of the cranium and in the middle of sagittal suture, and closes after 2-3 months. The squamosal sutures are between the parietal bones and temporal bones, which, with the coronal sutures, form the sphenoidal fontanelles (closing around 6 months). The mastoid fontanelles (which close between 6 and 18 months) are formed by the squamosal and lambdoidal sutures (Pritchard, Scott, and Girgis 1956).

Sutures play a significant role as skull bone growth sites while remaining patent for brain expansion inside (Dye 2000; Steinbock 2011). In other words, in order to accommodate the expanding brain, sutures produce new bones at the bone fronts, which are attached to sutures, while maintaining the suture itself at approximately the same size and in an unossified state but increase the volume of the bones (Opperman 2000). (Opperman 2000) believed that bone growth sites, unlike the bone growth center, are passive bone remodeling regions without intrinsic growth ability, and need to be triggered by external stimuli. In cranium development, the key external stimulus is believed to be the enlarging brain, which exerts pressure on the internal surface of the calvarium to separate the intramembranous bones and stretch the suture, thereby stimulating the stretched sutures to develop more bones and go back to their original size (Reardon 2000). Therefore, skull development turns out to be an oscillatory separating procedure whereby the sutures try

to maintain their size by adding more bones at the edges of the bone fronts to compensate for the increasing calvarial volume (Sperber, Sperber, and Guttman 2010).

Moreover, these flexible and transitory disconnections (sutures) among these cranial plates are essential to assisting the infant's head as it passes through the birth canal and meanwhile avoiding brain damage (Steinbock 2011). After birth, the flexibility of the sutures and fontanelles can also absorb external forces to shield the brain when the infant's head is slightly knocked (Gilbert and Singer 2006).

1.3 Craniosynostosis: The Abnormality of Skull

Development

1.3.1 Overview

Obviously, the sutures are significant during the early development stage, as otherwise a pathology called craniosynostosis would take place, when one or more sutures close prematurely (Johnson and Wilkie 2011). Because the brain is blocked from developing in the perpendicular direction of the closed sutures, it is forced to over expand in the perpendicular directions of other opening sutures, resulting in a distorted head shape and deformed facial features (Johnson and Wilkie 2011). The discovery of craniosynostosis can be traced to 1851, when (Virchow) first indicated a type of skull abnormality caused by prematurely closed sutures.

The exact cause of this pathology is still unknown, but may be related to both genes and environment. This pathology occurs 300-500 times in every one million live newborns

(Aviv, Rodger, and Hall 2002). It is a relatively highly frequent pathology in newborns such that one subject may be found in every 2500 newborns, and so it has received much attention since some cases of it may contribute to high intracranial pressure and certain developmental delays (Pritchard, Scott, and Girgis 1956).

1.3.2 Types of Craniosynostosis

Craniosynostosis is categorized into four types depending on which suture is fused:

Trigonocephaly (frontal suture closed), Scaphocephaly (sagittal suture closed), Plagiocephaly (either of coronal or lambdoid suture closed), and Brachycephaly (bicoronal suture closed), among which the first two are the most common types. We have indicated the typical shape of these skulls in Figure 1.6.

Among the most common types of pathological cases, scaphocephaly, the sagittal suture is fused, causing a long, boat-shaped head. The frequency of scaphocephaly, according to statistics, is around one in every 5000 children (Pritchard, Scott, and Girgis 1956). The brain's development is hindered in the perpendicular direction of the sagittal suture, and thus expands more in the direction of the sagittal suture to accommodate this blockage. The temporal brain lobes could be pressed in such conditions, leading to disorders of hearing, sound perception or pronunciation.

Trigonocephaly occurs when the metopic suture (separates the frontal bones) is fused before 9 months or even prenatally (normally closed between 9 months to 2 years), leading to a triangular forehead (Pritchard, Scott, and Girgis 1956). As the second most common type, the frequency of occurrence is approximately one in every 15,000 children. It may be accompanied by complications in neuropsychological development,

problems with vision and ocular hypotelorism. In this situation, it is necessary to rebuild the whole forehead to regain a regular shape.

Plagiocephaly is further classified into anterior plagiocephaly and posterior plagiocephaly. Anterior plagiocephaly, whose prevalence is estimated to be 1 in every 10,000 births, is the premature closure of either side of the frontal suture, whereas the fusion of the unilateral lambdoid suture as known as posterior plagiocephaly (Pritchard, Scott, and Girgis 1956). The appearance of anterior plagiocephaly could be evidence of facial deformity in some cases while posterior plagiocephaly creates a flat surface at the unilateral back of the head. Both types of plagiocephaly could lead to visual impairment and higher intracranial pressure.

Brachycephaly is treated as premature closure of the bilateral coronal suture, preventing the brain from growing in the perpendicular direction of the lateral suture so that it develops more in the closed suture direction. The skull is compressed in the sagittal direction and extensively in the transverse direction, leading to eyeball protrusion and a flat head as the most obvious symptoms. In such cases, the intracranial pressure could be extremely high (Pritchard, Scott, and Girgis 1956).

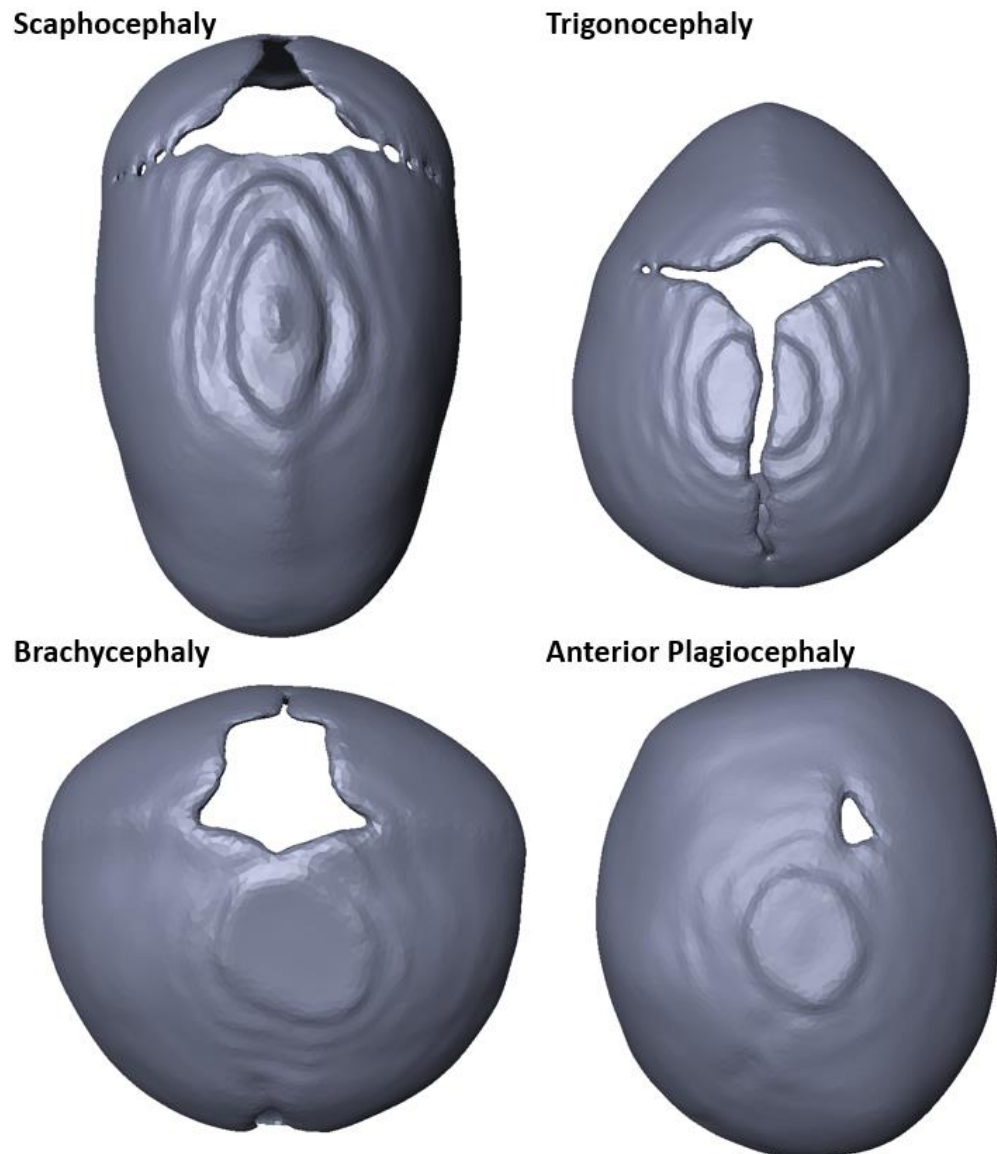


Figure 1.6: Common types of craniosynostosis. The left top skull was scaphocephaly, the right top skull was trigonocephaly, the left bottom skull was brachycephaly, and the right bottom one was anterior plagiocephaly.

1.3.3 Current Treatment Methods

Surgery is considered the routine treatment for craniosynostosis patients in order to correct the skull shape and reduce the excessive intracranial pressure caused by suture fusion. (Lannelongue 1892) performed the first surgery for a craniosynostosis patient. (Jane et al. 1978) shared their experience adjusting the frontal prominence of a scaphocephaly patient with the Pi (π) technique. It is called Pi technique since the shape of the cuts on the cranial roof looks like “ π ”. Again, (Jane et al. 1984) utilized dural plication to correct plagiocephaly. (Albright 1984) described parietal wedge craniectomies for the treatment of scaphocephaly. (Greene and Winston 1986) published their treatment for scaphocephaly, which included sagittal craniectomy and bi-parietal morcellation. (Persing et al. 1989) proposed near-total cranial vault reconstruction for the treatment of brachycephaly. (Cohen et al. 1991) published their treatment for craniosynostosis using fronto-orbital remodeling with the advancement-onlay technique. A sunrise technique was published for surgical treatment of occipital plagiocephaly by (D. F. Jimenez and Barone 1995). This technique focuses on reopening the fused lambdoid suture and reconstructing the flattened occipital bone (D. F. Jimenez and Barone 1995).

(Vicari 1994) first applied the endoscopic technique for craniosynostosis treatment.

Endoscopic technique aims to complete a surgery with small incisions and endoscopic instruments that help view the internal body of a patient (Barone and Jimenez 1999).

(Barone and Jimenez 1999) combined the endoscopic craniectomy with helmet wearing postoperatively. (S. R. Cohen et al. 2002) proposed the concept of immediate cranial

vault reconstruction utilizing biodegradable plates in minimally invasive craniosynostosis repair in 2002.

So far, the surgical treatments for craniosynostosis have developed from simple suture re-opening procedures to cranial vault reconstructions (Thaller, Bradley, and Garri 2007).

Generally, neurosurgeons have believed that the best time for surgical treatment for a craniosynostosis patient is between two to four months, when the skull bone is relatively soft and has potential to grow. We will introduce some popular approaches for common types of craniosynostosis described in (Thaller, Bradley, and Garri 2007).

1.3.3.1 Scaphocephaly

Various approaches are applied for scaphocephaly determined by the severity and the age of the patient. If the deformity has been diagnosed in early stage, neurosurgeons would suggest sagittal synostectomy only. The Pi technique could be applied for patients that only appeared with frontal bossing but no saddling or occipital abnormalities (David F. Jimenez et al. 2002). To infants that has significant deformity, a cranial vault remodeling should be preformed with biodegradable plates and screws.

1.3.3.2 Trigenocephaly

(Noetzel et al. 1985) summarized that no matter the severity of the abnormality, the surgical procedures are quite consistent. The routine approach is osteotomies on bilateral supraorbital rim, in which a temporal tenon or Z-plasty might be considered with the purpose of stabilization. A modified medial orbital osteotomy is an alternative for

extensive interorbital separation for patients with hypotelosrism. Helmets are suggested to wear postoperatively for several months.

1.3.3.3 Unicoronal and Bicoronal Synostosis

Depending on the level of deformity of this pathology, the surgical procedures are variant. Normally, supraorbital rims osteotomies and bifrontal craniotomy are accomplished. For patients with specific facial abnormalities, more osteotomy might be carried out. Fronto-orbital advancement technique and cranial reconstruction are carried out for brachycephaly cases.

1.4 Medical Imaging

1.4.1 Overview

Medical imaging is a technique that allows to visualize interior part of a human body or the functions of some organs, to assist disease diagnosis, monitoring and treatment. It can be sub-classified into various modalities, including radiography, ultrasound, computer tomography (CT), magnetic resonance imaging (MRI), nuclear medicine and so on.

1.4.2 Radiography

Radiographic technique was developed firstly from the discovery of x-rays in 1895 by the physicist Wilhelm Roentgen (Bushberg 2002). The x-rays are emitted from an x-ray tube above one side of human body, and penetrate through the body to reach the x-ray detectors on the other side, from where to produce x-ray images. Different tissues in human body has different capabilities to absorb the energies of x-ray beams that passing

by (also known as x-ray attenuation), resulting to discrepant amount of x-ray energies distributed on the detectors, which show different tissues with different intensities.

1.4.3 Computer Tomography (CT)

Computer tomography (CT) is an imaging technique that produces cross-sectional images using x-ray technique for diagnostic and therapeutic purposes in clinics. While an x-ray image is an 2D representation of a volume of human part, CT can be interpreted in a way that taking several 2D x-ray images of the volume from different angles to reconstruct the anatomy of the whole volume in 3D.

X-ray CT is capable of showing superior contrast between bone and soft tissues, which make CT scans as a standard diagnosis procedure and surgical planning material for craniosynostosis patients.

1.4.4 Digital Imaging and Communication in Medicine (DICOM)

Digital Imaging and Communication in Medicine is defined as a standard protocol of handling, transmitting and storing information in medical imaging. The concept was first introduced by the American college of Radiology (ACR) and National Electrical Manufacturers Association (NEMA) in 1983. DICOM covers disciplines of images compression, visualization, image presentation and so on (Kahn et al. 2007).

Each DICOM file represents a cross-sectional image with a matrix of pixels, each of which contains a grayscale. With appropriate mathematics, we can extract 3D geometry of any tissue or organ that stored in a set of DICOM images. There are a lot of software

existed now to support visualizing and manipulating DICOM images, such as 3D Slicer, Amira and so on.

1.5 Previous Work

1.5.1 Overview

In previous sections, we have explained the pathological situations that might occur during skull development for infants and corresponding treatments. Considering the ethical problem, the studies for infant's skull growth has been developed very slow. Recently, with the rise of virtual reality concept and three-dimensional (3D) medical imaging techniques, some of the research groups start to devote to improving the treatment for craniosynostosis. In this section, we will discuss most related work (2010 - 2016) with respect to virtual reality and medical imaging techniques.

1.5.2 Surgical Evaluation Tool for Craniosynostosis

In their paper (Oliveira et al. 2010) , Oliveira et al. introduced an evaluation system to measure the outcomes of craniosynostosis surgeries, utilizing image registration technique. For their system, three sets of CT scans of a patient are required, which includes scans of preoperative, postoperative, and one-year postoperative. With the preoperative images as a reference, the other two images were transformed to align with the reference. They indicated the local changes (visually and quantitatively) of those two postoperative images from preoperative one with minimum distance map.

In the paper, they stated that the minimum distance map is a useful tool to assist neurosurgeons to evaluate surgery. However, such a tool can only compare the differences of the skull between before and after surgery, but how do we evaluate a change as good or not. In our opinion, a good evaluation tool should be able to investigate the ability of a postoperative skull to grow back to normal shape because of the surgery.

1.5.3 Finite Element Analysis of Craniosynostosis Adjustment

(Wolański et al. 2013) described an approach to simulate postoperative skull correction for surgical evaluation, utilizing finite element modeling and analysis. Since the malformation of each case is variant, it is necessary to design patient specific skull incisions for each patient (Roth, Raul, and Willinger 2008; Larysz et al. 2011). The purpose of their work is to choose the best surgical option within various possibilities on the basis of the quantitative simulation results.

For each patient, (Wolański et al.) used their preoperative computational tomography (CT) scans to build 3D representation of the deformed skull using finite elements. The severity of the deformation was quantified in the beginning in order to compare with the result. For scaphocephaly, the cranial index was measured whereas for trigonocephaly, the angle of the forehead was measured. With guidance of neurosurgeons, several surgical options were designed for each patient. In the paper, each case has two possible solutions. The postoperative skull was then inputted into their simulation software to examine the ability of the skull to be tilted (bent over). They concluded that the more a postoperative skull can be tilted, the better a surgical option is.

We believed this algorithm has the following limitations. First of all, the simulation of their surgical correction was based on a condition that all the skull pieces should be connected as a whole, which is not true for most of real cases. For an infant, we have discussed in the first chapter, the skull is separated into several plates by sutures since the brain volume develops faster. Second, the simulation was performed without the consideration of skull extension itself. During the first year of human life, the skull development is fast but is varied individually. Therefore, in the middle of skull correction, the gaps caused by incisions might be closed. Finally, the extent of a skull can be tilted is not the only factor to assess the surgery for craniosynostosis. For example, for a scaphocephaly skull that is much longer and narrower than the normal ones, the aim of the surgery should make the head shorter and wider. However, the tilt capability of a skull cannot make the skull shorter.

1.5.4 Automated Diagnosis of the Types of Craniosynostosis

(Mendoza et al. 2014) developed an algorithm to quantitatively classify a craniosynostosis skull and measure the severity of malformation from normal in order to assist surgical planning for craniosynostosis. Their first step is to generate each patient's skull model with normalized orientation and spatial location. With a technique called graph-cut (Liu et al. 2008), they were able to detect all the open sutures on a skull model, and to determine if there is a fused suture by comparing to the template (sutures of normal skull). So far, they can roughly diagnose a skull to be either normal or a type of craniosynostosis. To further characterize a pathological case from the normal ones, a statistical model was built with 90 normal skull cases, in order to develop an averaged

normal-skull as a reference. Subsequently, for each skull, local deformation (by Euclidean distance) and curvature value were calculated to indicate the difference between this skull and the normal reference.

The authors showed a high-accuracy (95.7%) to auto-diagnose a new skull shape.

However, the abnormality of a skull can be easily deduced by looking at it. In addition, the shape of each type of craniosynostosis is typical, for example, scaphocephaly patients' skulls normally have long-boat shape. Cases that cannot be diagnosed by looking at it can be treated as not severe cases. In addition, taking CT scans is a standard procedure to diagnose Craniosynostosis, which makes it much easier to indicate which suture/sutures are closed. As a result, it cost too much to build a such complex system for diagnosis.

1.5.5 Statistical Model to Predict Craniosynostosis by the Snake Algorithm

In (Walker et al. 2016)'s work, they measured the asymmetries of intracranial volume and the patency of each cranial suture to predict the types of craniosynostosis. They used CT scans of 77 craniosynostosis patients and 40 normal infants to train their predictive system.

After the skull segmentation on each 2D slide from CT scans of each patient, they used the snake algorithm to identify the gap (suture) between each two plates, and to refine the border of the inner surface of the skull so as to measure the intracranial volume (Hermann et al. 2012). They discovered that the total intracranial volumes of patients remain the same as normal infants'. Consequently, they attempted to measure the

asymmetry of the volume to evaluate the skull shape. Each skull model was divided into four parts manually with respect to the midlines in horizontal and vertical directions. Further, they utilized the identified skull bone gaps from CT slides to examine the closure of sutures. With these two results, they claimed the accuracy of their predictive system was 91.9%.

As I mentioned in the previous section, the Craniosynostosis can be easily recognized with CT scans so that a predictive system is not necessary for diagnosis. Moreover, this system is not completely automatic compared to previous work.

1.6 Thesis Rationale

1.6.1 Motivation

In previous section, we have discussed some common procedures in craniosynostosis that were **introduced in** (Thaller, Bradley, and Garri 2007). They also admitted that although the technique for treatments has been developed, the quantification of surgical evaluation remained unsolved. Some researchers attempted to use the rate of reoperation to assess the surgeries (Williams et al. 1997; McCarthy et al. 1995). Alternatively, some neurosurgeons compared preoperative and postoperative cranial indices (the relation between maximum skull width and maximum skull length) to measure the surgical outcomes. However, these two methods failed to describe the changes of local shape.

In addition, without an appropriate assessment method for surgical outcome, neurosurgeons were not able to validate the efficacy of their surgical techniques. As we know, for different degrees and types of deformity, the surgical approach should be

varied. The problem for neurosurgeons then is how to select the most efficient way among various options. Even for a selected surgical plan, the problem is how far an osteotomy should be carried out in order to bring the best result. Currently, neurosurgeons only use their experience to design surgical plans.

In the section of previous work, we have discussed some engineering supports for craniosynostosis. (Oliveira et al. 2010) developed a tool to measure the difference between the postoperative skull and preoperative skull, but failed to evaluate the level of normality for the postoperative skull. (Wolański et al. 2013) described their surgical simulation system considering only the tilt ability of the skull. (Walker et al. 2016; Mendoza et al. 2014) used different methods to build an automatic diagnosis system for craniosynostosis. All of these work did not focus on assisting neurosurgeons in deciding on how to choose the most appropriate surgical plan for a specific patient and evaluating how well a surgery has been performed to a patient.

1.6.2 Hypothesis and Objectives

The aim of our research is to develop a predicable model for neurosurgeons to design the best plan from various options. This model is expected to allow neurosurgeons to carry out extensive surgical plans on the patient's head model, and to see corresponding postoperative skull developments overtime (surgical result).

Computer simulation techniques (van Wijk van Brievingh and Möller 1993), which have been extensively used in biomedical area currently, allow us to develop such a predictable tool, without considering ethical issues to perform experiments on infants. With mechanical features embedded, the technique promises to mimic an infant's head

model, including skull, brain and suture. Further, with an appropriate physical modeling, we can simulate dynamic head development of an infant.

Our hypothesis is that with the ability to simulate a head development, we can accurately predict surgical result for neurosurgeons by simulating the postoperative skull-brain growth over time. To address this hypothesis, we have the following objectives:

- 1) To generate infant's head models with CT scans and mechanical features, and to develop mathematical model for dynamic simulation.
- 2) To simulate both normal and abnormal head development, from which to explore the mechanism of head development and to validate our simulation algorithm.
- 3) To perform surgery on patient's skull model, and simulate postoperative head development to foresee the surgical result.

In addition, for each skull shape, a NRK is measured, which is capable of describing the degree of abnormality of a skull with respect to the normal shape. With this tool, neurosurgeons are able to measure the efficacy of a surgery with the trend of three values, which includes the shape indices of preoperative and postoperative skull shapes and the skull shape one-year after the surgery.

Curvature, which describes the local shape of a geometry (Carmo 1976), is able to characterize different shapes of skulls, in our case, including normal skull and common types of craniosynostosis. The features will be summarized as a NRK, showing different values with respect to different shapes. A high value of NRK indicates a high level of deformity of a skull shape. In addition, we will associate this index with cranial index

(skull width over skull length), which is an evaluation method for head shape in clinics, to plot skull shapes onto a 2D Figure for intuitively visualization.

Our hypothesis then is the NRK for a skull can correctly predict a specific type of skull shapes, and is able to show the severity of the abnormality of this shape. With this hypothesis, we have such objectives:

- 1) To investigate a simple algorithm to estimate curvature values of a skull model, and to develop a statistical model to calculate NRK.
- 2) To evaluate a surgery by calculating the shape indices of three skull shapes from one patient, including skulls of preoperative, postoperative and one-year after surgery.

1.6.3 Outline

Chapter two contains our initial algorithm (a pressure based model) to simulate infants' head development during the first year of human life. We used this algorithm to simulate normal head development, and three common types of craniosynostosis.

Chapter three focuses on introducing our simulation system with a force based model. We also simulated normal head development and three common types of craniosynostosis, in order to compare with our previous model.

Chapter four introduces the procedures of developing a statistical model to characterize different types of skull shapes, so as to provide a numerical assessment of the level of

deformity of a skull. With this tool, we are able to evaluate the simulation result of any type of head development, moreover, to evaluate real surgeries.

Chapter five is a conclusion section to summarize all of my work.

Chapter 2

2 Head Development Simulation with Pressure Based Hybrid Model

2.1 Overview

Computer simulation is a technique that uses abstract models to simulate a specific system on one or more computers (Kheir 1995). It has recently been applied extensively in biomedical research. This technique can be used to develop surgical simulators, which help novices to develop their various surgical skills (O'Toole et al. 1999; Duffy et al. 2004; Seixas-Mikelus et al. 2010), to mimic parts of human body (Perktold and Rappitsch 1995; Stergiopoulos, Young, and Rogge 1992; Ghazanfari et al. 2014), and to test the mechanical properties of specific tissues (Miller et al. 2000). In this chapter, we attempt to use a computer simulation technique to imitate head development with a pressure based hybrid model.

2.2 Framework of Our Simulation System

Computer simulation is a technique to simulate the dynamic behaviors of a system on the basis of a three-dimensional (3D) static model, which in our project is an infant's head. Our approach to 3D modeling is mesh generation, also known as grid generation, which is a technique to describe geometric structures with polygonal or volumetric meshes (Edelsbrunner 2001). Polygonal meshes delineate the surface of 3D objects with a set of vertices, edges, and (triangular, quadrilateral or other simple polygonal) faces.

Volumetric meshes represent the whole volume of 3D objects with finite elements, including pyramids, tetrahedral, and hexahedral (the shapes are shown in Figure 2.1). The volumetric mesh is often used to characterize deformable models for finite element analysis (FEA), which analyze the response to stress by taking account a number of factors, including mass, volume, temperature, force, and displacement (Krishnamoorthy 1995; Desai 2011).

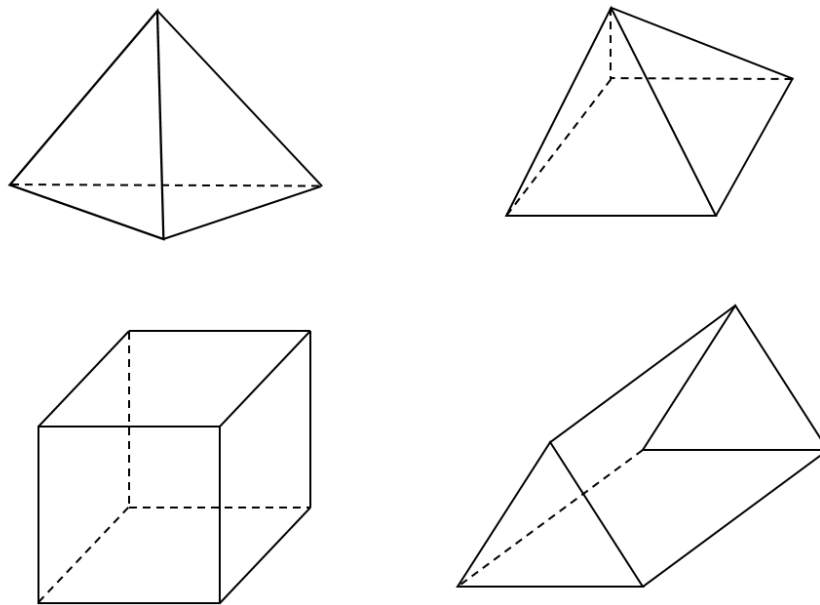


Figure 2.1: Unit shapes that are alternative to form volumetric mesh

Although the final goal of this project is to simulate postoperative head development, we hope to first simulate both normal and abnormal head developments, from which it is easy to validate our algorithm, and to explore how skull shape progresses under different circumstances. Therefore, we carefully designed a scheme for our initial simulation, which was based on a normal head model, including skull plates, sutures and the brain.

Figure 2.2 below demonstrates our work flow. First, clinical data for an infant head is acquired in order to label out the structure of the skull. Mesh generation was applied separately on these segmented structures to develop our 3D head model, which is essential for our simulation. These assets were then imported into a simulation platform Artisynt (Fels et al. 2006) and assigned by material properties, such as Young's modulus, Poisson's ratio, and the density of each object. Mathematical models were also built for each structure, to manipulate autonomous behavior or adapt response to extra stress. Six markers were set on the skull to monitor the maximum length, breadth, and height of the skull during the simulation.

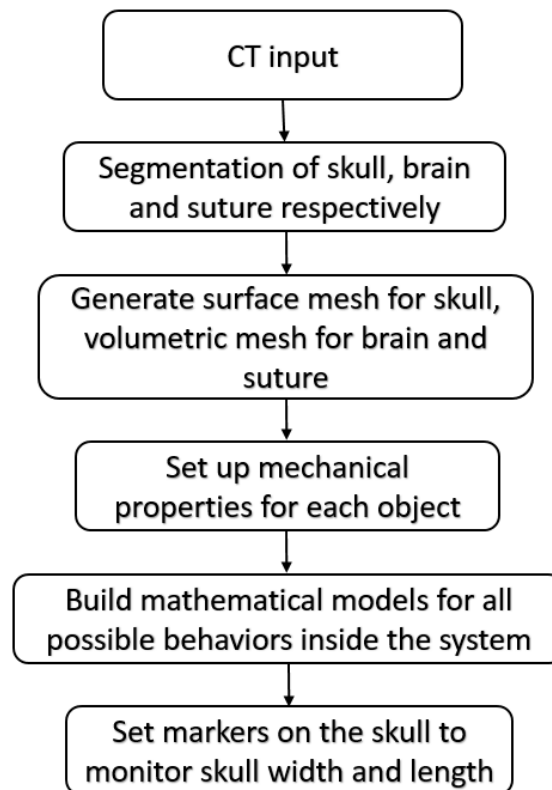


Figure 2.2: The flow chart of the procedure of our head development simulation

2.3 Simulation Software: Artisynt

Artisynt, which is a powerful and extensible platform for three-dimensional (3D) object modeling and simulations, was flexible enough to allow us to implement our hybrid model (Lloyd, Stavness, and Fels 2012). Artisynt supports numerous types of items, such as rigid bodies, finite element components, and particles, enabling us to build our hybrid model. In addition, it is capable of dealing with interactions between any two components, showing the pressures and forces involved (Vogt et al. 2005), so that we can interact, display, and ultimately animate a playback of the interactions between a growing brain and skull. The view point can be changed to let users focus on any part of the model. Any locations on the model can be marked and traced during the simulation so that we can produce reports of the evolution of our model across various metrics.

In Figure 2.3, we show a screenshot of the graphical user interface (GUI) of the Artisynt. In the main window, we can see the model we have imported, which in this case is a model of a jaw. On the left side of this main window, is a hierarchy of all the components involved in the current simulation system. The “Jaw” at the top is the name of this simulation and the “models” is the document which stores all the objects associated with this jaw model, including muscle and jaw bone files. Underneath the main window there is a timeline window, which allows users to track the status of this model at each time step run in the simulation. After one simulation is done, we can drag the time back to any frame so that the main window will display the according status of the model at that particular time. There is a bar of buttons on the left of the documents, which are tools to select or transform the objects of the model. On the top right of the

main window, a play button is provided to trigger the calculations for a simulation after everything has been prepared.

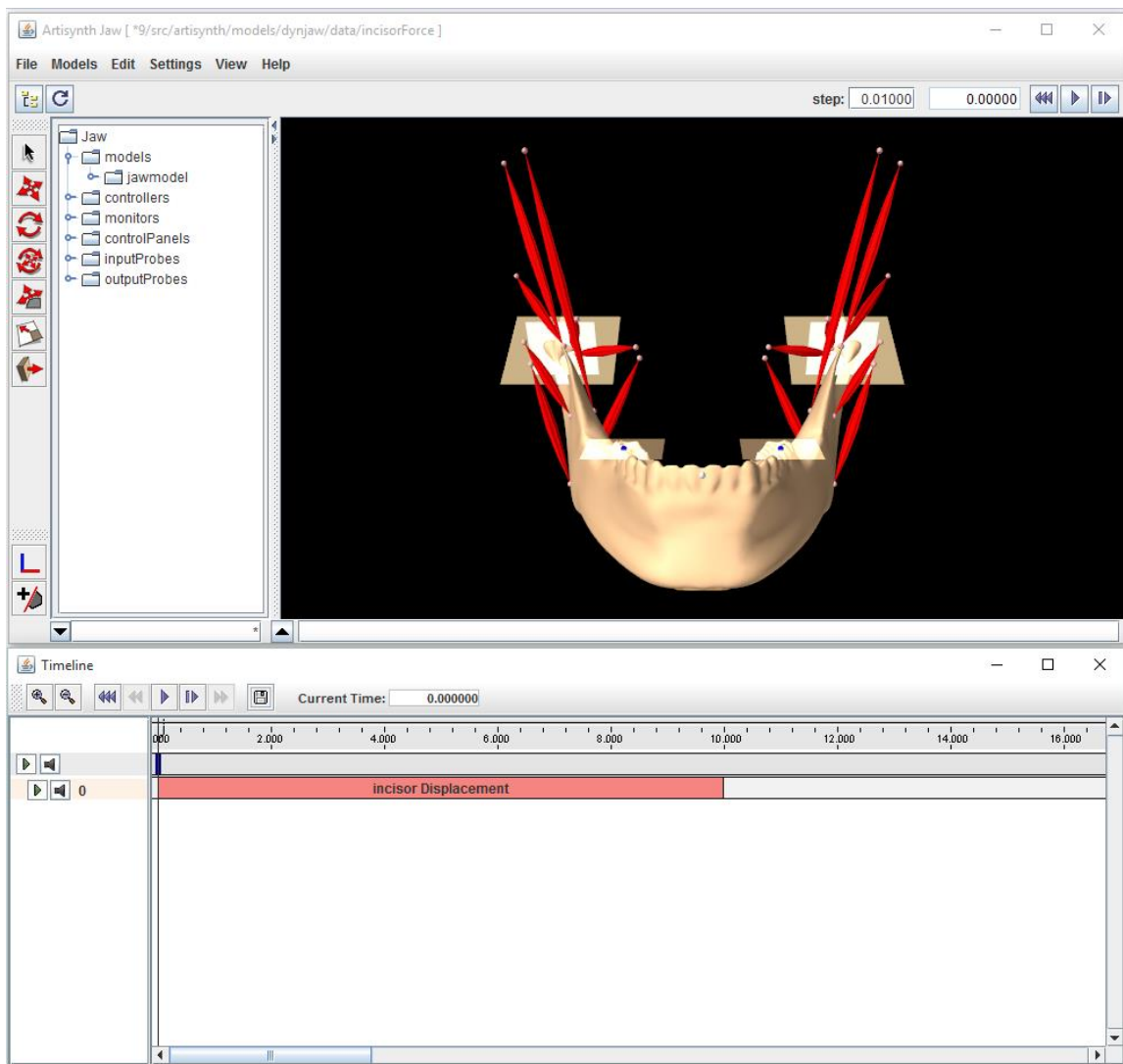


Figure 2.3: A screenshot of the GUI of Artisynt

2.4 The Generation of a Head Model

We have reviewed a set of CT scans from a normal three-week-old baby for our head model generalization. We auto-segmented this baby's skull with the threshold algorithm

provided by the Amira software, which is a platform for 2D or 3D image data visualization and manipulation. The threshold is selected as 100 Hounsfield Unit (HU), which means the pixels in the CT slices that have an intensity higher or equal to 100 HU will be labeled skull tissue. In Figure 2.4, we show one of the slices from the CT images of this normal baby, where the skull bone has higher intensities than other tissues in the head and is labeled by light blue contours.

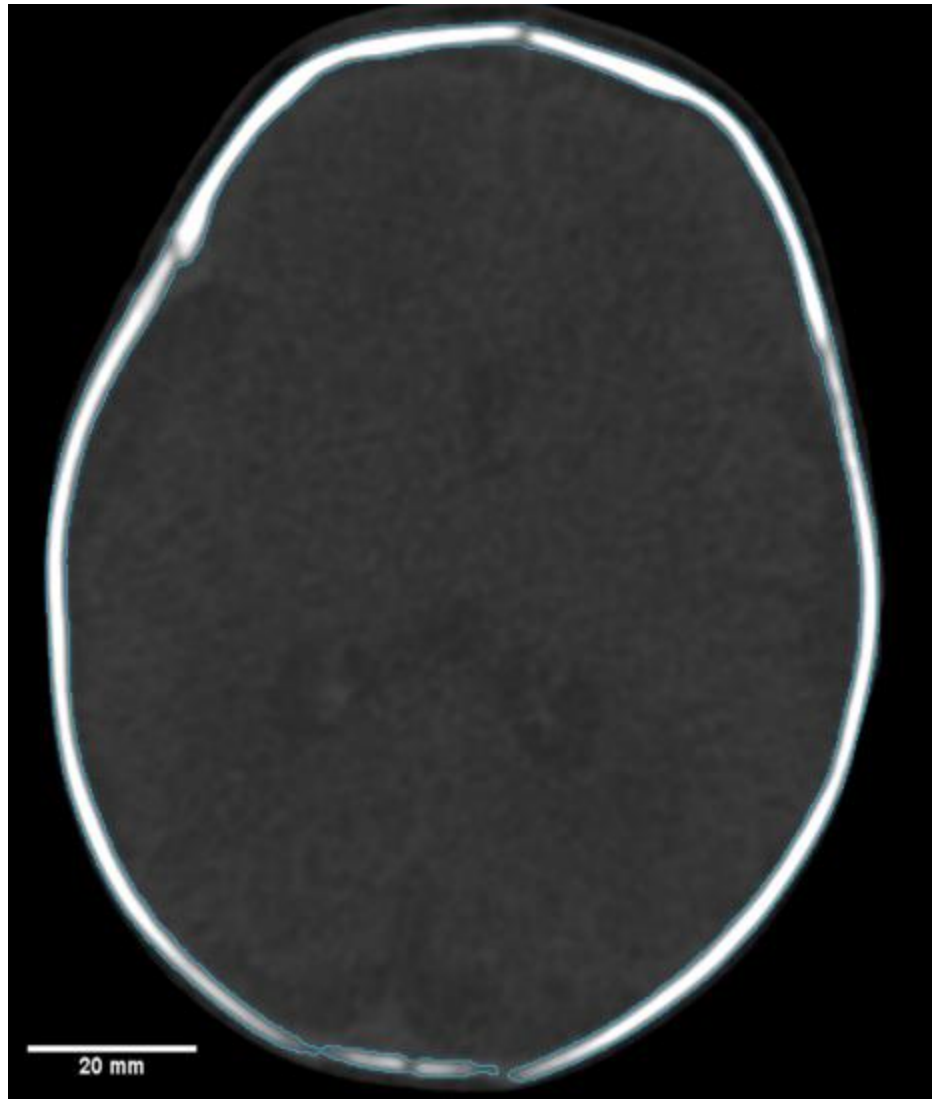


Figure 2.4: A slice of CT scans for the normal baby, using automatic segmentation method in Amira to label out the skull bone with light blue color.

The automatic segmentation results are not as we expected. Amira was able to distinguish the skull from the head very well, but was not able to differentiate between the plates and the sutures because of the noises produced while taking the CT images and the narrowness of the sutures. From the Figure 2.4, we can see that there is a disconnection in the middle of the frontal bones, but the blue contour failed to capture the gap. We

therefore had to further separate the skull manually into 9 plates. In the Figure 2.5, we used the same slice as Figure 9, but labeled the different skull plates with different colors. The red and yellow contours on the top of the image denote the left and right frontal bones respectively, whereas the blue and green contours indicate the left and right parietal bones respectively. The pink line at the bottom represents the occipital plate.

With these skull labels, it is easy to generate triangular meshes for these skull plates separately, which is supported by the Amira software. Figure 2.6 shows the surface mesh of all the skull plates with different colors: the sphenoid bone is in grey, the frontal left is in bright yellow, the frontal right is in red, the parietal left is in green, the parietal right is in blue, the temporal right is in sky blue, the temporal left is in earth yellow, the occipital bone is in purple, and the bone at the bottom is in grey with the purpose of filling the spinal cord hole. The jaw, however, will be excluded in our head development simulation since it is not our concern. We decided to treat our skull plates as rigid bodies, since the bone tissues are much more difficult to deform compared to the brain and sutures. Hence, we only used surface mesh to represent our skull plates. The brain and sutures are soft and deformable tissues, which is why we selected a finite element modeling technique to generate the models.

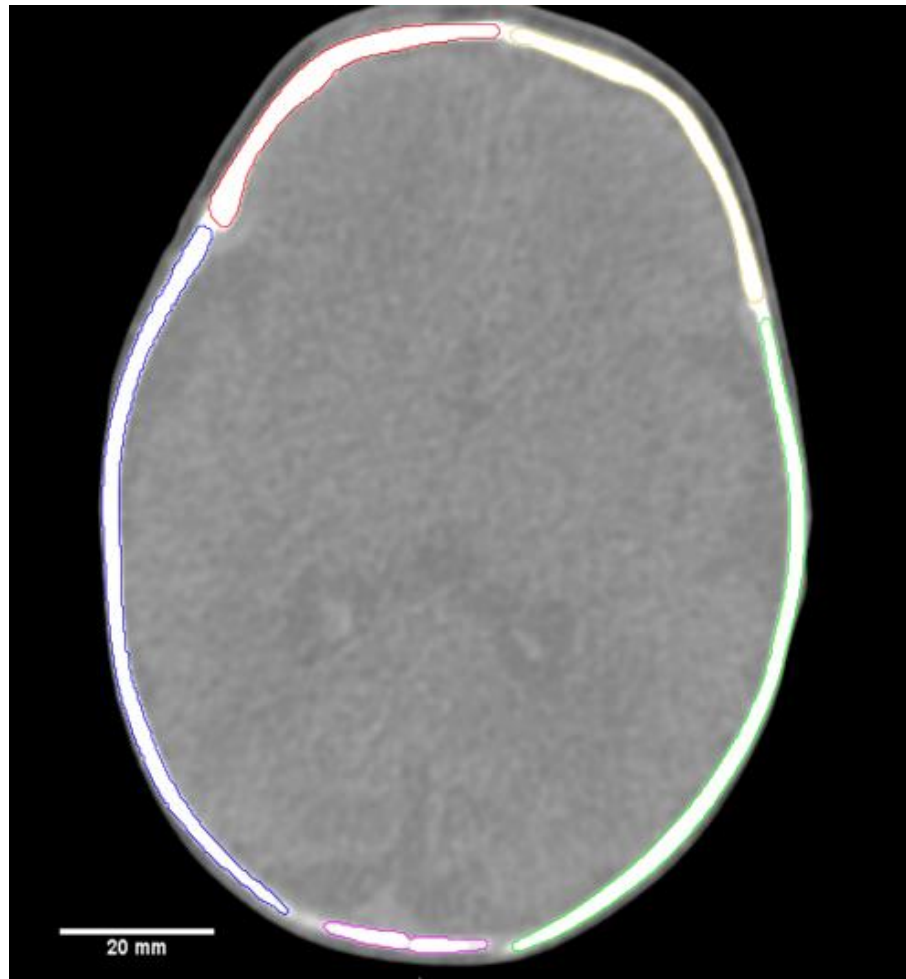


Figure 2.5: A slide of the CT scans from the normal baby. We use 100 as the threshold value to label out the skull structure out of the head, using different color to indicate different skull plate.

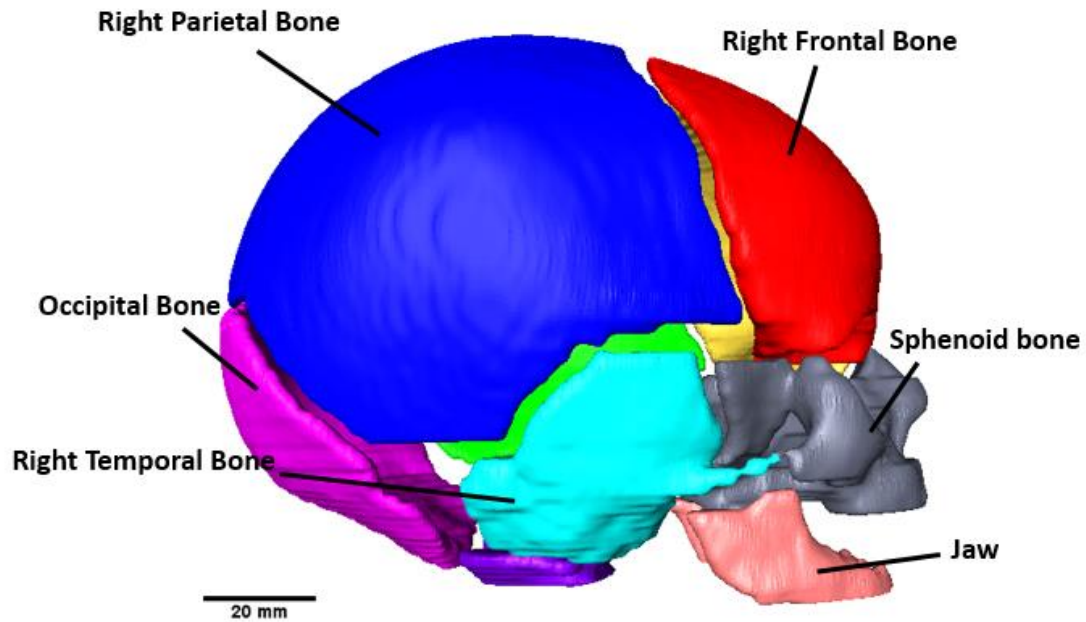


Figure 2.6: Surface model of a normal head, generated according to segmentation labels. Different color indicates different skull plates.

Since CT is good at recognizing bone structure but not soft tissues, there was insufficient brain information in the CT images for automatic segmentation. Fortunately, the only function we need from the brain model is to gradually scale its volume so as to interact with the skull, and therefore an approximate outline of the brain is acceptable. As a result, we manually segmented the brain contour from CT scans within the skull volume to be used as the initial volumetric shape, which could be increased and simulate pressures on the skull plates and sutures. A tetrahedral mesh of the brain model was developed after the simplification and smoothness of its surface mesh, the purpose of which is to optimize the calculation time during the simulation. In Figure 2.7, we show our volumetric brain model after mesh simplification and surface smoothness.

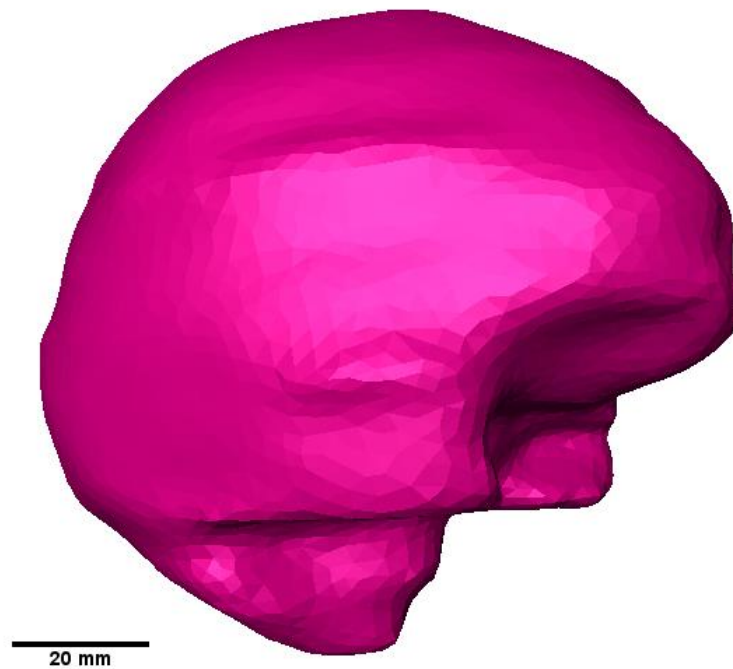


Figure 2.7: The volumetric mesh of a simplified and smoothed brain

Since the sutures play a critical role in our modeling, as the only zones where there is skull growth to accommodate the rapidly increasing brain volume, these should be setup with volumetric meshes between each two rigid skull plates. Of course, there is no suture information in the CT slices either, so at first, we attempted to use the same strategy as developing the brain model. The suture model with tetrahedral meshes was too complicated even after mesh simplification, and its edges, where the skull plates are supposed to connect to, were not smooth as expected.

Consequently, we decided to manually generate hexahedral meshes directly in Artisynt after importing into the 9 separated skull plates as simulation assets (Figure 2.8), and adjusted the position of the suture model to fit into the gaps between the plates until all the spaces were filled. Hexahedral mesh perfectly fits the natural shape of suture, largely

reduce the number of elements, and moreover, the edge of it is well adapted to the edge of skull plates. The sutures connecting the skull plates are shown in blue in Figure 2.9.

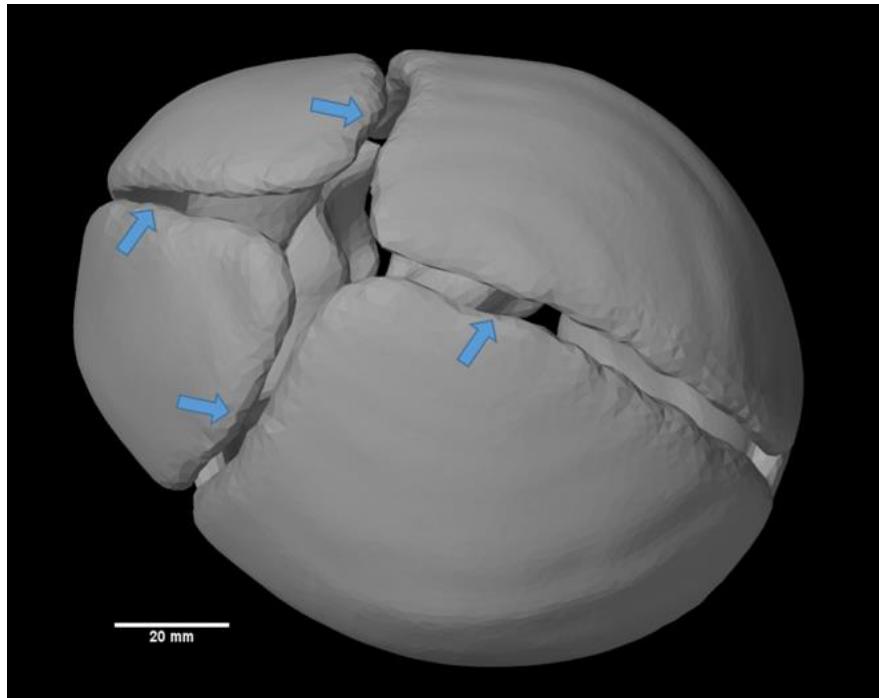


Figure 2.8: Skull plates were imported in the Artisynt, with gaps between each two plates.

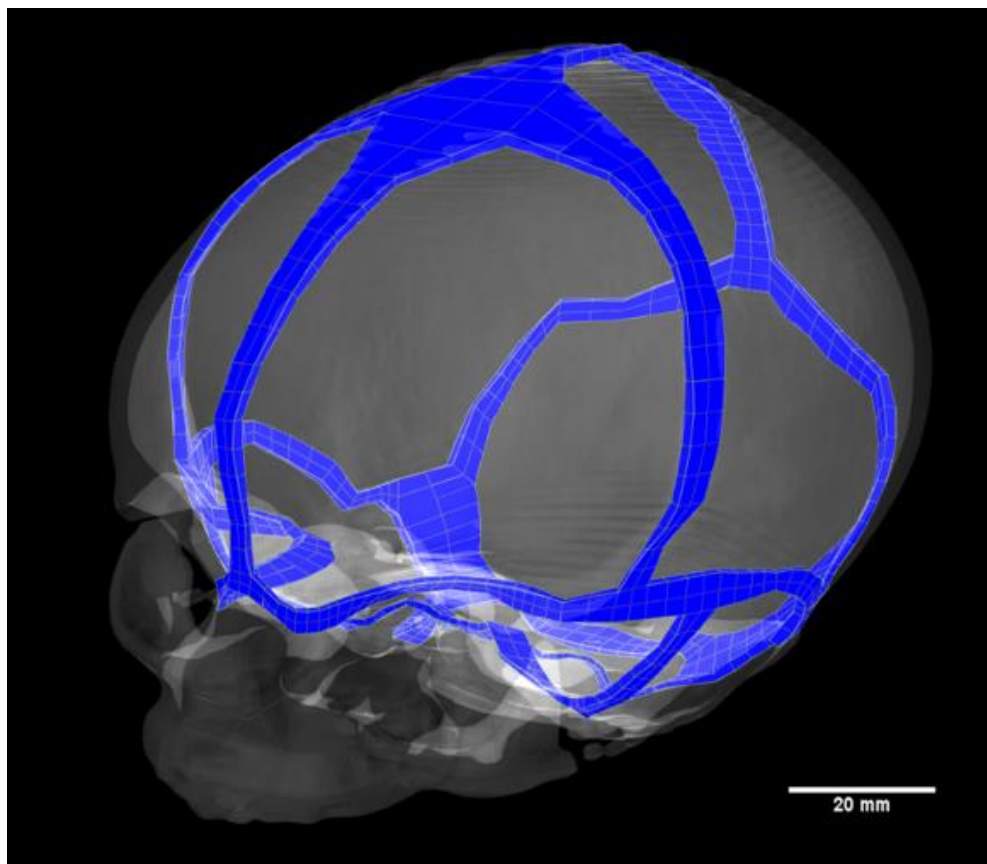


Figure 2.9: The suture model was indicated with blue color, manually generated with hexahedral meshes.

In order to get more correct results, we decided to further proceed our head model to be more real and complex. As mentioned in the introduction chapter, the cranial base gives rise from cartilage and ossified from several cartilage centers. As a result, the sutures located at the cranial base connect with cartilaginous bone plates, which grew slower than membranous plates. In addition, the bone on the face region also develops slower than the growth of membranous skull plates. We indicate these sutures in Figure 2.10, pointed by black arrows. We further segmented these areas

into individual models and re-attach to skull gaps again. We set higher Young's modulus value to these areas so that they are harder to be stretched out.

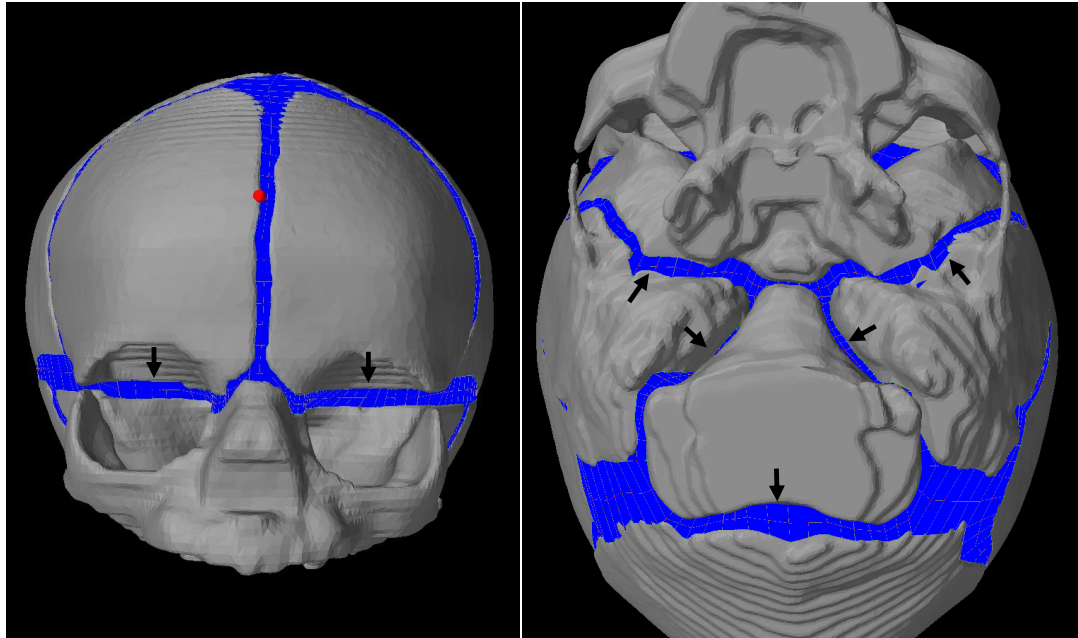


Figure 2.10: An indication of sutures that secrete cartilaginous bone cells. These types of suture have higher values of Young's modulus.

2.5 Mechanical Properties Setup

In order to appropriately simulate a system, it is necessary to know the mechanical properties of all the materials involved in the system. Therefore, before we delve deeper, we should characterize the skull, brain and suture with material features. Normally, these material parameters include density, Young's modulus and Poisson's ratio depending on the type of model. Density is defined as the mass per unit volume. The Young's modulus describes how a material deform (the proportion of the change to original volume) along the direction of stress that exerts on this object. From another perspective, Young's

modulus can be interpreted as a measure of the stiffness of a material. The higher the Young's modulus of a material, more rigid the material is. Poisson's ratio measures such effect that if a force is exerted on a direction of a material, the deformation of this material tends to occur along the other two directions. The values of most stable, isotropic, and linear elastic materials should be ranged between 0.0 and 0.5. The value of 0.5 means a material is incompressible, the volume of which is maintained while being deformed, like water.

In this paper, the mechanical properties of all materials were found from other researchers' work. Some researchers delved into studying the mechanical properties of the skull and sutures in infants (Baumer et al. 2009; Gzik et al. 2009; Couper and Albermani 2005; Coats and Margulies 2006; Claessens, Sauren, and Wismans 2016). Although they might use different techniques to estimate these properties, all of them agreed that the stiffness of skull bones becomes harder while the increase of the age, and the elasticity of the sutures are significantly higher than bones. Since the skull plates in our simulation are assumed as rigid bodies, which cannot be deformed by any stress. Therefore, there is no need to concern about the Young's modulus and Poisson's ratio for our skull model.

There are many previous studies on various mechanical properties of brain, mainly to concern the safety of the brain during the surgery (Miller et al. 2000; Miller and Chinzei 2002; Soza et al. 2005; van Dommelen et al. 2010; Rashid, Destrade, and Gilchrist 2012). Although the variety of methods for estimating the stiffness of the brain are controversial, there is no doubt of the incompressible feature, the ideal Poisson's ratio of which should be 0.5. Since the brain model in our simulation only needs to gradually grow in order to

increase the intracranial volume, the “safety” issue of the brain is not our concern. As a result, from a relative wide range (0.6 kPa – 180 MPa) of the Young’s modulus values, we randomly picked a middle value. In addition, current simulation platforms were not able to characterize the incompressible feature of a material, we will approximate the Poisson’s ratio very close to 0.5.

The following table lists all the related material parameters that we selected for each of the object in our head model. The information of infant sutures was found from (Margulies 2000).

Table 2.1: The approximation of mechanical properties for each object in our head model.

	Density (kg/m³)	Young’s Modulus (MPa)	Poisson’s ratio
Skull plates: (Claessens, Sauren, and Wismans 2016)	2070	--	--
Brain: (Soza et al. 2005)	1040	100	0.49
Membranous Sutures: (Margulies 2000)	1130	200	0.28

2.6 Dynamic Simulation for Each Object

2.6.1 Brain Expansion

According to the chart (“Head Circumference for Boys, Birth to 36 Months” 2016) collected by the Disease Control National Center for Health Statistics (shown in Figure 2.11), the circumference of head from a male infant approximately increased 27%, which basically increased from 36 to 46 centimeters (cm) between new born to twelfth month. Since the brain tissue is incompressible, the scaling rate of the skull should maintain the same as long as the brain is filling the intracranial space completely.

In our simulation, we will only simulate the head development of the first year for two reasons. First, the growth ratio of the head circumference for the first year is the fastest, and then drop quickly subsequently. It indicates that the brain expansion generally occurs during the first year, in which the brain affects the skull development most. Second, the error of our simulation increases while the volume of the head model grows more. For the simplicity of our simulation system, we assumed the speed of brain growth is constant during the first year of human life, since the growth ratio does not affect the development of the skull shape. In addition, the speed of the brain expansion in reality would consume too much to simulate in order to achieve the same magnitude. Therefore, we expected to enlarge the growth ratio of the brain growth so that we could shrink the simulation time of the first year development to approximately 10 to 20 seconds.

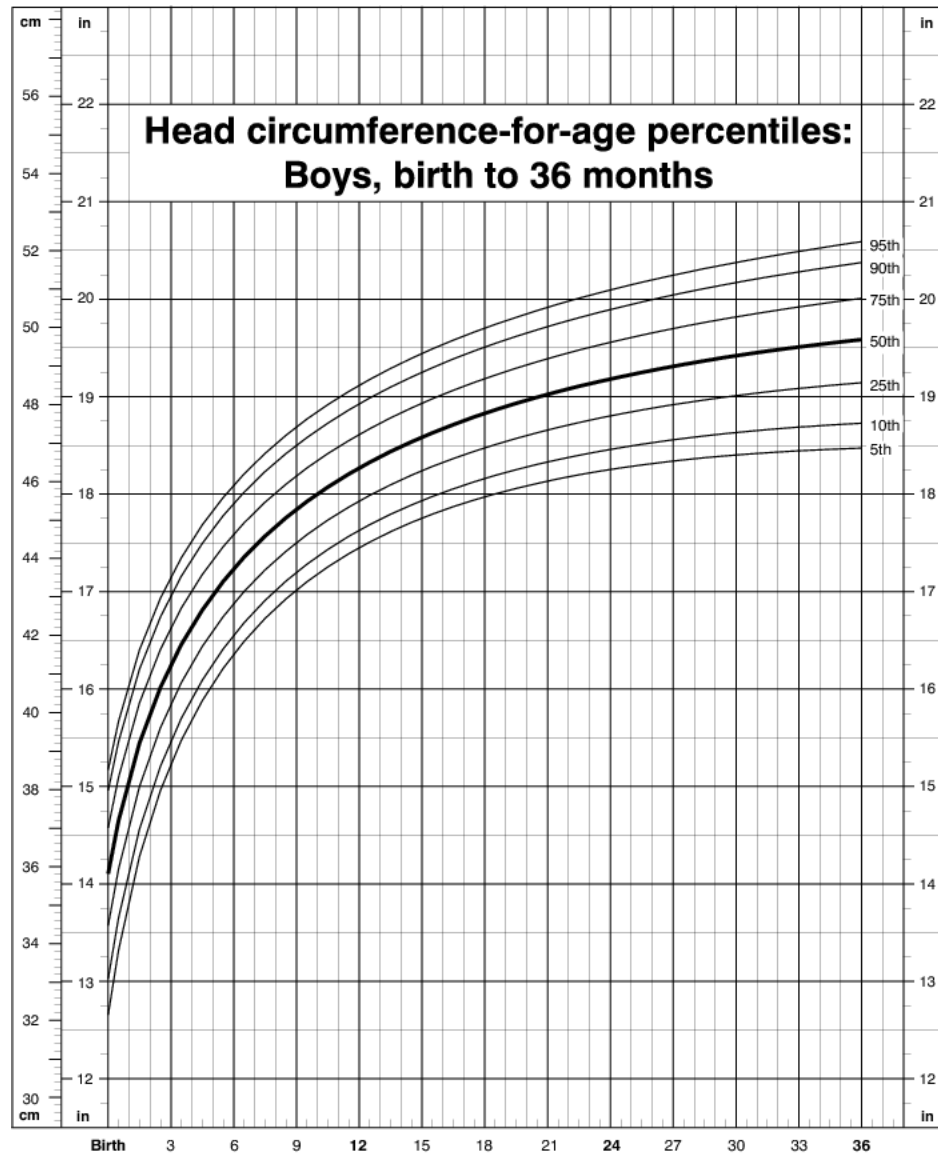


Figure 2.11: The development of circumferences of babies aged within 36 months, where the horizontal-axis represent the age with respect to months, and the vertical-axis indicates the values of circumferences with unit of centimeter (cm).

[<http://www.cdc.gov/growthcharts/data/set1/chart09.pdf>]

Our next question is how to make the brain model grow during the simulation. We assumed that the growth of the brain is isotropic, in other word, the growth ratio will be

the same along any direction from the centroid of the volume. Consequently, in order to scale the volume of the brain, we proportionally increased the distance between each vertex and the centroid of the brain at each time step. The center of the brain was calculated as follow:

$$c_{brain} = \frac{1}{n} \sum_{i=0}^{n-1} v_i \quad \text{Equation 2.1}$$

Where n denotes the number of vertices that formed the brain model, and v_i is the position of the i^{th} vertex ($i=0,1 \dots (n-1)$). The brain growth will be simulated by updating the positions of all the vertices from brain model:

$$v_i(t) = (v_i(0) - c_{brain}) \times (1 + ratio \times t) + c_{brain} \quad \text{Equation 2.2}$$

Where $v_i(t)$ represents the position of the i^{th} vertex at time t , $v_i(0)$ is the original position of this vertex, and $ratio$ is the growth speed, which is 0.005/s.

2.6.2 Suture Stretch

As we mentioned before, the suture is such a soft tissue that unites the skull plates together, and being stretched as a result of the growing brain pushing the skull plates outward. Therefore, we need to attach both sides of the suture to the edge of each two skull plates, since so far, they are just overlapped with each other without any connection. What we did is to get the distance between each suture node and the nearest skull face from this node. If this distance is small enough (less than 0.001mm) to be considered as

the edge of the suture, then it should be attached to the skull plate and recorded into a list for later skull growth (shown in Figure 2.12).

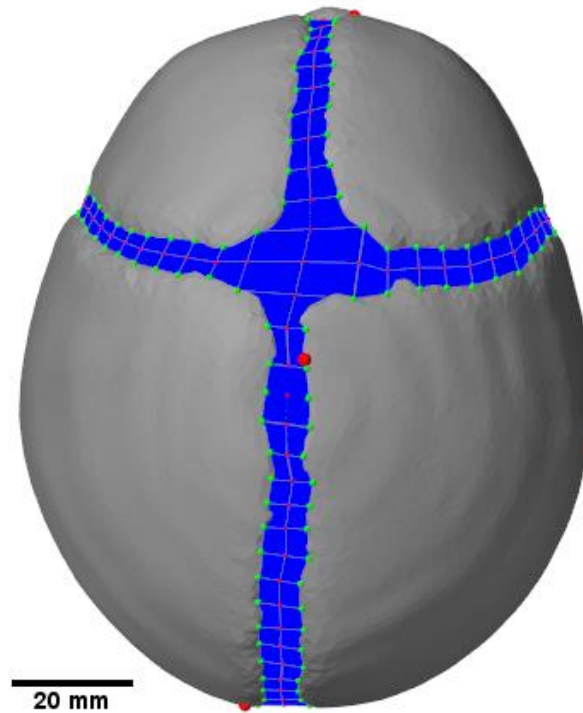


Figure 2.12: Green spheres in this Figure were nodes that were attached onto the closest skull surface whereas red spheres were not attached to any surface.

Accordingly, in our simulation, we hope the behavior of the suture to be passive: being stretched while the brain is increasing to push the skull plates separating from each other (indicated in Figure 2.13), and being shrunk while the skull plates are extending. It is not necessary to develop any additional mathematical model for the behavior of the sutures, deformation due to existing stresses is a built-in function for finite element model in our simulation software Artisynt.

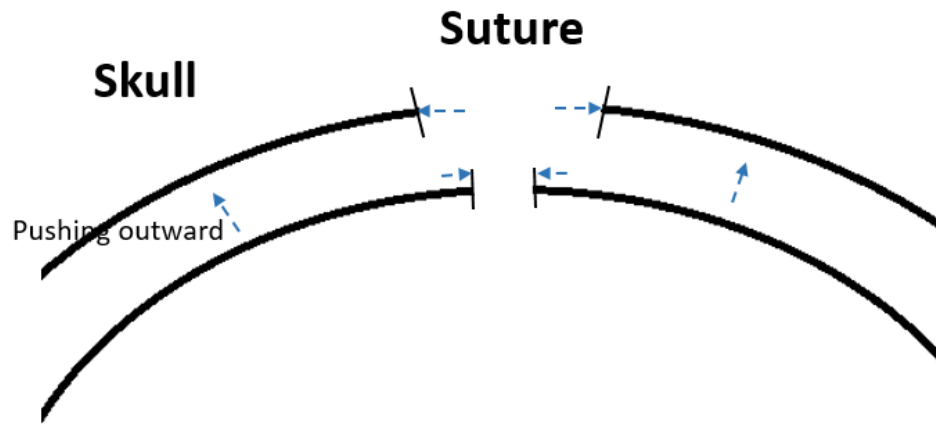


Figure 2.13: This Figure indicates that while the brain volume is expanding, the skull plates at the suture side are leaving from each, leading to the stretchiness of the suture.

2.6.3 Skull Extension

As illustrated above in the Figure 2.13, the increment of the brain volume results in the separation of the surrounded skull plates from each other, making the deformation of the sutures. We believed that the tension caused from this stretchiness signals the suture that the skull plates need extension. With this tension, the suture will then secrete more bone cells to the skull fronts, which will be ossified as bone tissue later so as to extend the skull plates. Consequently, we can interpret that the skull development occurs at the skull

fronts where they are attached to the suture, and only occurs while the suture is stretching.

2.6.3.1 Investigate The Edge of a Skull Plate

The proliferation and ossification of bone tissues that occurs at the edge of suture contribute to the growth of skull plates, and therefore, it seems reasonable to append more elements along the edge of our skull model to simulate the skull growth. However, since our skull model is generated by two layered surface mesh (only an outline of an object), we have to cut our skull surfaces along edges in order to fill new blocks of meshes, which would be a huge and complicated work. The left side of Figure 2.14 helps to interpret this impossible work, resulting from the two layered surface meshes. In order to make the growth easier as we could handle, we decided to scale the faces that formed the skull plates so as to achieve the same effect (indicated in the right side of Figure 2.14).

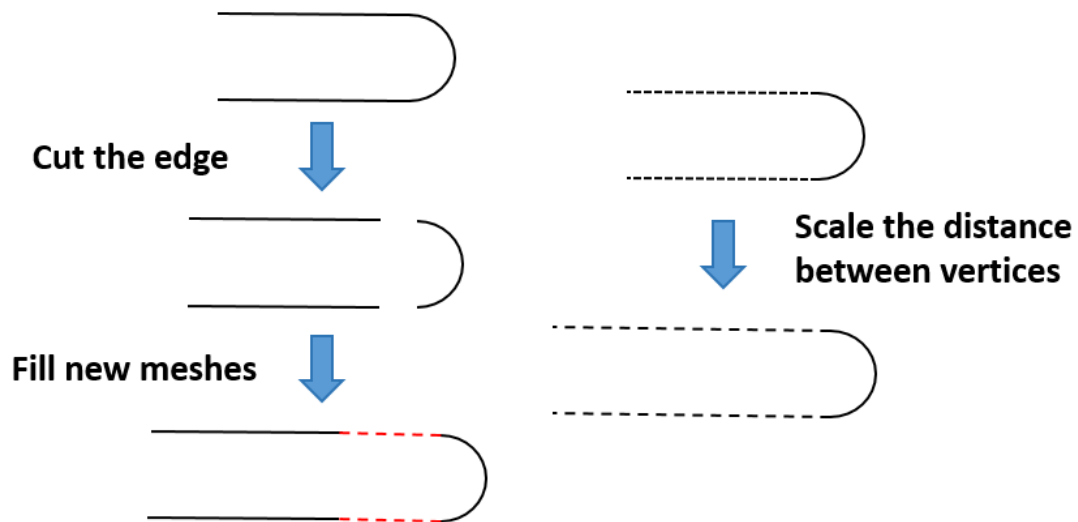


Figure 2.14: This Figure shows two ways to expand a skull plate. Left one indicates that the plate was cut at the edge, and make new mesh to fill in, whereas the right one shows to scale the skull plates to achieve the same effect.

However, as demonstrated in the right part of Figure 2.14, the edge of each skull plate that indicated with solid line should be excluded out of face enlargement. Otherwise, the shape of edges will be deformed and finally overlapped with other plates. From another point of view, if we allow all the faces on a skull plate (except the edge) to be modified, then the whole shape will be deformed, which against the purpose of setting the skull as rigid body. Therefore, we only selected a few faces that are close to the skull edges to be scaled.

To select faces that are scalable, it is necessary to recognize which vertices and faces formed the skull edges first. We used an easy but a little trivial method to detect vertices

that form skull edge. Because of the square shape of the frontal bones, our first idea is to make a sphere at the centroid of the bone plate, within where all the vertices of this bone plate should be excluded, then the rest of vertices are considered as edge. As indicated in the Figure 2.15, the edges at the left and right sides are acceptable, but the nodes at the top and bottom are too thick. So we added more spheres at the top and bottom to remove redundant nodes until the whole edge is rather thin. All of the skull plates were applied with the same process, the only difference is the number of spheres we used depending on the complexity of the shapes. In Figure 2.16 and 2.17, we indicate the edge of two other plates that have detected with respect to the vertices as small red spheres. We added all the indices of edge vertices from one skull plate into an array list respectively as the preparation of skull extension, in order to save calculation time during the simulation, and each skull plate has one edge list.

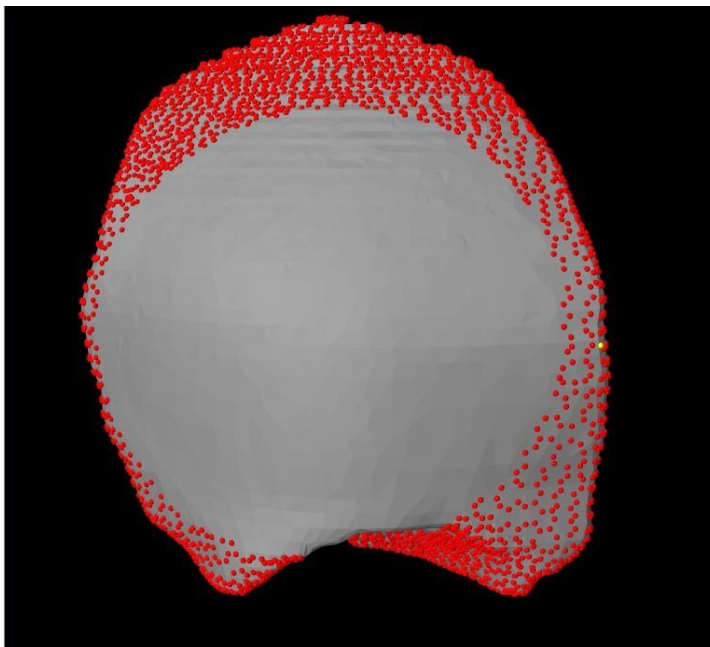


Figure 2.15: A skull plate using one sphere to explore the edge. The width of the edge at the top and bottom is too thick to be accepted.

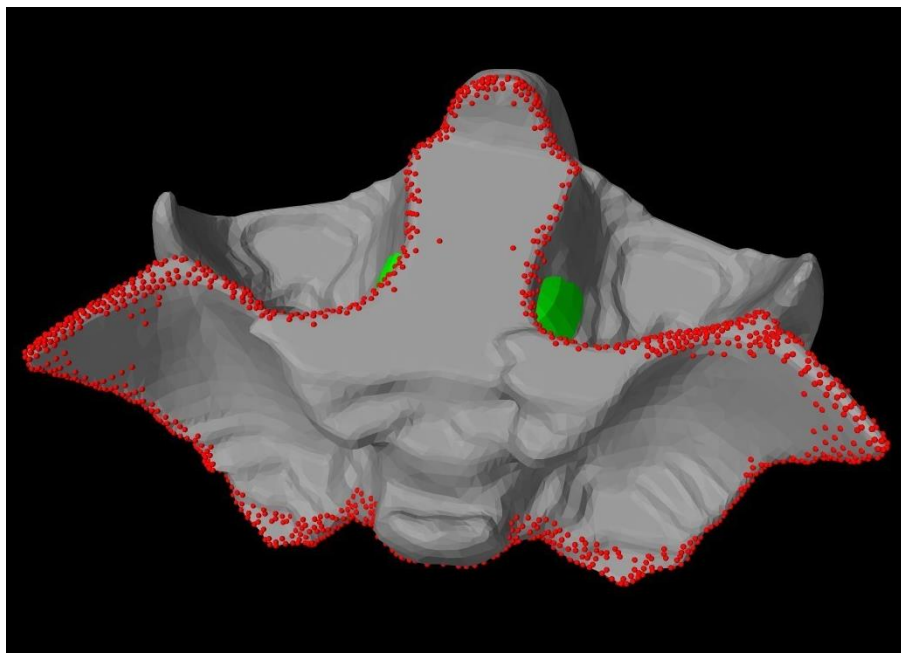


Figure 2.16: The skull plate that connected with cranial facial. The red points on the bone plate indicates this skull edge.

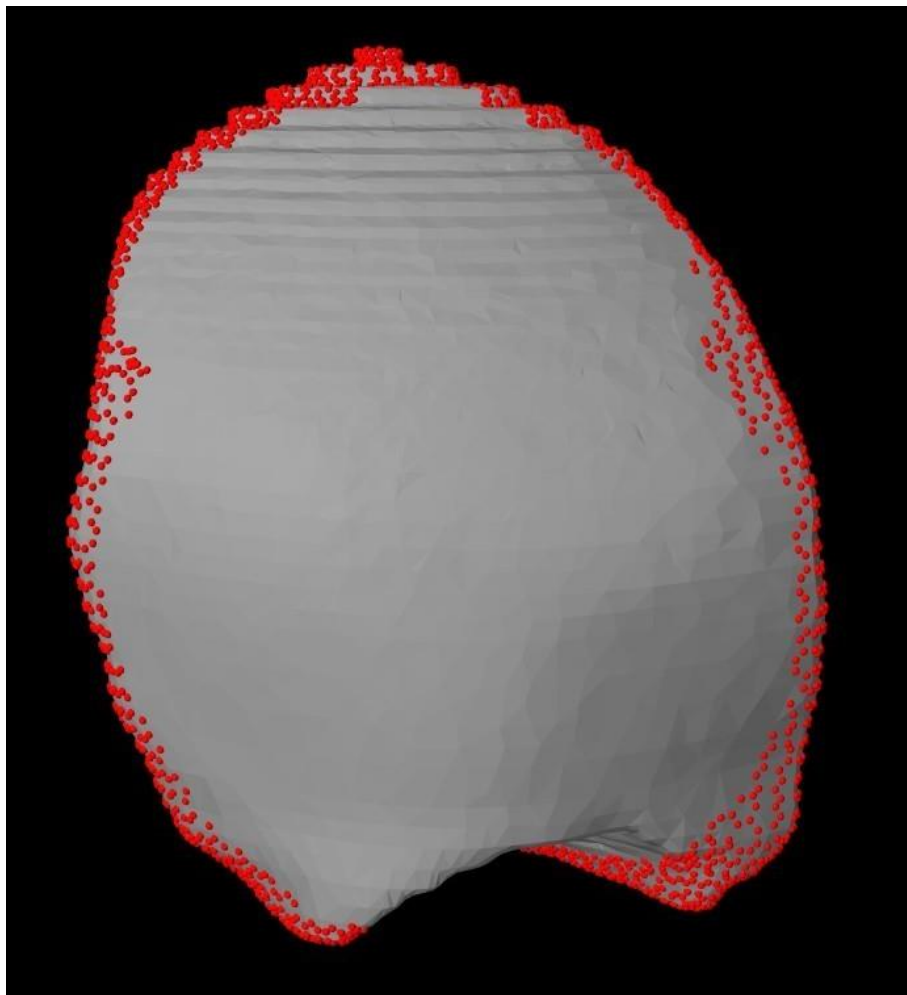


Figure 2.17: Illustration of skull edge of right front bone. The red points denote the vertices we added into the edge list.

2.6.3.2 The Skull Extension Algorithm

We believe that the extension of the skull plates that occurs on the skull fronts, are influenced by tensions exerted on the suture, which trying to shrink back to its original size. In our simulation, we used a simple way to test the stress of the suture. Once there is tension exerted on the suture, the sutures must be stretched out. Therefore, if we check the width of the suture at each time step, then it is easy to discover the stretchiness of the

sutures. In the Figure 2.18 below, there are six blue squares indicating part of our suture model, and each of the square denotes one hexahedral element of the suture model. Point A, B, C, D, O and O' denote six nodes on a hexahedral element, where nodes A, B, C and D are attached to the skull plates. We recorded the initial distance of AC and BD before the simulation, so that we could compare the changes of the distances at each time step, which will indicate whether the suture is stretched or not. As a result, all the distances between the two attached nodes, such as AC and BD, are stored in a list before the simulation (all the sutures has only two elements along the horizontal direction). Once the suture is detected as being stretched, we will make it move back, trying to maintain the relative position between each attached node and its corresponding middle node (e.g. \overrightarrow{AO} , \overrightarrow{CO}). Moreover, we also make a three column suture nodes list, where each row contains three nodes of suture (such as AOC and BO'D). With this list, the suture stretchiness can be detected faster at each time step.

In addition, once the suture was stretched, if we only shrink the suture back to original size, then the suture will be separated from the skull. Therefore, we should enlarge the skull plates along with the suture so as to grow the skull plates. However, for one suture that is attached to two plates, the stretched distances along this suture might not be the same (shown as Figure 2.19).

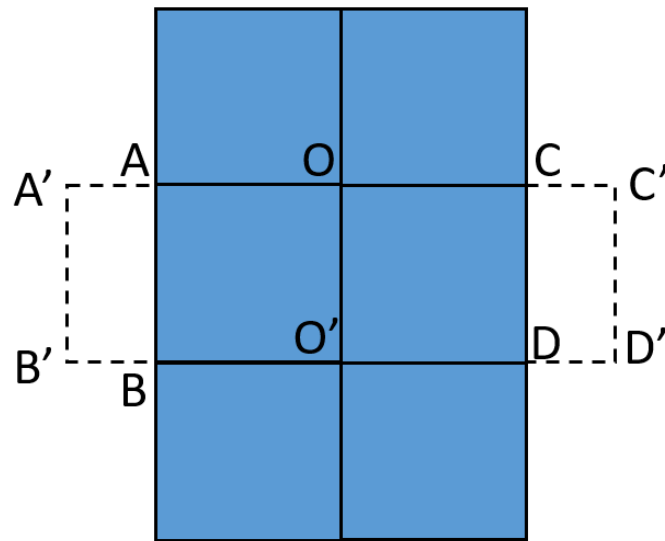


Figure 2.18: An indication of suture stretch. The six blue squares are part of suture, and the dashed line shows the stretch of the suture.

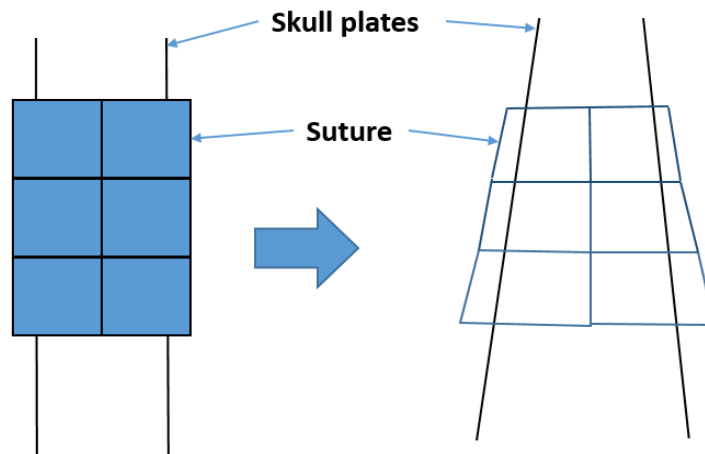


Figure 2.19: An indication that changes of the width of a suture could be variant under some circumstances.

Since the edge of a suture is attached to the skull plates by nodes, we further grouped the vertices on each skull edge into smaller regions, each of which is accordingly centered by one of the attached suture node. Figure 2.20 interprets the subdivisions of the edge for the right frontal bone. Those transparent yellow spheres illustrate how we decide the area of each region, which might be overlapped with its neighbors, whereas green points are suture nodes attached to skull and red points are nodes that are not attached. The stretchiness of suture that is measured on each attachment only affects vertices within its bonded small region. The size of these regions is varied depending on the size of the suture elements depending on the attachments. Notice that the yellow spheres overlapped with each other, which means some vertices might be controlled by two attachments. We finally decided to only bond this type of vertices to a closer suture attachment to avoid over growth.

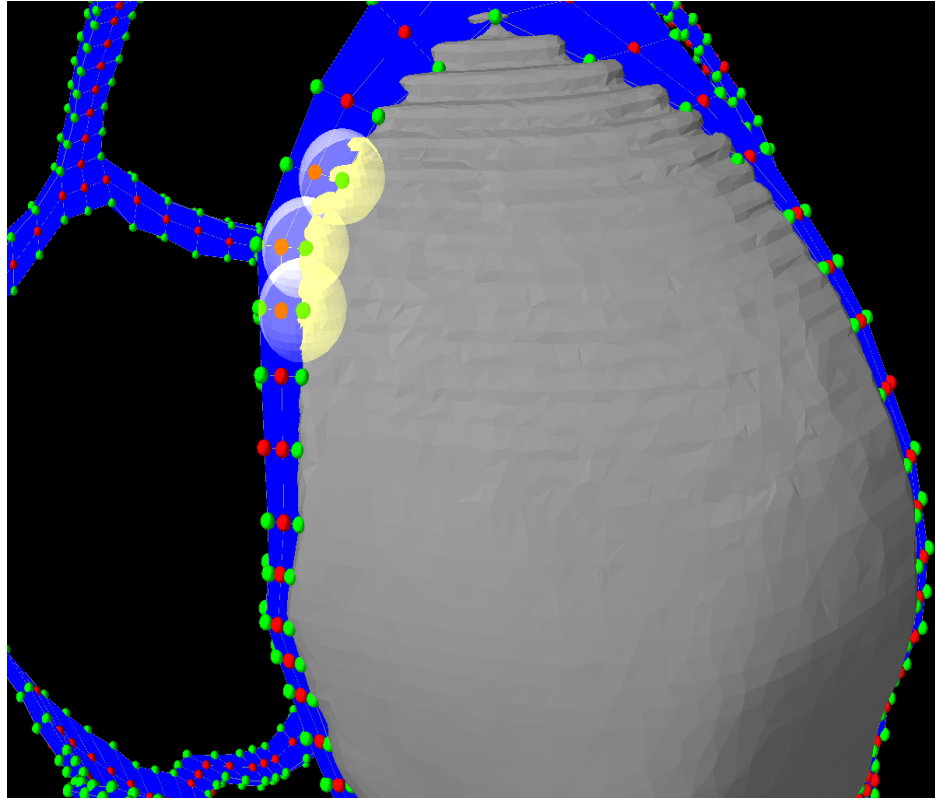


Figure 2.20: The attached suture nodes in green are the centers of each sub-regions. In order to make this picture clear, we make other plates invisible except this right frontal bone.

After bonding each small region of the vertices on the skull edge to its closest attached suture node, our next task is to build mathematics to allow suture shrink back once it is stretched, and in the meantime move each bonded skull edge region along with the suture node. As a summary, the task is to design an appropriate way to shrink the suture back to its normal once it is stretched.

The suture can only have two statuses during the head development, one is being stretched, the other is to go back to its original size. We did not concern ourselves with how the suture is being stretched, but once it occurred, it is our work to move back the

attached suture nodes to the positions that keep the original width of the suture along the stretching direction. In Figure 2.21, we demonstrate how a stretched suture attempt to shrink back to normal size with different tension applied on it. However, we didn't want the suture shrink back to the original size immediately once the displacement was detected. For every time step, we only made each stretched attachment move back half of the distance that it deviated from original. As a result, the procedure that the suture grows back to normal size will be smooth. The skull extension will be implemented then by moving the vertices within the small regions on the skull edge the same distance and same direction whenever the position of the corresponding suture node was adjusted.

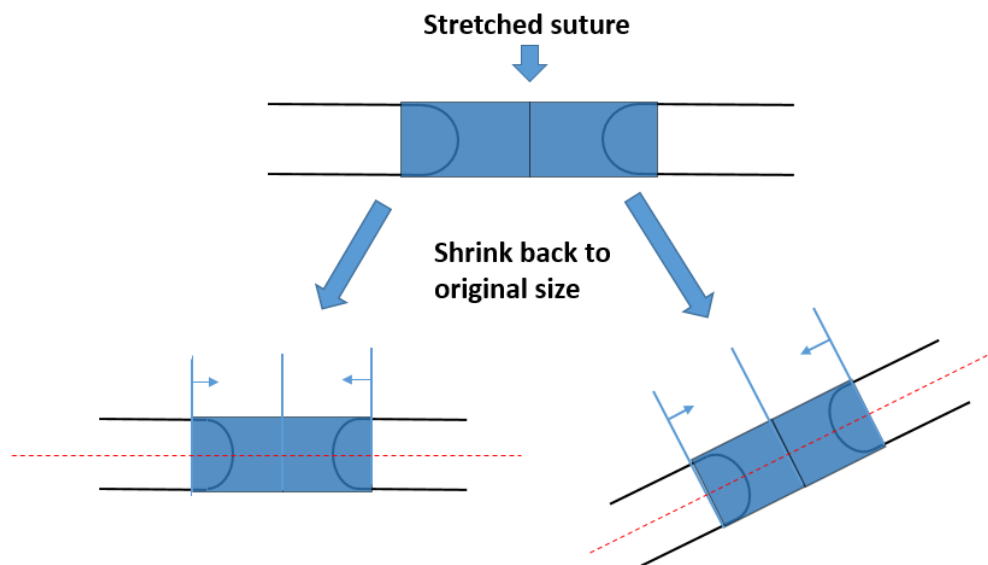


Figure 2.21: The suture shrink back to normal size along the direction of the tension exerted on it. The blue squares are represented as the cross-sectional view of the suture, where the shapes outlined with black lines indicated as skull plates.

2.6.3.3 Issues Caused by Sutures Overlapping

As mentioned in the previous section, we further segmented our suture model into three individuated objects with different mechanical features. In order to make them appear as a whole, we overlapped these sutures at the edge. This caused an issue during the simulation while the displacement of suture was detected at these overlapped areas. Those suture nodes that located at the same place, made the associated regions on the skull edges were bonded to two nodes, which were connected to different middle nodes along different direction. Therefore, when we shrink one of these two nodes back along one direction, the other node should be moved to the same place.

2.7 Set Land Markers On the Skull

The reference landmarks were manually placed on the skull to observe the length, width, height of the head during the simulation. Therefore, six markers were chosen on the left, right, top, bottom, front, and back of the skull respectively, shown in Figure 2.22 as red points. Consequently, after a simulation, we will see the trend of cranial index (normally the relation between the skull width and length) over time, so as to quantitatively evaluate our simulated head development.

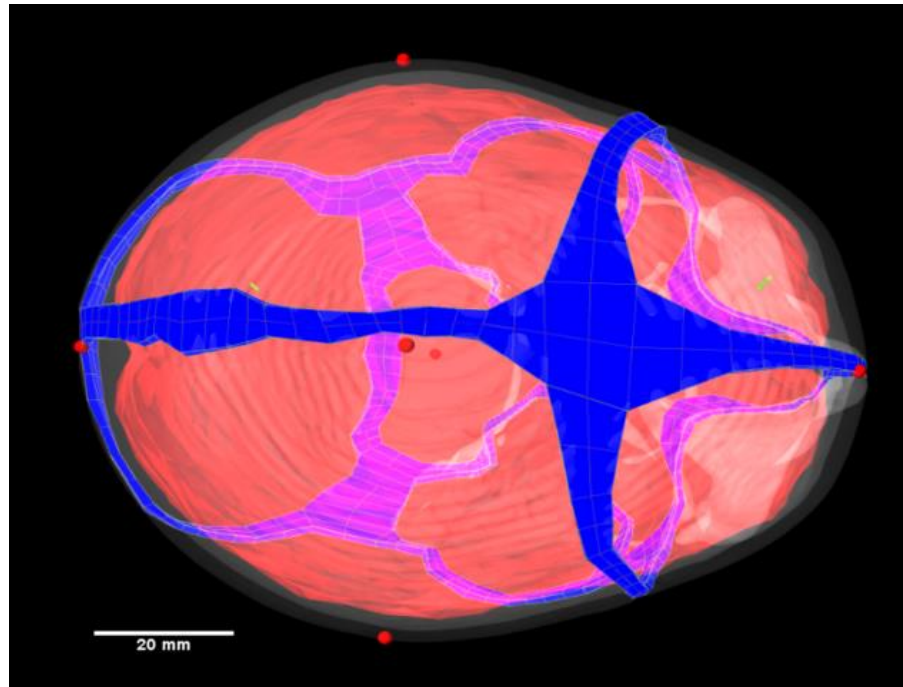


Figure 2.22: Six reference markers are set on our normal skull model, to calculate the skull width, length, and height. The six markers are indicated as red spheres, located at the left, right, front, back, top and bottom of the skull respectively. Image from (Jin et al. 2013).

2.8 Results

2.8.1 Simulations with Only Brain Expansion

Before simulating the head development with both brain expansion and skull extension, we first tested how a normal skull would grow with only an increasing brain. During the simulation, we applied stress map on the suture model, showing from blue as no tension to red as maximum (the threshold can be customized). By measuring the length, width, and height of the skull as established by reference landmarks we set, we were able to

measure the standard Cranial Index (CI). We were also able to calculate the skull volume development over time. The properties were setup as follows in the following simulation run:

Brain growth ratio = 0.02; Time step = 0.001; Time duration = 6.3 s; Calculating time interval = 0.1 s. In Figure 2.23, the x-axis is the time line with the unit of seconds. The blue diamonds are the maximum length of the head, while the blue "+" shapes are the maximum breadth of the head and the blue asterisks are the height. The unit of these three is millimeter (mm) referred to the left blue y-axis. The red circles are the volume of head by cm^3 indicated with the right red y-axis. Figure 2.24 illustrates the cranial index during the simulation. The simulation was run as a set of 1 second epochs, except where multiple surface-to-surface collisions required finer temporal step analysis. The head length grew from 106.46 mm to 123.07 mm with 15.6% increment whereas the head width increased 24.6% at the end of simulation. In other words, the head circumference increased by approximately 20%.

From time 0 s to 2.3 s, the length, width and height were all maintained at the same level, since we initialized the brain at 5 percent lower volume to ensure the hybrid model was totally stable while initializing the run sequences within the Artisynt software. As the brain was allowed to increase in volume, the surface contacts were then transformed into stresses along the sutures. After 2.4 s, the height began to grow first, the breadth grew in the following two time-interval and the length stayed still until 3 s. As in normal developmental cases, the breadth of the head grew faster than height. At 6 s, the breadth and the height seems to achieve the apogee, the values began to retain whereas the length kept growing all the time.

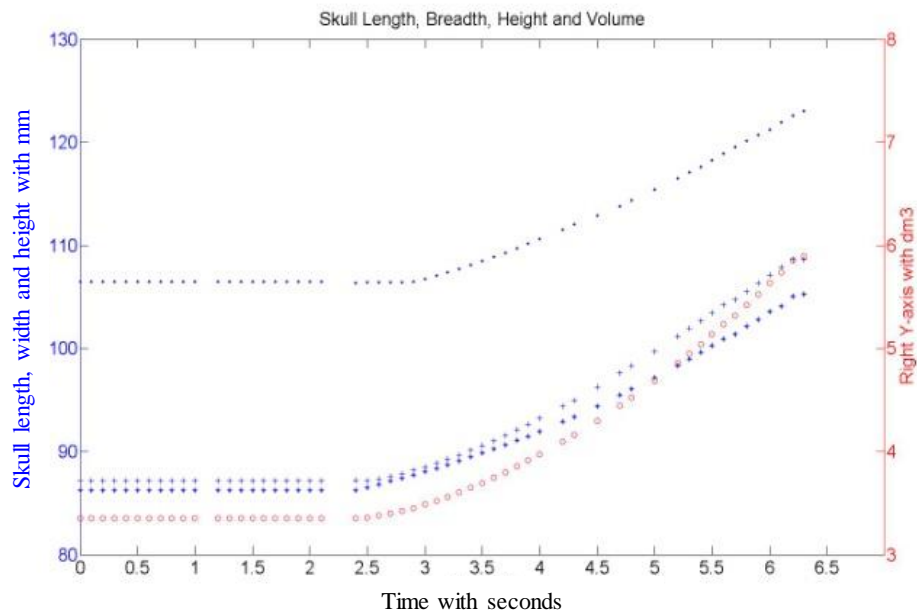


Figure 2.23: The length, width, height and volume measurement with respect to time during brain-skull growth. Left Y-axis represented the scale of skull with unit of millimeter (mm), right Y-axis indicated the volume of the skull with unit of dm^3 , and x-axis represented time with seconds. Image from (Jin et al. 2013).

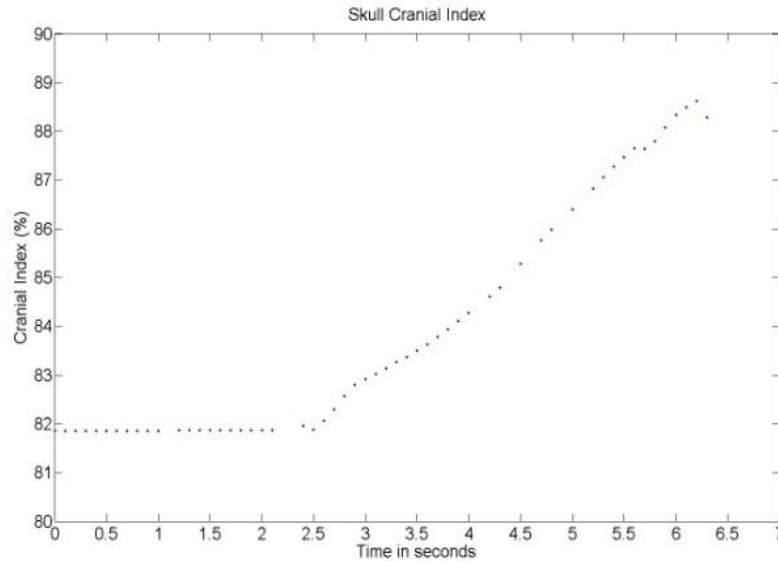


Figure 2.24: The values of cranial index over time during the simulation, which is the relation between skull width and skull length. Image from (Jin et al. 2013).

Figure 2.25 is one of the screenshots in the middle of the animation, showing tensions on suture (tensions that caused by stretchiness). Red areas pointed by arrows, indicates partial areas of stretched suture, which contribute to the growth of breadth and height, was stretched the most.

It is clear that the volume of skull increased quickly along the timeline and the ratio of growth decreases monotonically after reaching a peak. The cranial index increased slowly from 81.64 at 2.6 s to 88.62 at 6.2 s, which is the peak of this line, then started to go down for the reason that the breadth began to saturate while the length was still growing.

Figure 2.26 is taken at the end of the animation, showing two yellow areas for the potential further growth of length, and too stretched for breadth and height to grow.

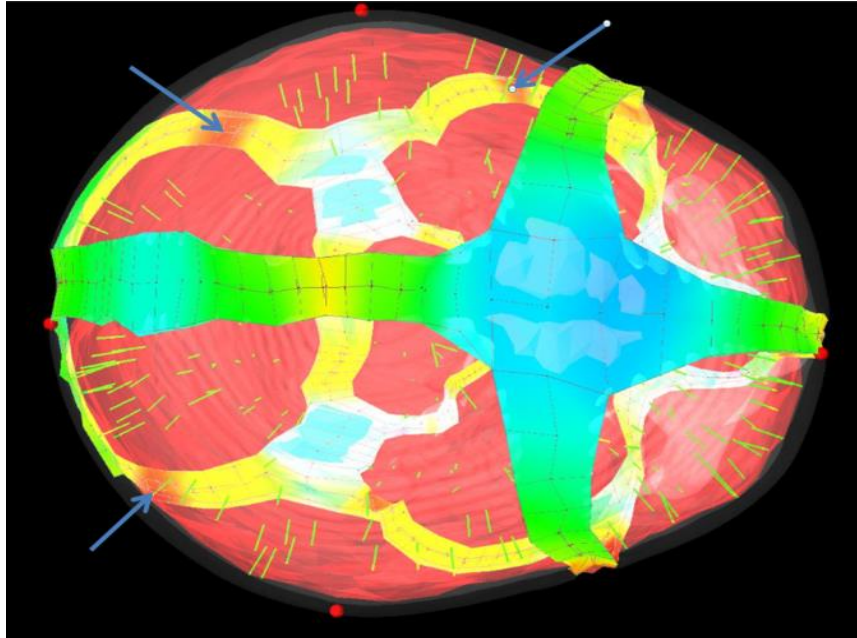


Figure 2.25: A screen shot of our head model in the middle of the simulation with color map of stress showing minimum as no tension to maximum as red. Image from (Jin et al. 2013).

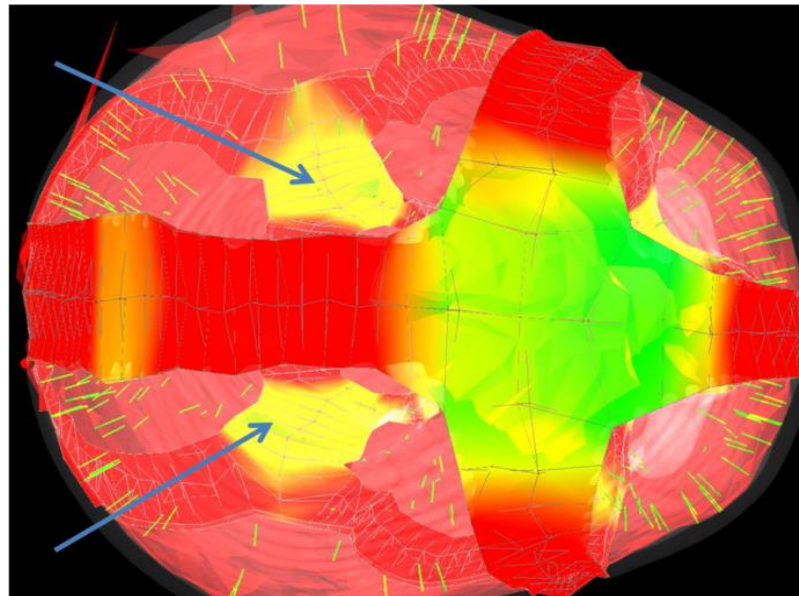


Figure 2.26: A screen shot of our normal head model at the end of the simulation.

Image from (Jin et al. 2013).

2.8.2 Simulations with Skull Plates Extension Added

In this section, we will show the results with complete simulation algorithm, which includes both the growth of brain volume and the extension of the skull fronts. We simulated normal head development and three common types of craniosynostosis (scaphocephaly, trigonocephaly and plagiocephaly), all of which have typical skull shape that could help us to qualitatively evaluate our current simulation algorithm.

2.8.2.1 The Simulation of Normal Head Development

For this simulation, we set time step (0.0005) smaller compared to the simulation with only brain expansion, since this program involves much more calculations and we try to keep the model as stable as possible. Six reference markers are located at the same position as previous simulation. The bottom plate, which is created to fill the hole that pass the spinal, was fixed to stable our model. We attempted this simulation as long as possible until the interaction between the growing brain and skull lost balance.

The Figure 2.27 below is a screenshot of the original status of our head model. Again the color map of stress was applied on the suture, currently showing blue as no tension. The brain model was shrunk back to 97% of its original size, in order to guarantee a completely steady model at the beginning of the simulation. Figure 2.28 and 29 indicated the deformation of our normal head model at the end of the simulation from different

angles. As mentioned in previous section, we separated our suture model into three pieces, where two of them are connected with cartilaginous bone plates, one of which traverse the cranial face, another is located at the cranial base. The bone plates attached to these sutures grow much slower than other places. As a result, in our simulation, there is no skull extension around these two suture, only with suture stretchiness. From the Figures we can see that all the membranous bone plates expanded with a certain amount compared to the original skull.

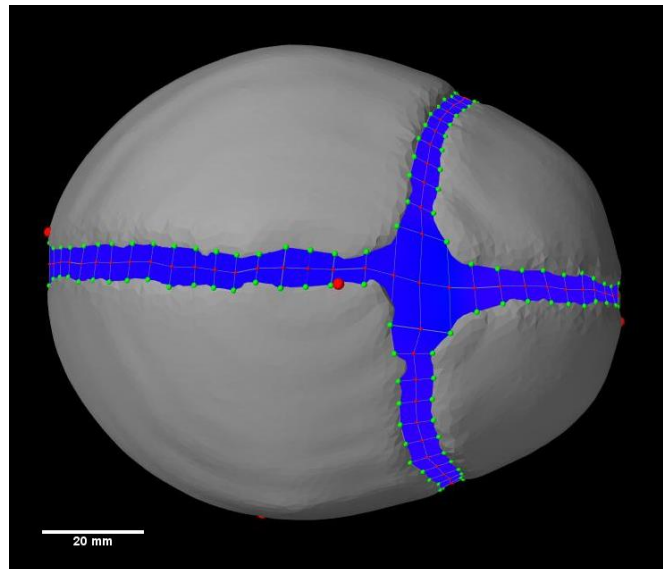


Figure 2.27: Original status of our normal skull model, and the brain model was placed inside the skull. The red spheres are reference markers.

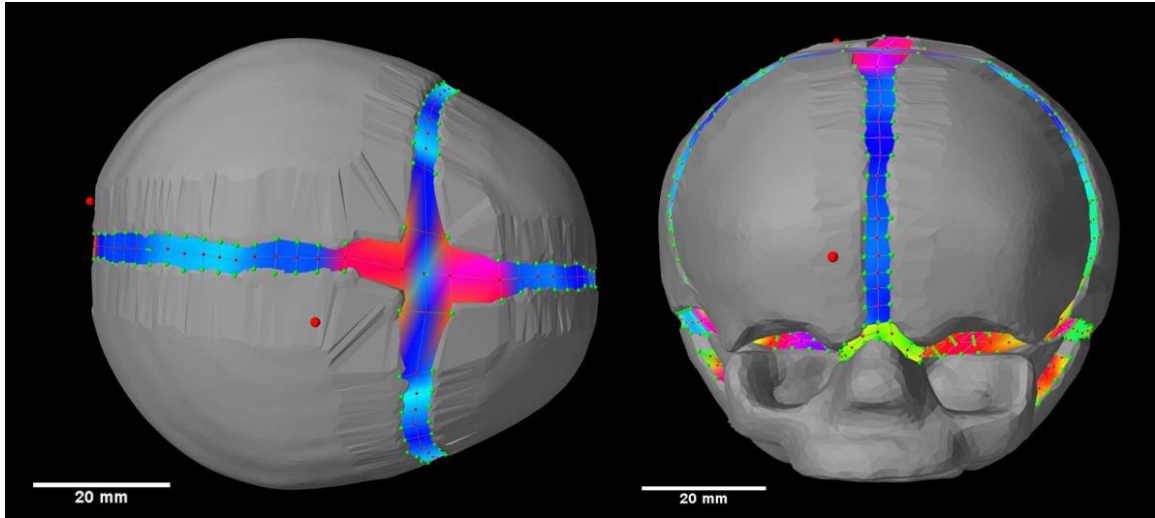


Figure 2.28: A deformation of our head model at the end of our simulation, left indicated from top view, and right displayed from front view.

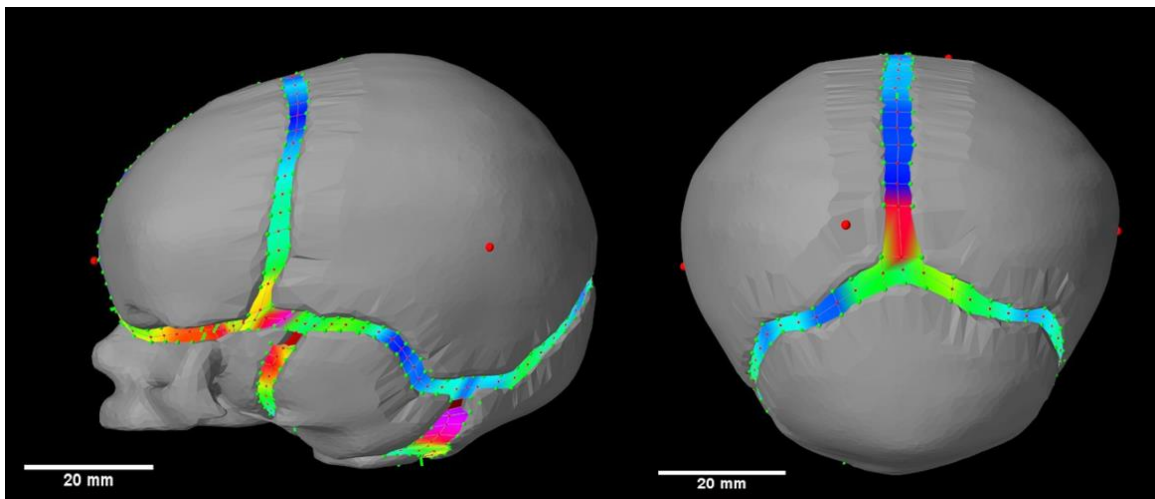


Figure 2.29: A screenshot of our normal head model in the end of the simulation, left showed from left view, and right indicated from back view.

In Figure 2.30, we plotted the cranial indices that measured frequently during the simulation with respect to time, where x-axis indicated time with unit of second and y-axis represented possible values of cranial index. From 0 to 9 seconds, it is obvious that

the cranial index slightly dropped from 81.5% to 81.1%, but start to escalate quickly from 9 to 22 seconds. After 22 seconds, the cranial index still tried to maintain the trend of growth but with a gentle slope.

At the beginning, the shrunken brain that is completely separated from the skull start to grow in order to reach the brain. Before the whole brain completely filled the intracranial space, we guessed some part of the brain achieved to skull the skull first than other part, causing some imbalance among the skull plates, which also lead to the descending trend of the cranial index. The rising tendency of the cranial index after 9 second increased linearly and started to slow down from 22th second. We guessed the decline of the growth ratio hinted out the imbalance of our head model. Therefore, we will only take the values between 9 to 22 seconds as available results.

In summary, our simulation with a normal head model developed such a growth pattern that the cranial index has a linearly increasing tendency while the brain volume is expanding linearly and all the sutures maintain open.

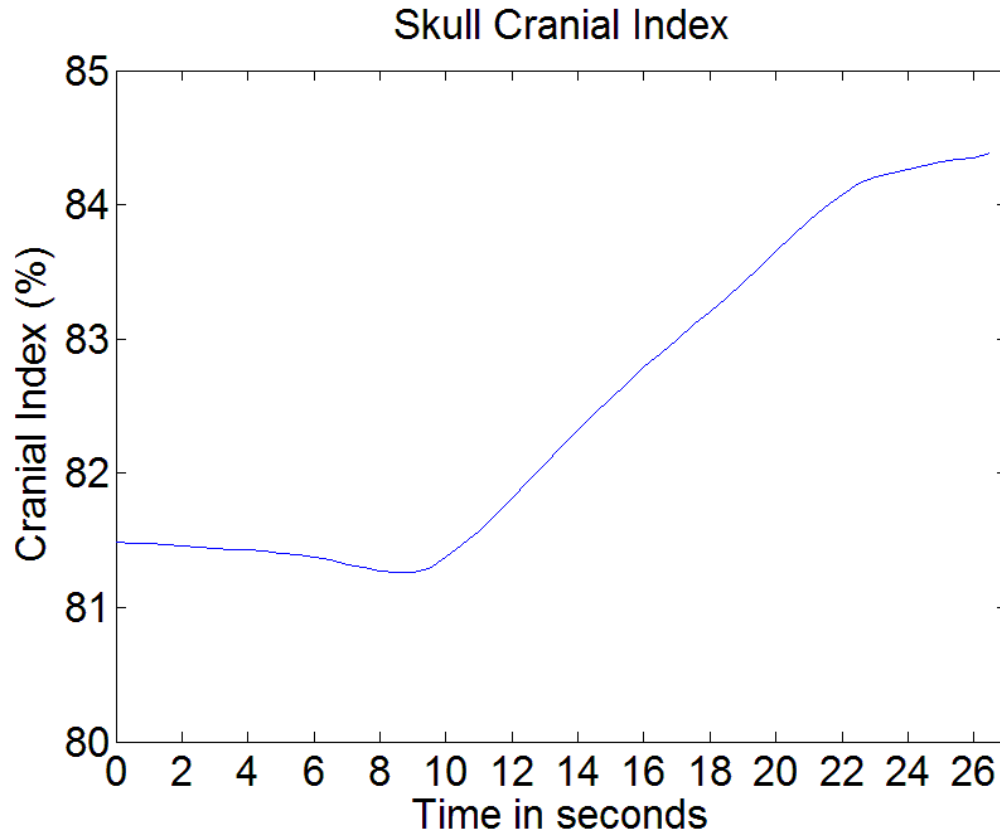


Figure 2.30: The values of cranial index calculated at each time intervals during the simulation, where x-axis represented time in seconds, y-axis denoted cranial index.

2.8.2.2 Scaphocephaly

We have modified our normal head model by closing the sagittal suture and combining the left and right parietal bones, we obtain a scaphocephaly model. In Figure 2.31, we indicated a screenshot of the original status of our scaphocephaly simulation. Currently, the skull shape was the same as our normal skull. Figure 2.32 represented the status of our scaphocephaly model at the end of our simulation. We can see from the top view that both frontal bones grew slightly in lateral direction, whereas in longitudinal direction the

frontal bones and parietal bone extended much more. The simulation of this scaphocephaly model lead to a very long head shape, which consists the fact.

In Figure 2.33, we illustrated the values of cranial index of our scaphocephaly model during the simulation. From 0 to 8 seconds, the cranial index maintained at the same level since the brain had not completely fill the intracranial space. After 8 seconds, the cranial index started to steadily fall down. It is obvious that because of the fused sagittal suture, the width of the skull was fixed while the length of the skull is growing, which occurred at the coronal suture.

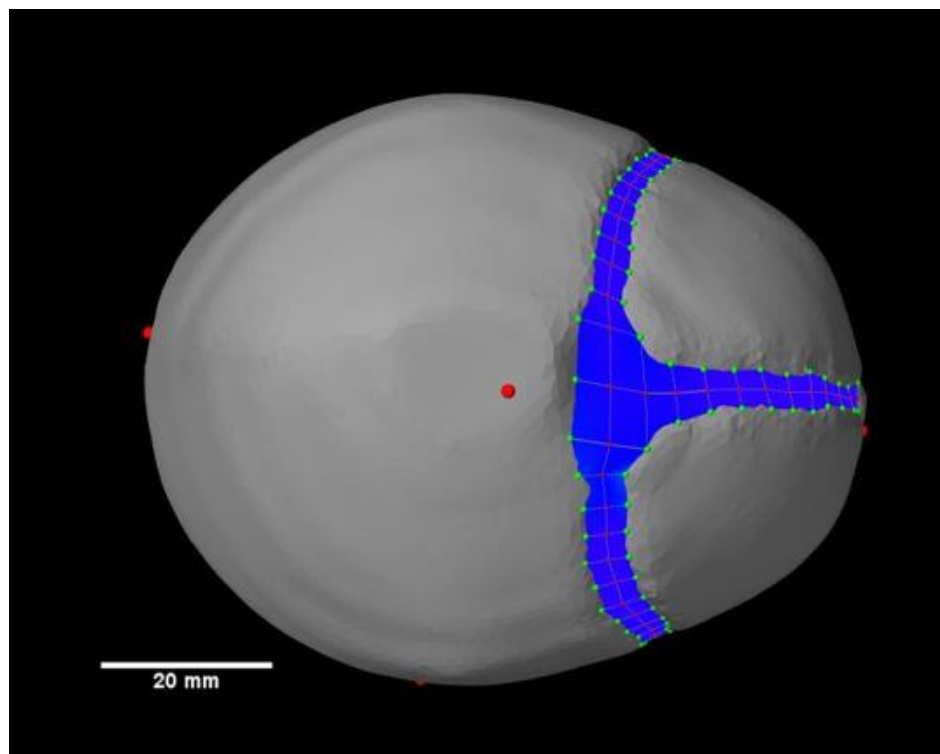


Figure 2.31: The original status of our scaphocephaly model, where the sagittal suture is closed.

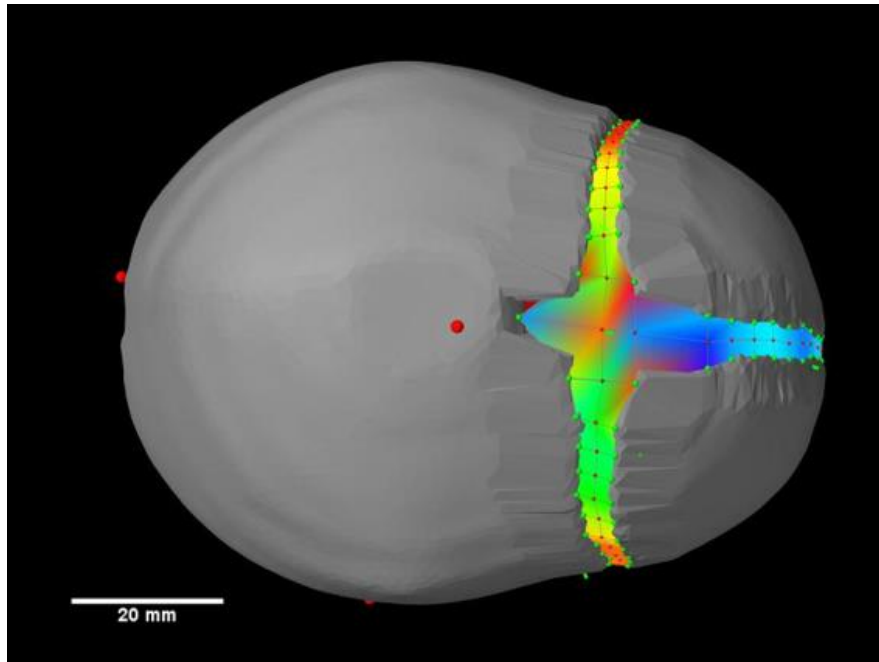


Figure 2.32: A screenshot of our scaphocephaly at the end of the simulation, showing a long head shape.

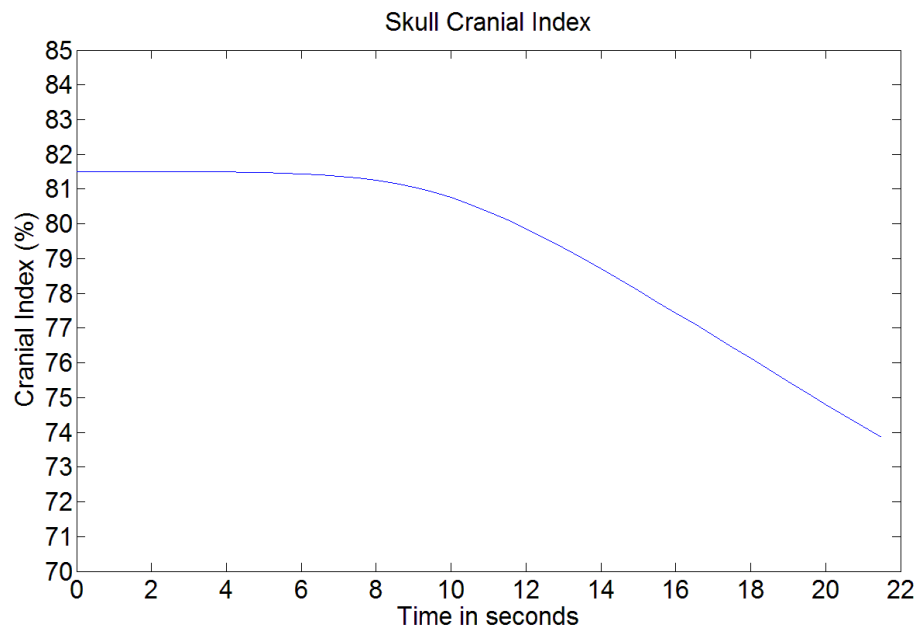


Figure 2.33: Cranial index values of the simulation of scaphocephaly.

2.8.2.3 Trigenocephaly

We combined the left and right frontal suture to develop trigonocephaly model. Figure 2.34 displayed our trigonocephaly model without frontal suture. After the simulation, we can see from Figure 2.35 that the frontal bone still keeps the original shape, whereas the posterior cranial vault was inflated in both lateral and longitudinal direction. The skull shape was similar with the normal head but with a smaller forehead.

Figure 2.36 indicated the cranial indices during the simulation, which has an increased trend like our normal head simulation. Noticed that with the same brain growth ratio, the cranial index value of trigonocephaly simulation grows only to 82.8 at 25 seconds, while the value of our normal simulation achieved to 84 at 22 seconds. It demonstrated that the closed frontal suture somehow impeded the expansion of the brain so as to decrease the ratio of cranial index development.

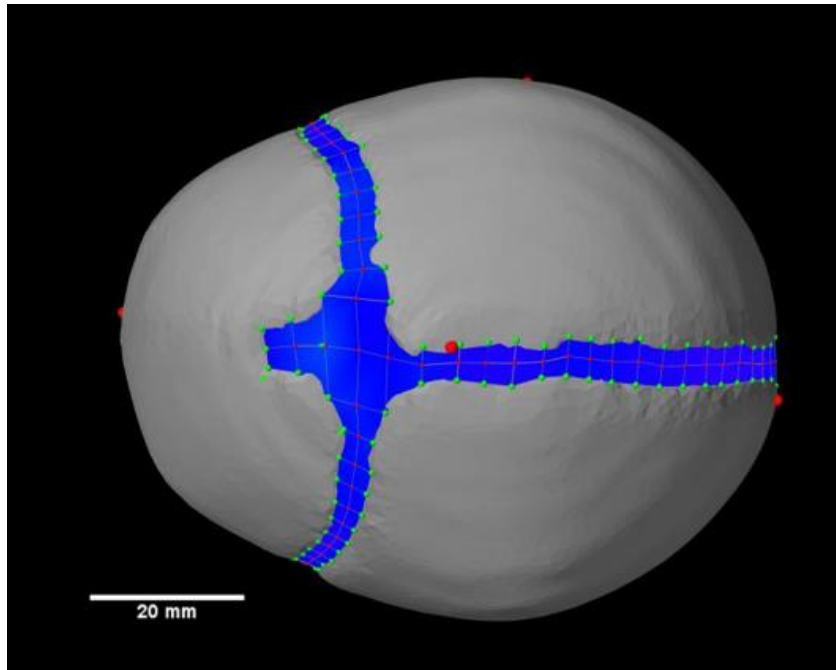


Figure 2.34: Initial status of our trigonocephaly where the frontal suture was closed.

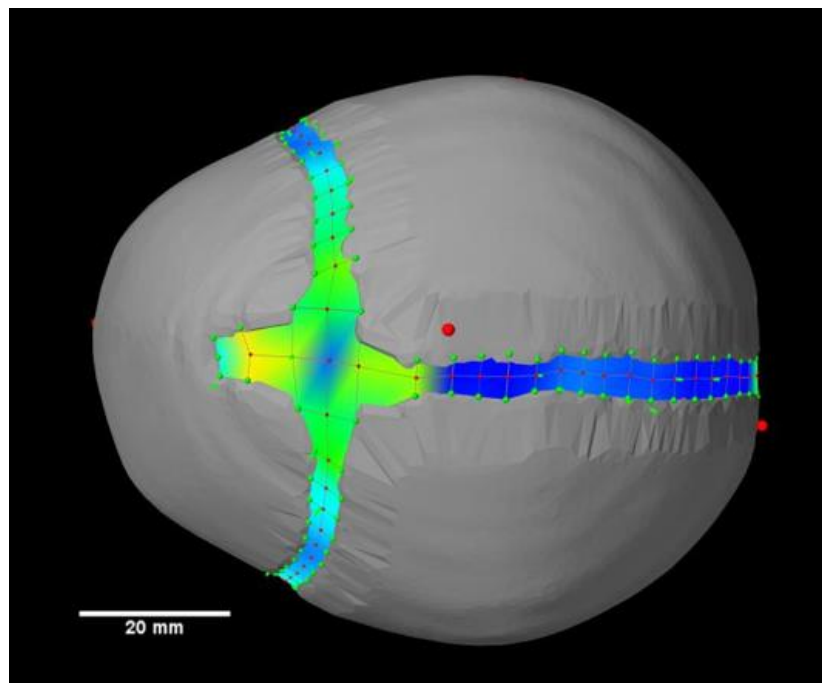


Figure 2.35: The result of the simulation with closed frontal suture.

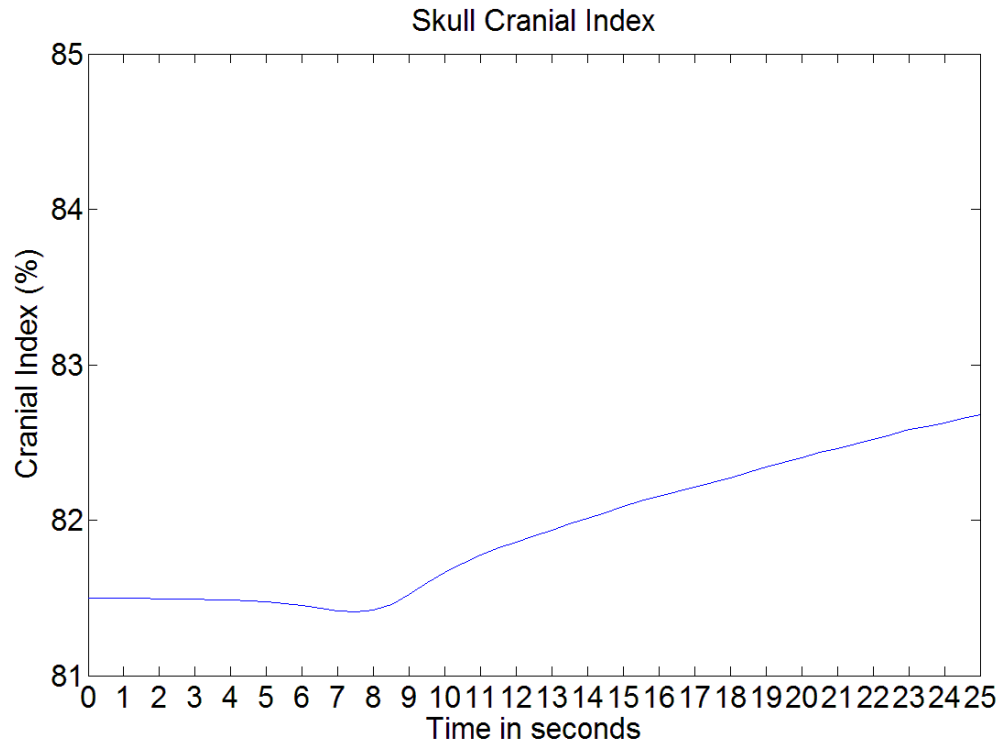


Figure 2.36: Cranial index values during the simulation of trigonocephaly model.

2.8.2.4 Anterior Plagiocephaly

With reliable results from the two abnormal simulations, we attempted to further simulate the development of anterior plagiocephaly. Figure 2.37 shows two screenshots of our model during the simulation, one is at initial, one is in the middle. However, the skull shape did not have obvious deformation at the left side, where the coronal suture was still open. It conflicts with the fact that a skull of plagiocephaly has a protrusion at the side with open coronal suture. In our case, the left frontal bone should grow forward to make an uneven forehead.

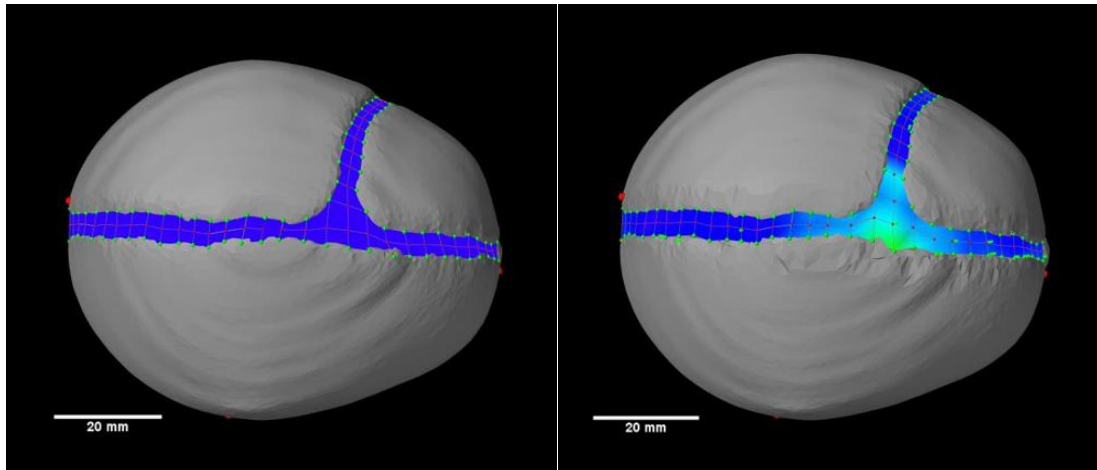


Figure 2.37: a) Initial plagiocephaly model. b) Plagiocephaly model in the middle of simulation.

2.8.3 Results Discussion

Although the simulation results of scaphocephaly and trigonocephaly were qualitatively correct, it is obviously that the simulation of anterior plagiocephaly did not match the truth. While the skull grew normally in the later direction, the unaffected side of frontal bone did not protrude forward as expected. One possible explanation is that the deformable brain model did not interact correctly while it is being compressed, which we cannot control since this behavior was calculated by the system itself. In addition, the collision detection between the brain and the skull caused a huge amount of calculations during the simulation, leading to one simulation last at least one week to finish.

Furthermore, the model was not stable during the simulation, often exited earlier than expected from collision behavior failed. Therefore, we decided to adjust our algorithm in order to avoid the calculation of collision detections. In the next chapter, we will discuss our alternative simulation algorithm in detail.

Chapter 3

3 Head Development Simulation with Force Based Model

3.1 An Alternative Simulation System

The previous simulation algorithm requires huge amount of calculations, resulting from the large amount of nodes from our brain and skull models and the collision detections between the skull plates and the brain model. In addition, these interactions between the brain model and the skull model made our simulation unstable that could end our calculation much earlier than expected. Therefore, we developed an alternative algorithm to substitute our brain model.

3.1.1 Algorithm Specification

The purpose of our brain model is to push our skull plates outward so as to develop the skull plates. As a result, instead of using the brain model itself, we could exert forces on the interior surface of the skull model to push it outward. Now our task is how to distribute the forces to achieve the same effect as brain expansion.

In Artisynt, we can attach a force point on a surface with a specific direction and scale.

We decided to add a force point on each triangular face of the inner skull surface (without edge faces). The direction of each force is the opposite of its face normal. Each force value is decided by:

$$fo_i = \frac{s(fcen_i - scen)}{1 + d_{\max}} \cos \theta_i \quad \text{Equation 3.1}$$

Where fo_i is the force applied on an face $face_i$, s is a scale, $fcen_i$ is the center of the face, $scen$ is the centroid of our skull, d_{\max} is the maximum distance between the skull centroid and an inner face of skull, and $\cos \theta_i$ is the angle between the face normal and the direction along $(fcen_i - scen)$ (Figure 3.1).

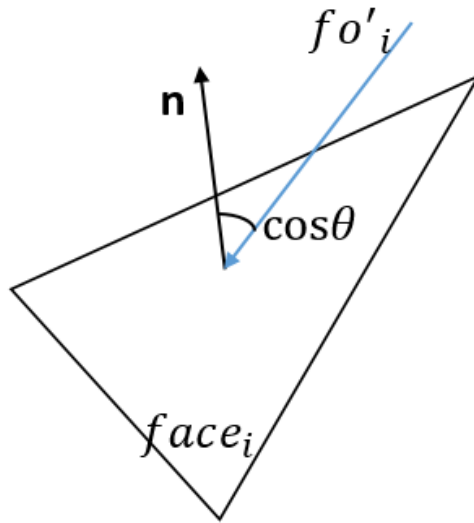


Figure 3.1: An indication of the relationship between face normal and the force fo'_i .

3.1.2 Parameter Specifications

For this new simulation system, we still used the same material properties shown in table

1. Our materials involved skull, brain and sutures, and the properties to characterize a

material includes density, Young's modulus and Poisson's ratio. As a reminder, we further segmented the suture model into three parts with respect to the different tissues the sutures formed by. The two sutures that are illustrated in Figure 3.2 were responsible to secrete cartilaginous tissues to its attached skull bones. Bones surround these two sutures grow slower than membranous bone plates, and these two sutures are harder. Therefore, in all the following simulations, we set the Young's modulus of these two suture 5 times the value shown in table 1.

All the other parameters are needed during the simulations were settled the same value for consistency. Time step is a parameter to control the frequency to calculate the dynamic behaviors and interactions between the models, in our system, set as 0.0005 second. Since we used force to simulated the actions of the brain, therefore, it is necessary to set the original scale of any force, which is $50000 \text{ g}\cdot\text{mm}\cdot\text{s}^{-2}$ in our case.

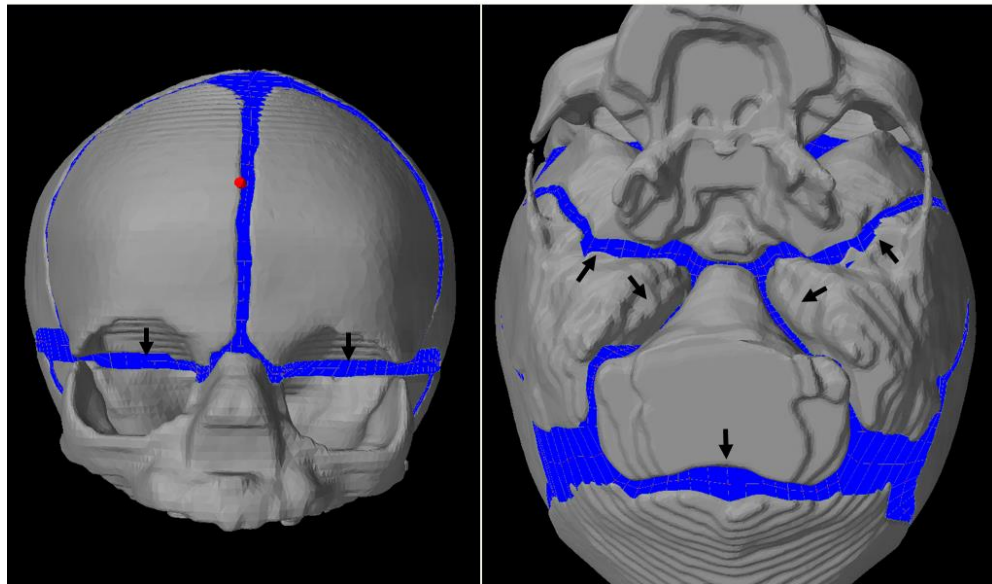


Figure 3.2: a) One of the suture that was segmented from original model, crossing the cranial facial bones. b) The other suture we segmented, located at the cranial base.

3.2 Results

3.2.1 Anterior Plagiocephaly

Since in the previous simulation algorithm, we found issues in the plagiocephaly simulation, so we decided to show the same simulation with current algorithm for comparison. Before that, let us remind the typical skull shape of this type of pathologies. The closed coronal suture can be occurred on either side of the skull. Such patients should have a protrusion on the forehead at the unaffected side, and a relative compressed eye compare to the affected side.

Compare Figure 3.3 to 3.4 from top view, it is obvious that the skull was expanded in lateral direction, whereas in longitudinal direction, the right side maintained the same while the frontal bone at the left side grew forward to form an uneven forehead.

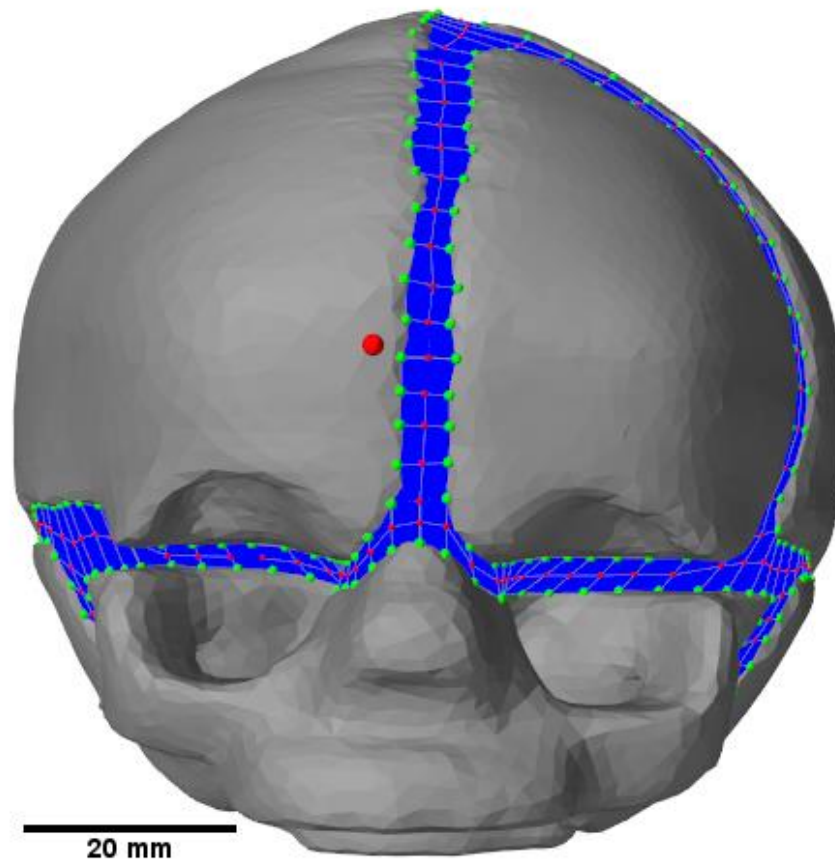


Figure 3.3: Initial model of anterior plagiocephaly by closing the right side of coronal suture.

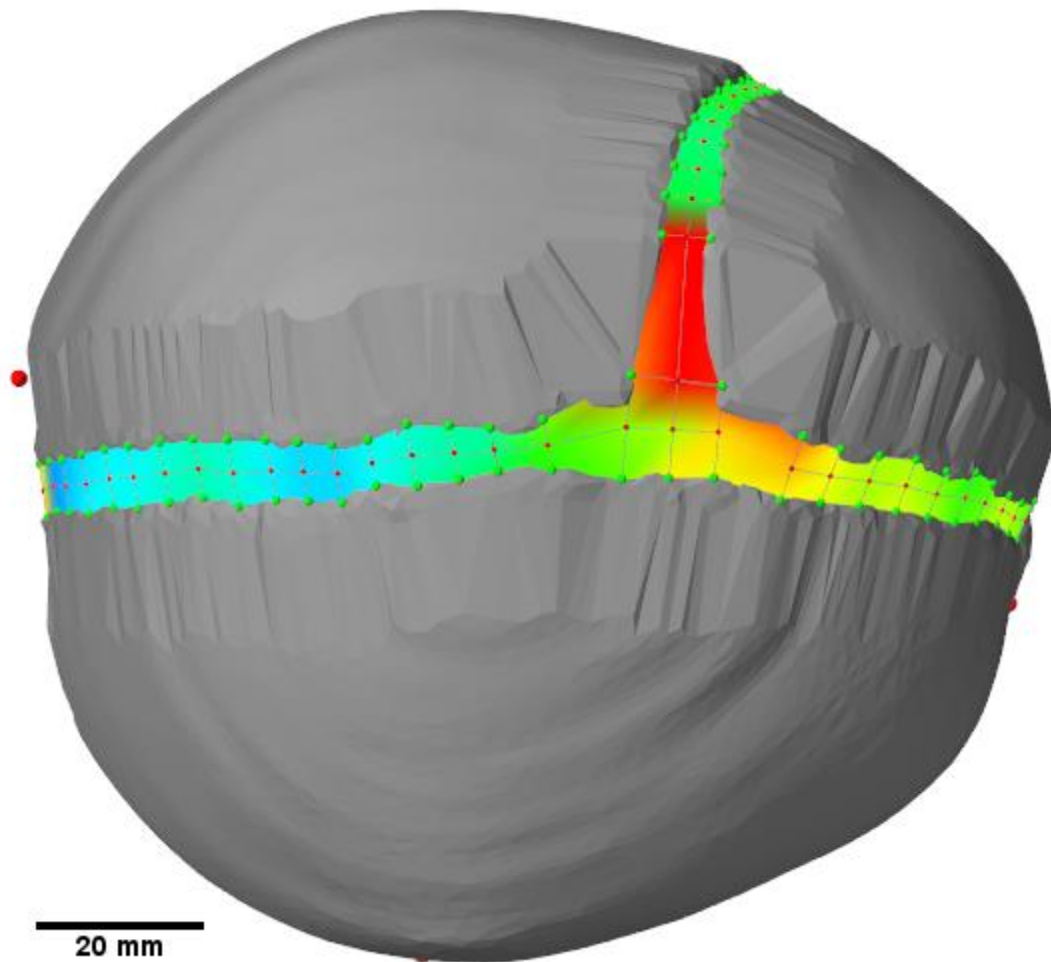


Figure 3.4: Top view of our plagioccephaly model in the end of the simulation, the opened frontal bone was protruded while the affected side remained original status.

Figure 3.5 indicates our initial plagioccephaly model from front view, whereas Figure 3.6 illustrates our plagioccephaly model at the end of the simulation from front view. The yellow dashed line in Figure 3.5 is tangential to the ridges of the eye sockets on both sides, whereas a paralleled dashed yellow line in Figure 3.6 only touched the ridge of right-sided eye socket. It is obvious that the unaffected eye socket in Figure 3.6 was slightly compressed compared to the affected side whereas at the beginning of the

simulation, both the eye sockets have the same size. Since in our model, the suture across the face can only be stretched, and its maximum displacement should be the same on both sides. On the affected side, the frontal bone was pulling upward, while on the unaffected side the frontal bone was pulling not only upward but also forward, resulting in a tilted (forward) frontal bone with the ridge moving down a little bit compared to affected side.

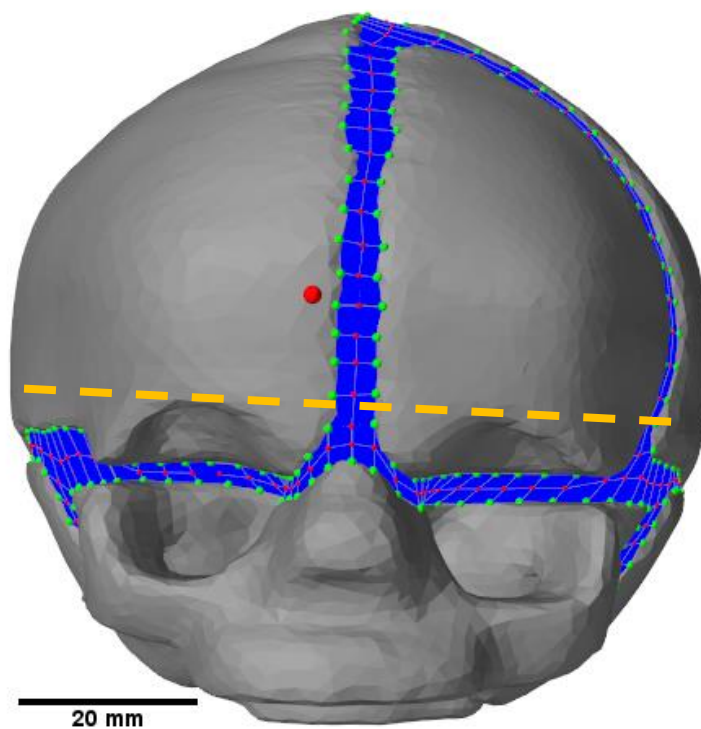


Figure 3.5: Front view of our initial plagiocephaly model.

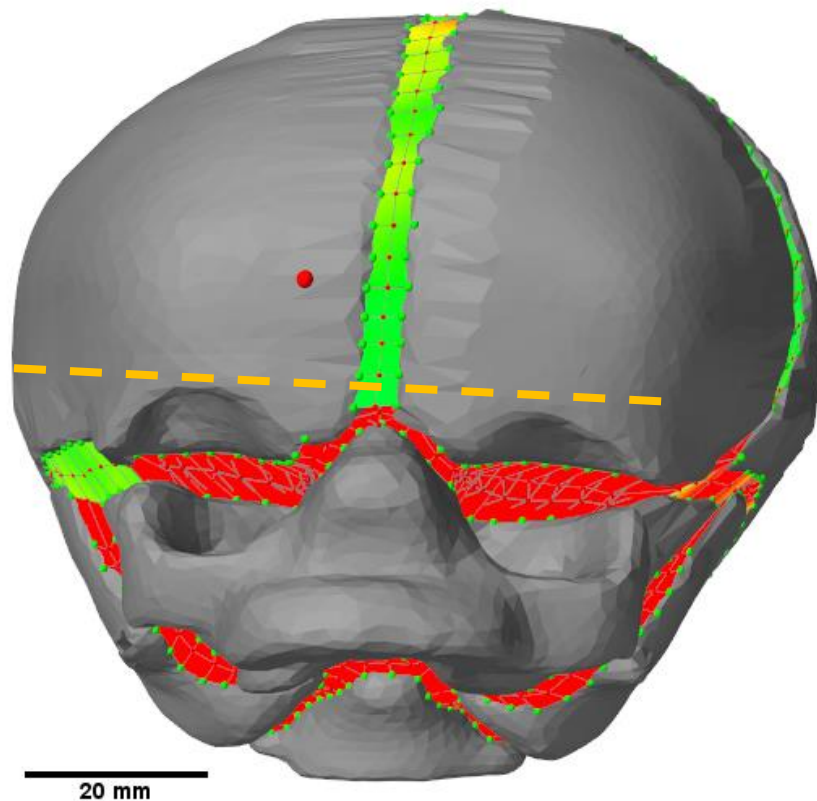


Figure 3.6: Front view of the result from plagiocephaly simulation.

The skull scales of this simulation are indicated in Figure 3.7. All the scales of this plagiocephaly skull increased linearly during the simulation, where the skull width grew the fastest while the skull length rose the slowest. The skull in lateral direction was not restricted, and grew faster than longitudinal direction so as to compensate increasing volume, making the cranial index (in Figure 3.8) goes up quickly. The growth ratio of cranial index was fast at the first 2 seconds but started to slow down a little bit after.

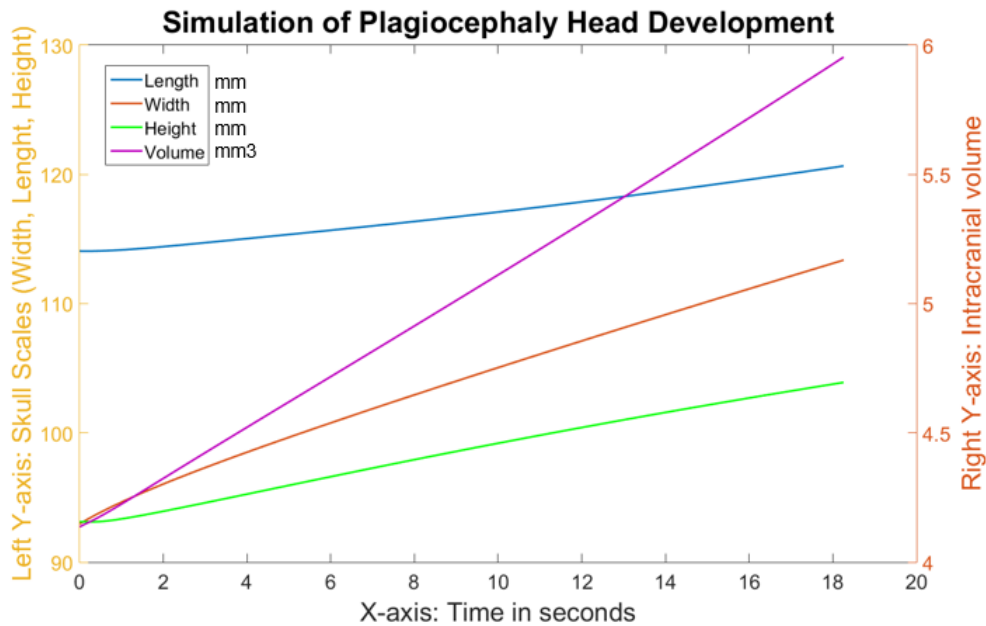


Figure 3.7: The scales of the skull during the simulation of plagiocephaly head development.

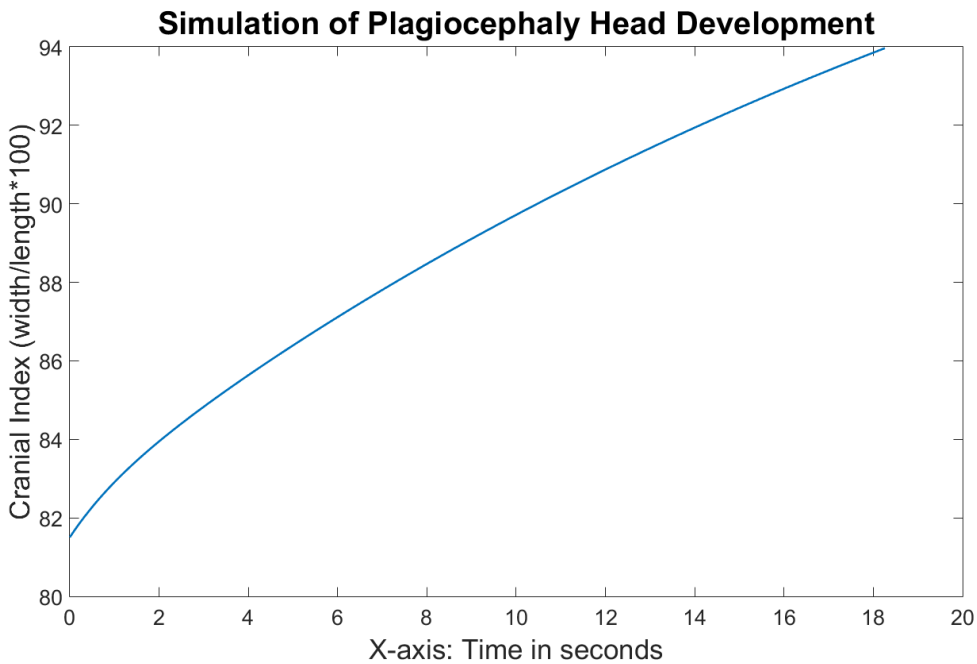


Figure 3.8: Cranial indices during the simulation of anterior plagiocephaly.

3.2.2 Normal Head Development

From Figure 3.9 to 11, we show our model in both initial status and the middle of the normal simulation respectively from three angles of view. Figure 3.9 indicates that the frontal and parietal bones extended in both lateral and longitudinal direction. It is obvious in Figure 3.10 that the growth of cranial face in vertical direction was only from the stretch of the suture across the face, whereas Figure 3.11 shows that the posterior part of skull grew much more vertically at parietal and occipital bones. Generally, since all the sutures are open during the simulation of skull development, the skull tended to become a sphere.

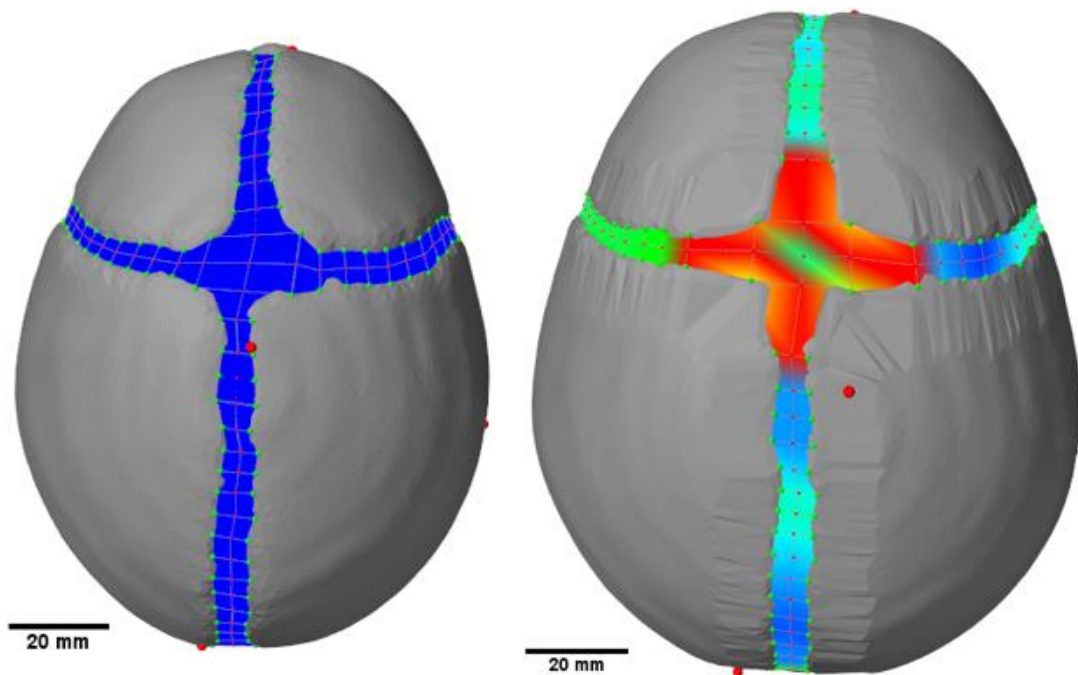


Figure 3.9: Top view of our normal head model, left presented the initial status and right was captured in the middle of the simulation.

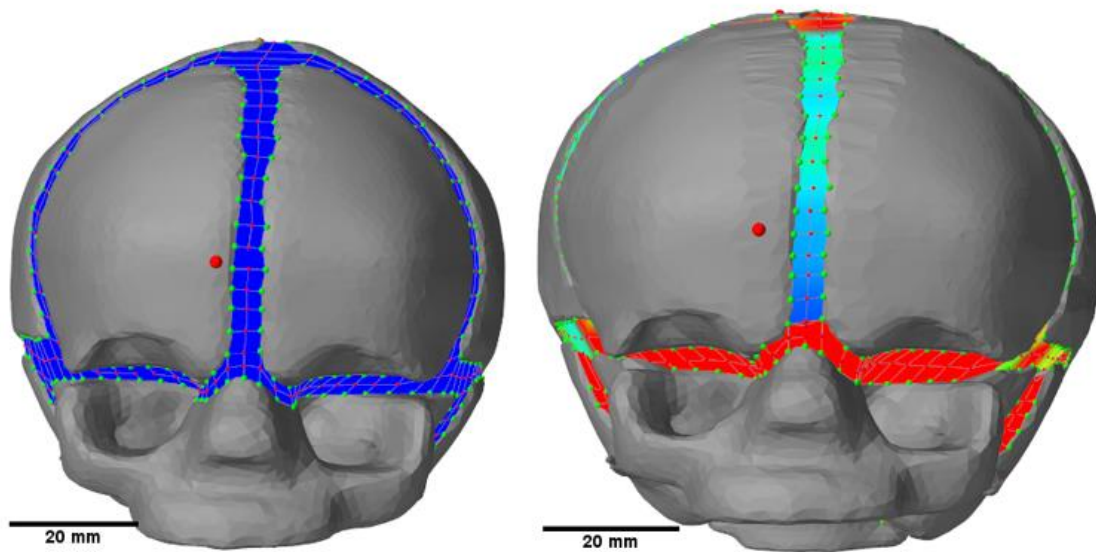


Figure 3.10: Front view of our normal head model, left presented the initial status and right was captured in the middle of the simulation.

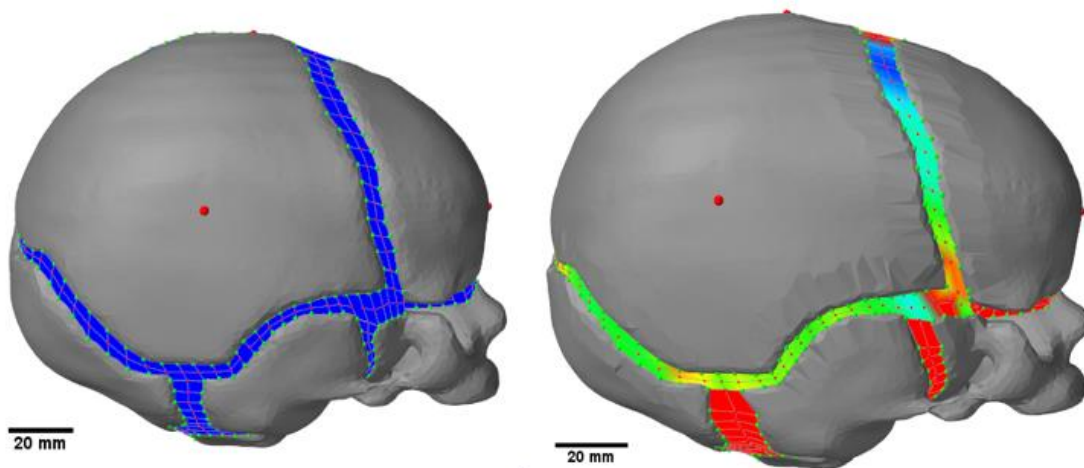


Figure 3.11: Side view of our normal head model, left presented the initial status and right was captured in the middle of the simulation.

Figure 3.12 indicates the skull scales and volumes along time during the normal simulation. We will discuss our simulation time in the angle of human life in the discussion section. The skull length (blue line) and width (yellow line) kept almost the same growth ratio during the simulation while the growth ratio for the skull height (green line) was relative slower. The skull length increased from 114.1 millimeter (mm) to 144.2 mm during 6 seconds, whereas the one in plagiocephaly simulation only grew to 115.7 mm at 6th second. Although in the simulation of plagiocephaly the skull width grew fastest, it was still slower than the development of skull width in the normal one, where the value was 100 mm at 6 seconds in plagiocephaly simulation but reached to 125 mm in normal simulation at the same time. The purple line represents the changes of intracranial volume over time, increasing from 4.1 mm³ to 8.8 mm³ within 7 seconds, whereas in plagiocephaly model, the volume only increases 50% within 20 seconds (under the same force environment). With the same values of all parameters, the volume of normal head increase much faster than plagiocephaly model, indicating that the closed coronal suture prevents the development of the skull inner space.

The blue line in Figure 3.13 represents a non-linear growth of cranial indices during the simulation. The values of cranial index rose quickly during the first second and then slowed down after. The value raised to 86.7 at 6 seconds when the intracranial volume grew to double size, whereas the value in plagiocephaly grew to 87.1 at 6 seconds when its volume enlarged only 14%. Although this record of cranial index indicates an increasing trend as well, the growth ratio was much slower than the plagiocephaly.

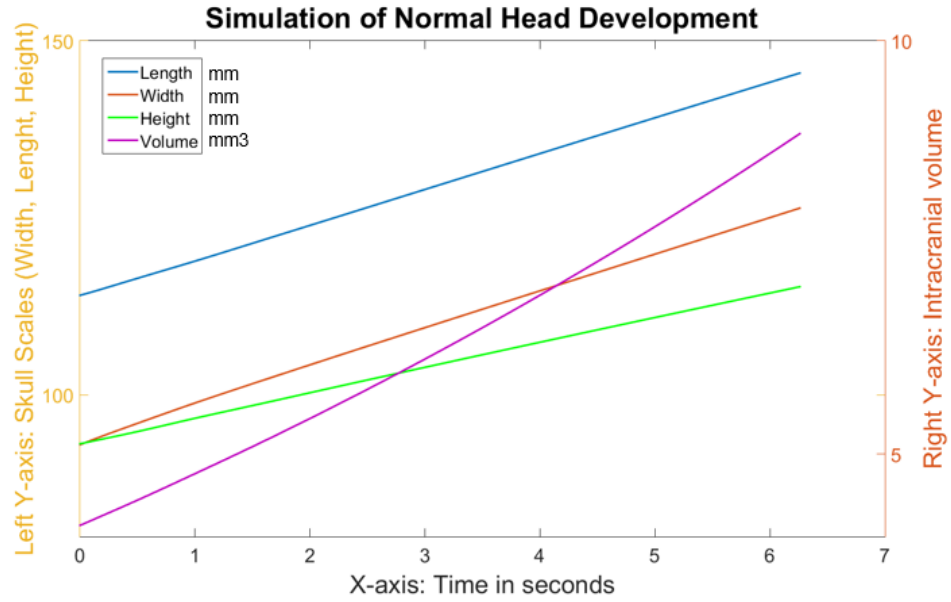


Figure 3.12: The scales of the skull during the simulation of normal head development.

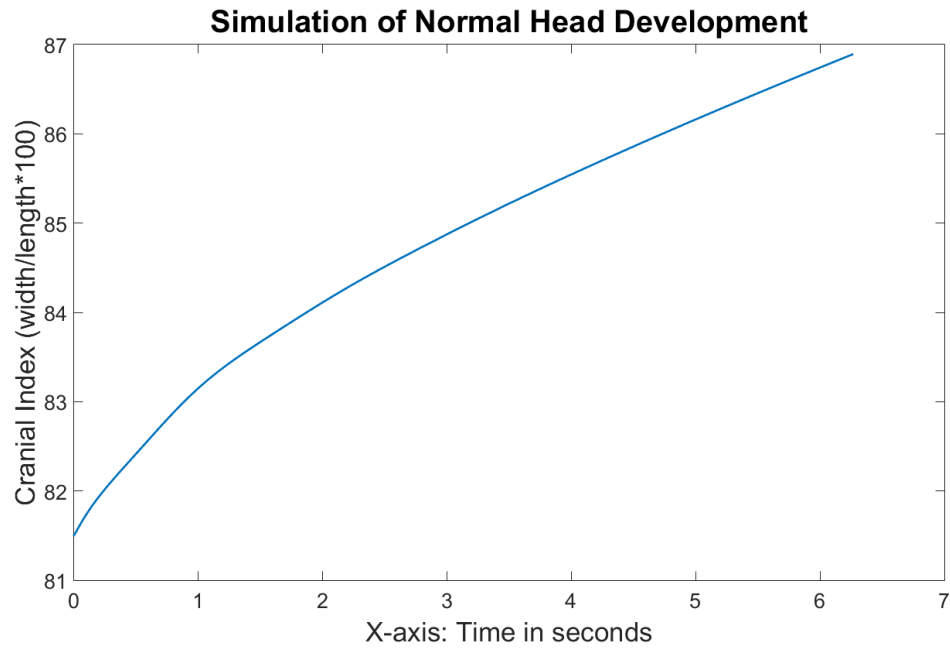


Figure 3.13: Cranial indices with respect to time during the normal head development simulation.

3.2.3 Scaphocephaly

We provide Figure 3.14 to 16 to illustrate our scaphocephaly model at both initial status and the end of the simulation from different angles of view. Since the sagittal suture was closed (Figure 3.14), the skull was prevented to develop in the lateral direction, leading to develop more in the longitudinal direction compare to a developed normal skull (Figure 3.9). In addition, because the cranial base was restricted to develop in lateral direction (Figure 3.15) and the frontal bones were limited to develop vertically by the facial suture, the combined parietal bone was the only plate that was free to develop in both vertical and longitudinal direction, leading to a protrusion at the back (shown in Figure 3.16).

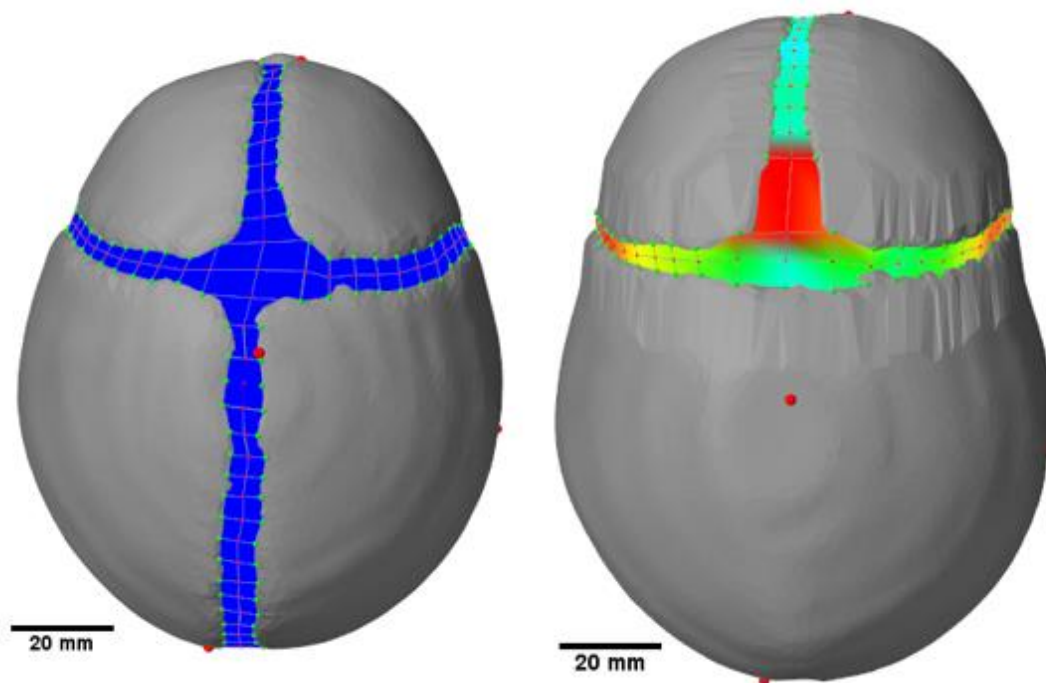


Figure 3.14: Top view of our scaphocephaly head model, left presented the initial status and right was captured in the middle of the simulation.

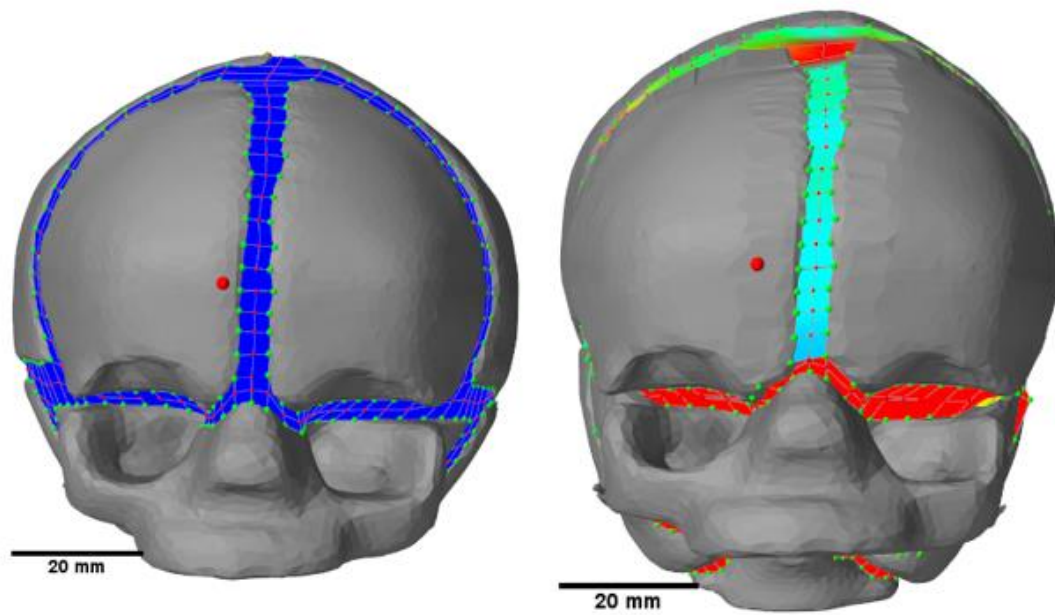


Figure 3.15: Front view of our scaphocephaly head model, left presented the initial status and right was captured in the middle of the simulation.

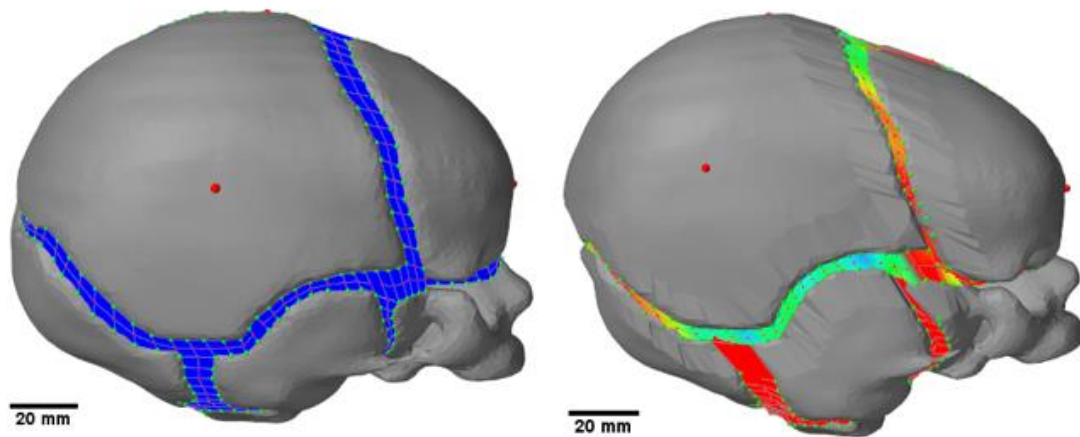


Figure 3.16: Side view of our scaphocephaly head model, left presented the initial status and right was captured in the middle of the simulation.

Figure 3.17 shows the result of this simulation with skull scales and intracranial volumes along time span. The skull width maintained the same during the simulation while the length and height had very close growth ratio. The skull length arrived to 124.7 mm at 6 seconds in this simulation while grew to 144.2 mm in normal, showing a lower growth ratio than the one in normal simulation. The skull height from scaphocephaly model grew slightly slower than the one in normal simulation as well.

The changes of the cranial volume during the scaphocephaly simulation also indicates a linear relationship to the time in Figure 3.18 increased from 4.1 mm^3 to 5.25 mm^3 . The volume increased around 10% from 4.1 mm^3 to 5 mm^3 during 6 seconds, whereas for normal simulation the volume increased to approximately 200% and the plagiocephaly model increased 15% during the first 6 seconds. Therefore, it is obvious that among these three simulations, the growth rate of cranial volume for scaphocephaly model was the lowest.

The cranial index shown in Figure 3.18 also appears a linear relationship with time, gradually decreasing from 81.5 to 72.9. Since the parietal bones were combined, the skull width maintained the same all the time while the skull length kept growing (Figure 3.17) during the simulation, which was consistent with the fact.

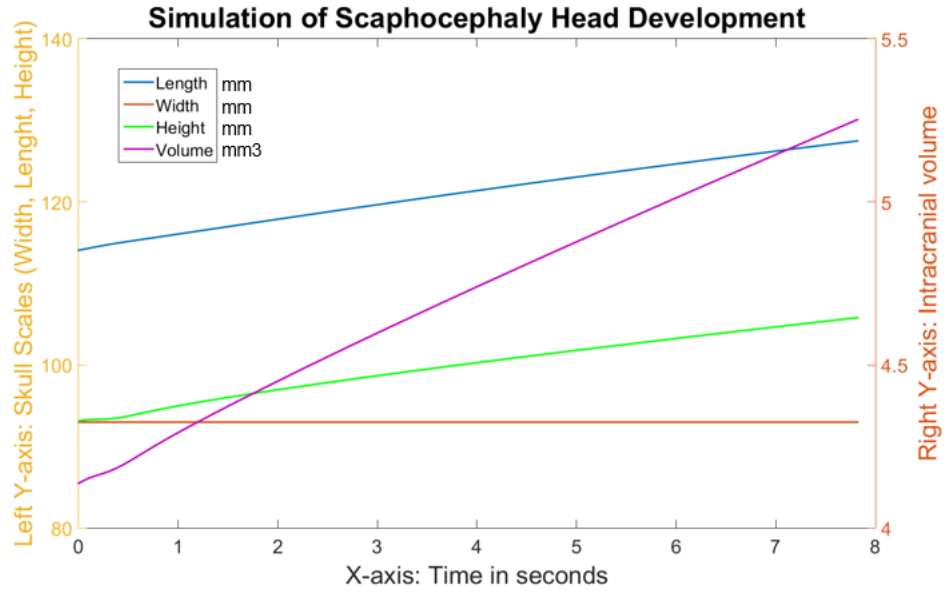


Figure 3.17: The scales of the skull during the simulation of scaphocephaly head development.

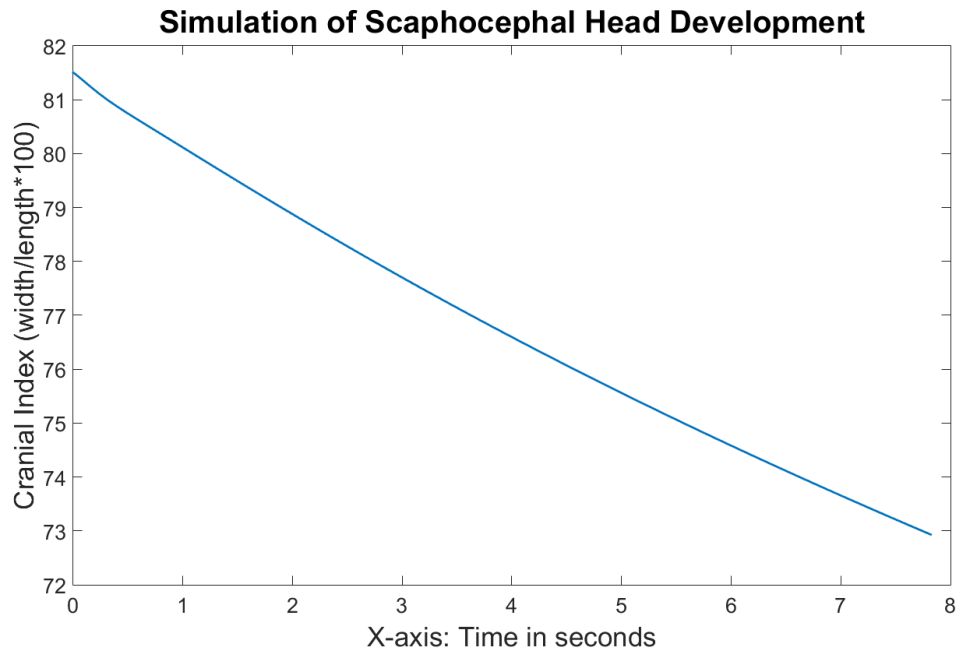


Figure 3.18: Cranial indices with respect to time during the scaphocephaly head development simulation.

3.2.4 Trigenocephaly

We also indicated the difference between the initial trigenocephaly model and the model in the middle of the simulation from three angles of view. From Figure 3.19 we can see that although the skull was inflated in both lateral and longitudinal direction, but the frontal bone was limited in the lateral direction leading to a triangular forehead which fits the fact. Except the frontal bone, all the other skull plates were developed as normal, and appeared like normal from the other two angles of view (shown in Figure 3.20 and 22). Although the parietal bones are the only two plates in the skull that was not restricted, they did not protrude as occurred in scaphocephaly simulation.

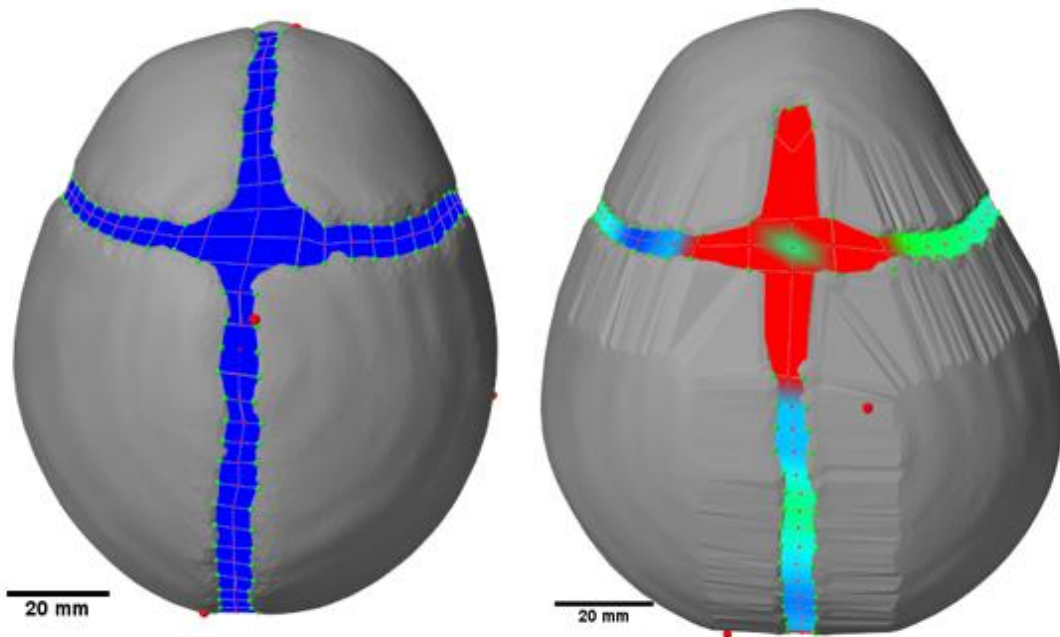


Figure 3.19: Top view of our trigenocephaly head model, left presented the initial status and right was captured in the middle of the simulation.

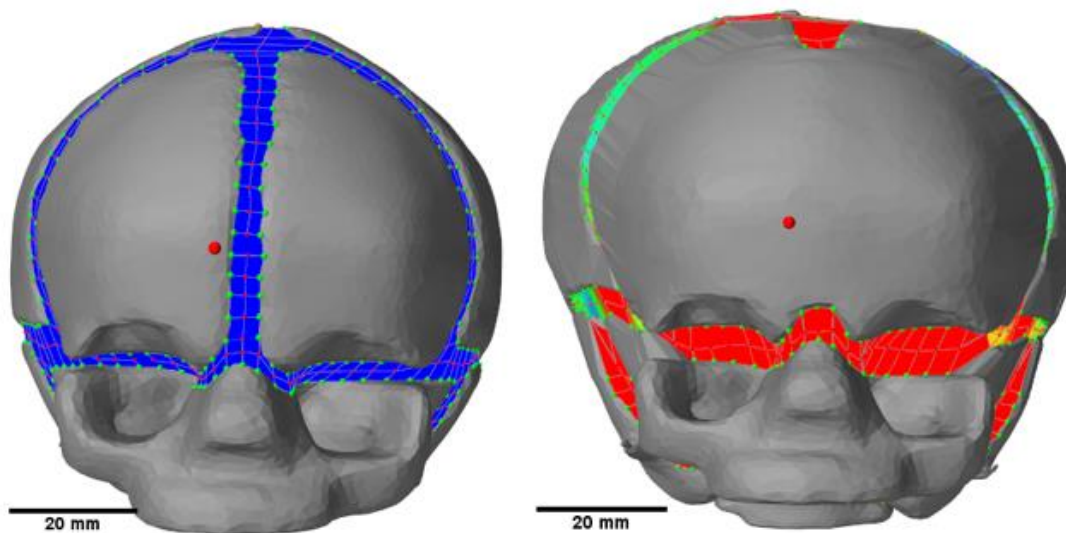


Figure 3.20: Front view of our trigonocephaly head model, left presented the initial status and right was captured in the middle of the simulation.

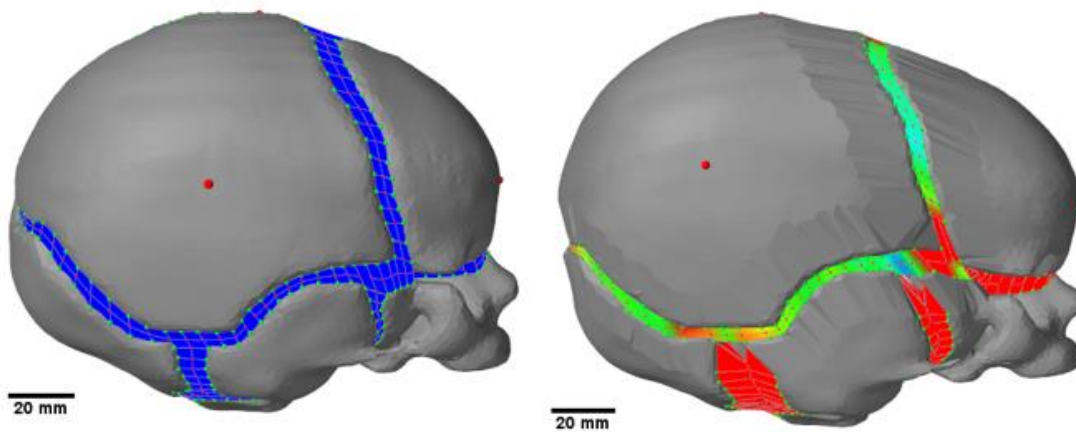


Figure 3.21: Side view of our trigonocephaly head model, left presented the initial status and right was captured in the middle of the simulation.

The skull scales along time span from this trigonocephaly simulation are shown in Figure 3.22. The whole pattern looks similar to the pattern of normal simulation, where the growth ratio of height was lower than the one of width and length. The only difference was that the skull width grew slightly slower than the one in the normal simulation, where the value rose to 121 mm in trigonocephaly simulation while it achieved to 125 mm in the normal simulation.

In Figure 3.23, we display the cranial index values with respect to time. The growth rate of cranial index was steady in trigonocephaly simulation, unlike the rate in normal simulation slowed down over time. In addition, the change of cranial index was slower in this simulation compared to the normal one, where the value was up to 84.3 at 6 second in trigonocephaly case while it increased to 86.7 at 6 second in normal case.

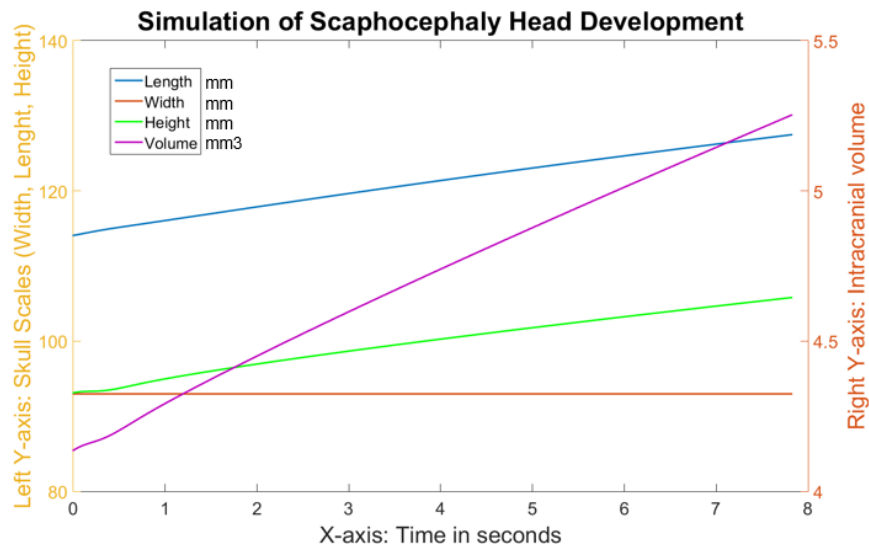


Figure 3.22: The scales of the skull during the simulation of scaphocephaly head development.

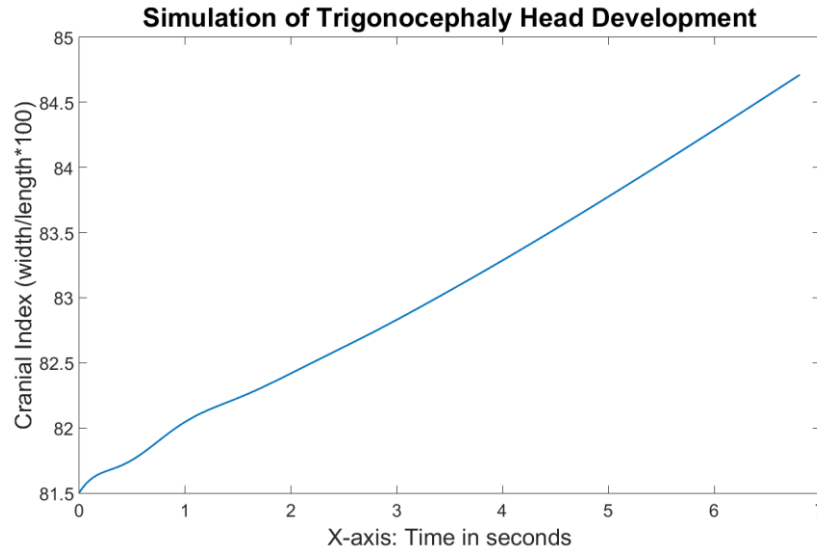


Figure 3.23: Cranial indices with respect to time during the trigonocephaly head development simulation.

3.3 Discussions

In order to evaluate our simulation system, it is necessary to find corresponding clinical data to compare with. However, since CT scans bring risk of radiation exposure to the patient, it is not easy to find a comprehensive and balanced set of scans on which to base a study of abnormal growth. Furthermore, it is practically impossible to find CT scans that would represent normal infant skull growth. For craniosynostosis patients, CT scans of the head is only considered if the deformity is severe enough to need surgical treatment. Consequently, studies can only use traditional methods, which are skull scales (skull width, length and height) and cranial index, to quantitatively measure normal skull development from different infant with different ages; some 3D pictures have also been done but are harder to use to calculate intracranial volumes or changes with time.

The data that demonstrates in Figure 3.24 was from a recent paper (Likus et al. 2014) that collected cranial indices from different healthy babies between new born to 12-month-old. The blue bars in Figure 3.24 indicate the average cranial index value with respect to different periods, which are 80.19 ± 7.49 in 1-3 months, 81.45 ± 7.98 in 4-6 months, and 83.15 ± 7.98 in 7-12 months. The “+” sign in the Figure represented the maximum cases in the corresponding periods, whereas the “*” sign show the minimum cases. The statistics demonstrate a gradually increment of cranial index during the first human life, growing from 80.2 to 83.15 on average. However, it is not guaranteed that all the normal skulls follow this growing trend. As a matter of fact, (Dekaban 1977) did similar statistics about skull shapes including first human life, but they obtained a decrease trend. Therefore, the growing trend of cranial index is variant, resulting from diversified closing time of each sutures. In this section, we will qualitatively compare our result to the trend shown in Figure 3.24.

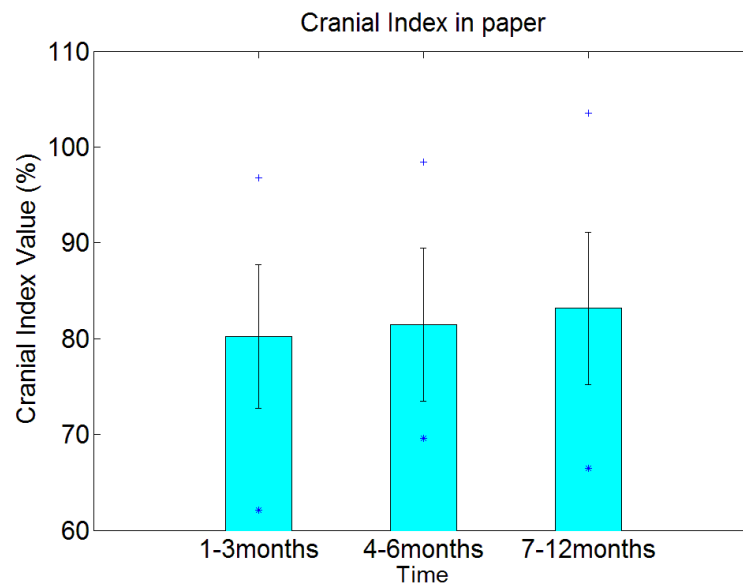


Figure 3.24: Cranial index statistics from (Likus et al. 2014)

We first transfer the time of our normal simulation from second to the real human life, and we assumed that the initial status of our normal head model is a newborn. Figure 2.11 in chapter 2 indicates the growth of head circumference (we approximated it as skull circumference) during the first year, which on average is from 36 to 46 (increased 27%). Since the development of circumference is approximately linear to the growth of skull length and width, and therefore, we supposed that an increment of 27% of the skull length in our normal simulation (shown in Figure 3.12) from the beginning represents the first year of human life, which in our simulation consumed 6.1 seconds. The corresponding cranial index during this 6.1 seconds developed from 81.5 to 86.8 (in Figure 3.13). As a result, the cranial index during the first human life increased 6.5% in our normal simulation, whereas in (Likus et al. 2014)'s paper it grew 3.7%. It demonstrated that as a general result, the growth rate of the cranial index in our simulation was higher than expected. Since the cranial index is the relation between skull width and length, the problem could be targeted to the skull development in either lateral direction or longitudinal direction.

We believed that one of the major problems is the rigidity of our skull model. Since our skull models were generated using a surface mesh, the shape of our skull plates cannot be deformed at all under any conditions. Although the bone is known as a very hard tissue compared to brain, it has the ability to deform during infancy (Baumer et al. 2009; Couper and Albermani 2005). From another point of view, the smoothness of the skull shape is maintained as ellipsoid-like while the intracranial volume was quickly increasing in the first year of human life, which illustrates that the curvatures of the skull plates must be remodeled within this period.

We can imagine that if consider the skull plates and sutures as a whole that can be deformable, the curvatures of the skull plates would be adjusted during the growth of intracranial volume (brain expansion). The dashed yellow line in Figure 3.25 and 26 can be considered as a demonstration of how the skull shape would be adjusted during growth. From top view, both parietal bones should be slightly flattered than previous shapes so as to increase the parietal bones in longitudinal direction and shrink back in lateral direction. From the side view, we can see that instead of shifted to the left, the occipital bone should be tilted downward, and the corner of both frontal bones should be remodeled upward.

Another problem that we did not consider in our normal simulation is the closing time of the sutures. We have mentioned in the introduction chapter that different sutures close at different time. For example, normally the frontal suture close around 2 months. From the simulation of trigonocephaly, we can see that the closure of frontal suture slows down the growth rate of cranial index. Of course, the closure time of each suture is diverse depends on individuals, which leads to various skull shapes in the world.

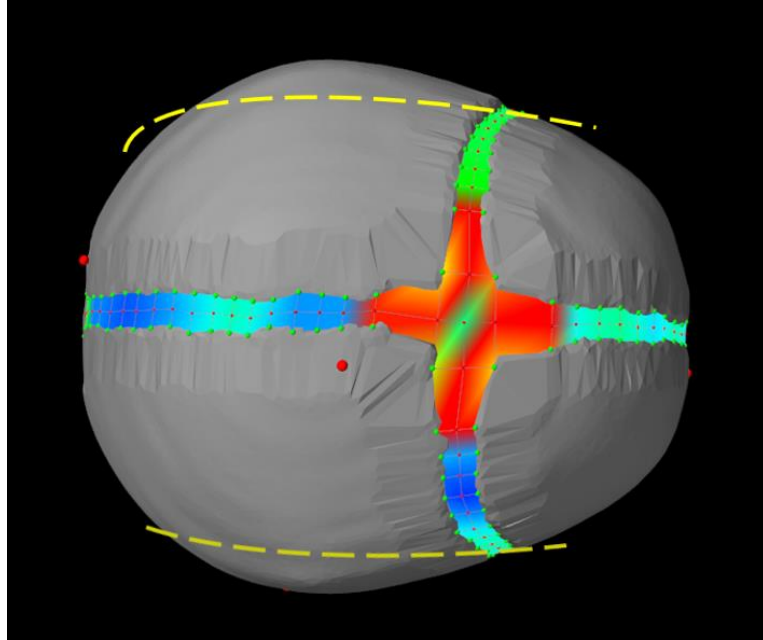


Figure 3.25: Top view of normal head model during the simulation with deformable skull plates.

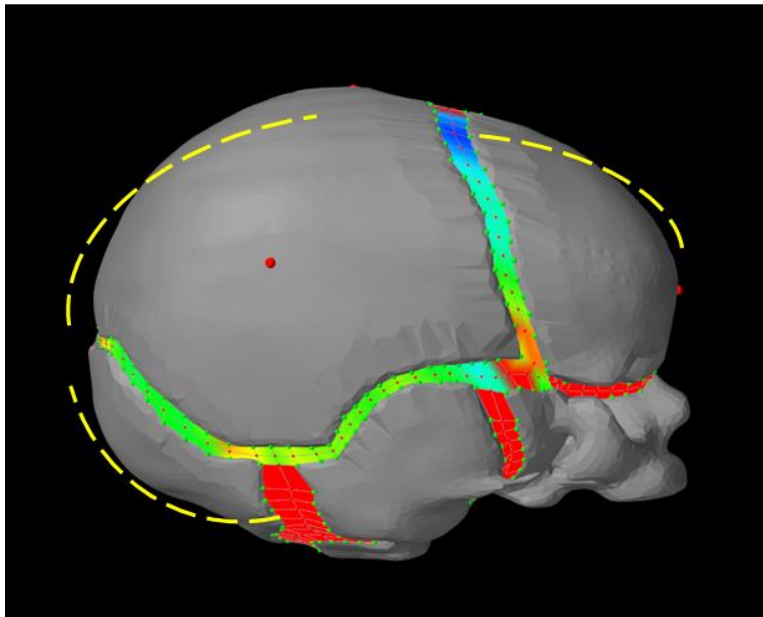


Figure 3.26: Side view of normal head model during the simulation with deformable skull plates.

3.4 Conclusions and Future work

In summary, we used two algorithms to simulate the head development, one with brain model and the other used force on the skull as substitution. We obtained numerically stable results with the second system. Using a brain model to represent the distribution of inner forces should be closer to reality, the calculations of collision detection between the brain and skull resulted in a numerically complex and unstable system. With the force based algorithm, the time for calculating one simulation was shortened from at least one week to only a few seconds. The forces exerted on the skull were fixed once decided, which may be acceptable for the simulation of normal head model development since all the sutures maintained open. However, for the scaphocephaly model with fused parietal bone, the brain was largely constrained in the lateral direction leading to a boost of intracranial pressure, which deviates from the constant forces in our simulating algorithm. As a result, the cranial index of our scaphocephaly simulation should decrease faster than current result. In the future, we could gradually increase the magnitude of the forces while simulating craniosynostosis cases.

The major problem that caused deviation of our result from a general clinical data was the non- deformation for our skull models. We therefore proposed, early in this doctoral project, to utilize deformable model to develop skull. However; in general, mechanical and materials property simulators, such as Artisynt, do not support the instantiation of a deformable mode (skull) to another finite element model (suture). In another point of view, if we modelled the skull and sutures as a whole, it is also impossible to define two types of material properties in one model with Artisynt. Fortunately, we found another

similar simulation platform, which is called SOFA, enables to specify various material properties on different part of a finite element model. With this function, we are able to generate an integrated skull model (includes suture), and characterize skull and sutures respectively on different locations with different mechanical properties. With this feature, we expect to make our simulation closer to the reality. In addition, we could also simulate the skull extension by subdividing the elements at the edge of sutures, which size can be enlarged so as to expand the skull plates.

Chapter 4

4 Evaluation Tool for Craniosynostosis Surgery

4.1 Overview

As we discussed before, the regular treatment for craniosynostosis patients is surgery in order to correct the skull shape. For patients with different ages, the brain growth rates and skull growth rates are variant. As a result, it is hard to predict how a skull shape would develop within a few years after the surgery. Normally, patients should re-visit clinics one year after surgery in order to check subsequent skull growth and to assess the surgery. The common way to evaluate the skull correction is to take CT scans of patient's head right after surgery and one year later so as to compare. However, with the CT scans, the cranial facial teams are only able to qualitatively compare the two. It is still hard to quantitatively evaluate how better a skull shape tends to be normalized or how much worse it tends to return to pathological shape.

Therefore, we hope to develop an algorithm to quantitatively measure the level of deformity of a skull shape that deviates from normal shape. With high level of deformity, we expect to attain higher value from this algorithm. As we know, each type of skulls has similar shapes. Then with three skull models for one patient (pre-operative, post-operative, and one-year after surgery), we can evaluate the surgery by comparing the deformity of these skulls to normal shapes. If the values are decreasing over time and the final value is close to normal index, then we can say the surgery is very sufficient.

Previously, we have explained the algorithm to simulate skull growth (normally, abnormally or postoperatively). With a new born skull or a post-operative skull as input, the output after the simulation is a scaled and deformed skull. With this skull shape evaluation tool, the cranial facial teams can get more intuitional evaluation of a postoperative skull shape, making it easier to choose the optimum surgical plan.

We designed to use statistical modelling to characterize different types of skull shapes with respect to curvature values. Curvature is an intrinsic property of geometries to describe how local shape develops along different direction (Nigam and Agrawal 2013). It plays an important role in mesh simplification (Hua, Huang, and Li 2015), surface smoothing (Desbrun et al. 1999), segmentation (Zhang et al. 2008), and shape analysis (Kawata et al. 1999; Florindo, Backes, and Bruno 2010). Inspired from these work, we decided to utilize curvature values to evaluate the skull shapes.

In this chapter, we will first introduce curvature calculation for a smooth surface in differential geometry, following by several popular methods to estimate curvature for discretized surface. Subsequently, we will elaborate a simple and fast algorithm developed by (Dong and Wang 2005), which we adopted in our statistical model. Finally, we will explain the procedures of how we scheme our statistical model and how we train our data in order to classify different types of shapes.

4.2 Curvatures in Differential Geometry

Before the development of calculus, geometry was interpreted as some simple curves, such as circles, ellipse, lines, parabolas, hyperbolas and so on (Gray et al.). The theory of

curves and surfaces has not developed until the proposition of Cartesian coordinates by Descartes in 1600s (Gray et al.). The concept of surface curvature was introduced subsequently by do Carmo in 1976 (do Carmo). It is interpreted as an intrinsic property of differentiable surfaces that summarizes the spanning trend of a location on the surface to all directions. It plays an important role in shape analysis applied in various research fields. In this section, we will dip into differential geometry to explain the concept of curvature for differentiable manifolds.

4.2.1 Curves and Surfaces

Consider an open set denoted as $D \subset \mathbf{R}^2$. A regular surface $S \subset \mathbf{R}^3$ is defined as such a subset that can be represented by a smooth vector function $\mathbf{r}: D \rightarrow \mathbf{R}^3$ with two variables, which is an injective (one to one) map:

$$\mathbf{r} = \mathbf{r}(u, v) = \begin{pmatrix} x(u, v) \\ y(u, v) \\ z(u, v) \end{pmatrix} \quad \text{Equation 4.1}$$

Where $(u, v) \in D$ denote coordinates of all points P in \mathbf{R}^2 , and $\mathbf{r}(x, y, z)$ indicate vectors pointing from origin to according points in \mathbf{R}^3 .

Let $I \subset \mathbf{R}$ denote a subset. We can define a plane curve or line $(u, v) \in D$ where $u, v: I \rightarrow \mathbf{R}^2$ are two smooth functions expressed as $u(t)$ and $v(t)$ respectively. A space curve on the regular surface $S \subset \mathbf{R}^3$ is then defined by the composite function $\mathbf{x}: I \rightarrow \mathbf{R}^3$, expressed by the following formula:

$$\mathbf{x}(t) = \mathbf{r}(u(t), v(t)), \mathbf{x}(t) \in S \quad \text{Equation 4.2}$$

From another perspective to understand, a curve on the regular surface $S \subset \mathbf{R}^3$ is a trajectory of a point that moving on the surface through time. Given a specific location $\mathbf{r}(u_0, v_0)$ (a point P) on this curve, the derivative with respect to t at this location $\mathbf{r}_t(u_0, v_0)$ is tangent vector of this curve at point P, and is one of tangent vectors of the surface at point P. More generally, at location P, there are infinite curves with infinite tangent vectors. These tangent vectors form a plane called tangent plane of the surface at location P. Since the vector function for the surface S has two variables, we can express any tangent vector of the surface at P (u_0, v_0) by the differential of the function:

$$d\mathbf{r}(u_0, v_0) = \mathbf{r}_u(u_0, v_0)du + \mathbf{r}_v(u_0, v_0)dv \quad \text{Equation 4.3}$$

It is obvious that the two partial derivatives $\mathbf{r}_u(u, v)$ and $\mathbf{r}_v(u, v)$ can be considered as two tangent vectors at location (u, v) on the surface. Since these two derivatives are linear independent ($\mathbf{r}_u \cdot \mathbf{r}_v \neq 0$), we can safely specify this tangent plane of the surface at P by unit normal vector:

$$\mathbf{n} = \frac{\mathbf{r}_u(u_0, v_0) \times \mathbf{r}_v(u_0, v_0)}{|\mathbf{r}_u(u_0, v_0) \times \mathbf{r}_v(u_0, v_0)|} \quad \text{Equation 4.4}$$

With these essential concepts, we will introduce the first and second fundamental forms (from geometric meaning) in the next two sections as the preparation for curvature calculation. A surface should be differential enough to support at least the two forms in order to attain curvatures.

4.2.2 The First Fundamental Form

Consider another point P' on the curve C located in the neighborhood of P . Let the two vectors $\mathbf{r}(u, v)$ and $\mathbf{r}(u + \Delta u, v + \Delta v)$ denote \overrightarrow{OP} and $\overrightarrow{OP'}$ respectively. The vector $\overrightarrow{PP'}$ therefore can be estimated according to Taylor's theorem:

$$\overrightarrow{PP'} = \Delta \mathbf{r} = \mathbf{r}(u + \Delta u, v + \Delta v) - \mathbf{r}(u, v) = \mathbf{r}_u \Delta u + \mathbf{r}_v \Delta v + \dots$$

Where the omit part are small enough to be ignored. Therefore, we can obtain such differential relation:

$$d\mathbf{r} = \mathbf{r}_u du + \mathbf{r}_v dv \quad \text{Equation 4.5}$$

When P' is infinitely close to P ($\Delta u \rightarrow 0, \Delta v \rightarrow 0$). The arc length ds on the surface S from P to P' then can be approximated by the distance between P and P' and represented as follow:

$$\begin{aligned} ds^2 &= \|d\mathbf{r}\|^2 = d\mathbf{r} \cdot d\mathbf{r} \\ &= (\mathbf{r}_u du + \mathbf{r}_v dv) \cdot (\mathbf{r}_u du + \mathbf{r}_v dv) = \mathbf{r}_u \cdot \mathbf{r}_u (du)^2 + 2\mathbf{r}_u \cdot \mathbf{r}_v dudv + \mathbf{r}_v \cdot \mathbf{r}_v (dv)^2 \end{aligned} \quad \text{Equation 4.6}$$

Let

$$E = \mathbf{r}_u \cdot \mathbf{r}_u, \quad F = \mathbf{r}_u \cdot \mathbf{r}_v, \quad G = \mathbf{r}_v \cdot \mathbf{r}_v$$

Then the following representation is defined as the first fundamental form:

$$ds^2 = Edu^2 + 2Fdudv + Gdv^2 \quad \text{Equation 4.7}$$

Where E, F and F are known as the coefficients of the form. It is normally written as matrix tensor:

$$\mathbf{I} = \begin{bmatrix} E & F \\ F & G \end{bmatrix} = \begin{bmatrix} \mathbf{r}_u^T \mathbf{r}_u & \mathbf{r}_u^T \mathbf{r}_v \\ \mathbf{r}_u^T \mathbf{r}_v & \mathbf{r}_v^T \mathbf{r}_v \end{bmatrix} \quad \text{Equation 4.8}$$

In the last section, we have discussed that equation 6 indicates a tangent vector of any point on the surface. Let $\{\mathbf{r}_u, \mathbf{r}_v\}$ denote the natural basis vectors of the tangent vector, and (du, dv) are considered as the components of the natural basis vectors to form the tangent vector. From this point of view, the coefficients can be interpreted as the scalar product of the basis vectors. (Gelas et al.) explained the meaning of this fundamental form as an inner product on the tangent plane of location P on the surface.

4.2.3 The Second Fundamental Form

One intuitive way to check the extent a surface bend at a point P, is to see the distance from a closed point P' to the tangent plane of P. The distance denoted as δ can be calculated with Taylor series:

$$\begin{aligned} \delta &= \overline{PP'} \cdot \mathbf{n} = \mathbf{r}(u + \Delta u, v + \Delta v) \cdot \mathbf{n} - \mathbf{r}(u, v) \cdot \mathbf{n} \\ &= \frac{1}{2} (\mathbf{r}_{uu} \cdot \mathbf{n} (\Delta u)^2 + 2\mathbf{r}_{uv} \cdot \mathbf{n} \Delta u \Delta v + \mathbf{r}_{vv} \cdot \mathbf{n} (\Delta v)^2) + \dots \end{aligned}$$

Where the omit part is small enough to be ignored.

Let

$$L = \mathbf{r}_{uu} \cdot \mathbf{n}, \quad M = \mathbf{r}_{uv} \cdot \mathbf{n}, \quad N = \mathbf{r}_{vv} \cdot \mathbf{n}$$

Denote as the coefficients of the second fundamental form. Since $\mathbf{r}_u \cdot \mathbf{n} = \mathbf{r}_v \cdot \mathbf{n} = 0$, the coefficients can be represented as follow alternatively:

$$L = -\mathbf{r}_u \cdot \mathbf{n}_u, \quad M = -\mathbf{r}_u \cdot \mathbf{n}_v, \quad N = -\mathbf{r}_v \cdot \mathbf{n}_v$$

Then

$$2\delta = -d\mathbf{r} \cdot d\mathbf{n} = Ldu^2 + 2Mdudv + Ndv^2 \quad \text{Equation 4.9}$$

is defined as the second fundamental form when the distance is infinitely small. Its matrix form is expressed as follow:

$$\mathbf{II} = \begin{bmatrix} L & M \\ M & N \end{bmatrix} = \begin{bmatrix} \mathbf{r}_{uu}^T \mathbf{n} & \mathbf{r}_{uv}^T \mathbf{n} \\ \mathbf{r}_{uv}^T \mathbf{n} & \mathbf{r}_{vv}^T \mathbf{n} \end{bmatrix} \quad \text{Equation 4.10}$$

If δ is a positive number, it means P' is above the T_p , where the normal vector \mathbf{n} stays. If δ is negative, then it is on the other side.

4.2.4 Normal curvature

Let's denote the arc length of a curve on the surface S. Then we can interpret the variables of vector function \mathbf{r} as functions of arc length: $u=u(s)$, $v=v(s)$. This curve can be expressed by the vector function $\mathbf{r}=\mathbf{r}(u(s), v(s))$. The unit tangent vector ($d\mathbf{r}$) of the curve on the surface with respect to the arc length (s) is indicated as:

$$\mathbf{a} = \frac{d\mathbf{r}}{ds} = \mathbf{r}_u \cdot \frac{du}{ds} + \mathbf{r}_v \cdot \frac{dv}{ds} \quad \text{Equation 4.11}$$

The curvature vector of the curve then is defined as the derivative of its unit tangent vector:

$$\begin{aligned} \dot{\mathbf{a}} &= \kappa \boldsymbol{\beta} \\ &= \mathbf{r}_{uu} \left(\frac{du}{ds} \right)^2 + 2\mathbf{r}_{uv} \frac{du}{ds} \frac{dv}{ds} + \mathbf{r}_{vv} \left(\frac{dv}{ds} \right)^2 \\ &\quad + \mathbf{r}_u \frac{d^2u}{ds^2} + \mathbf{r}_v \frac{d^2v}{ds^2} \end{aligned} \quad \text{Equation 4.12}$$

Where $\boldsymbol{\beta}$ denotes the unit vector of the curvature, and κ is the scale of this vector. We can project curvature vector onto the unit normal vector, using the following formula:

$$\begin{aligned} \kappa_n &= \dot{\mathbf{a}} \cdot \mathbf{n} = \kappa (\boldsymbol{\beta} \cdot \mathbf{n}) = \mathbf{r}_{uu} \cdot \mathbf{n} \left(\frac{du}{ds} \right)^2 + 2\mathbf{r}_{uv} \cdot \mathbf{n} \frac{du}{ds} \frac{dv}{ds} + \mathbf{r}_{vv} \cdot \mathbf{n} \left(\frac{dv}{ds} \right)^2 \\ &= \frac{Ldu^2 + 2Mdudv + Ndv^2}{(ds)^2} \end{aligned} \quad \text{Equation 4.13}$$

We can see that, the direction of the normal curvature only depends on the direction of its tangent vector $\left(\frac{du}{ds}, \frac{dv}{ds} \right)$, and is therefore we define it as the normal curvature with respect to the unit tangent vector at location (u, v) on the surface. Observing this expression carefully, we discover that numerator part of this expression is the second fundamental form, and the denominator part can be approximately equal to the first

fundamental form when the arc length is infinitely small. In consequence, we can redefine the normal curvature by the two forms:

$$\kappa_n = \frac{\mathbf{II}}{\mathbf{I}} = \frac{Ldu^2 + 2Mdudv + Ndv^2}{Edu^2 + 2Fdudv + Gdv^2} \quad \text{Equation 4.14}$$

Alternatively, we can express normal curvature in the following form:

$$\kappa_n = \frac{L + 2M\eta + N\eta^2}{E + 2F\eta + G\eta^2}, \eta = \frac{dv}{du} \quad \text{Equation 4.15}$$

Which will be useful to deduce the Principal curvatures in the next section.

4.2.5 Principal curvatures

The calculation of principal curvatures is followed by a differential geometry book (Struik). According to equation 4.15, we can acquire the extreme values of the normal

curvature by making $\frac{d\kappa_n}{d\eta} = 0$. This equation can be expanded:

$$(E + 2F\eta + G\eta^2)(N\eta + M) - (L + 2M\eta + N\eta^2)(G\eta + F) = 0$$

From which we can deduce such relation:

$$\kappa_n = \frac{L + 2M\eta + N\eta^2}{E + 2F\eta + G\eta^2} = \frac{M + N\eta}{F + G\eta} \quad \text{Equation 4.16}$$

Since $L + 2M\eta + N\eta^2 = (L + M\eta) + \eta(M + N\eta)$ and

$E + 2F\eta + G\eta^2 = (E + F\eta) + \eta(F + G\eta)$, the expression can be simplified to:

$$(E + F\eta)(M + N\eta) = (L + M\eta)(F + G\eta) \quad \text{Equation 4.17}$$

As a result, it is obvious that the expression of normal curvature can be extended:

$$\kappa_n = \frac{L + 2M\eta + N\eta^2}{E + 2F\eta + G\eta^2} = \frac{M + N\eta}{F + G\eta} = \frac{L + N\eta}{E + F\eta} \quad \text{Equation 4.18}$$

Substitute $\eta = \frac{dv}{du}$ into $\kappa_n = \frac{M + N\eta}{F + G\eta}$ and $\kappa_n = \frac{L + N\eta}{E + F\eta}$ respectively, we obtain:

$$(L - \kappa_n E)du + (M - \kappa_n F)dv = 0$$

$$(M - \kappa_n F)du + (N - \kappa_n G)dv = 0$$

Interpreted these two equations in linear algebra, we can form a homogeneous system

$AX = 0$, where

$$A = \begin{bmatrix} L - \kappa_n E & M - \kappa_n F \\ M - \kappa_n F & N - \kappa_n G \end{bmatrix}, x = \begin{bmatrix} du \\ dv \end{bmatrix}$$

In order to ensure $\eta = \frac{dv}{du}$ exists, this system must have a nontrivial solution, which

means the determinant of the matrix A should equal to zero ($\det(A) = 0$):

$$(EG - F^2)\kappa_n^2 - (EN + GL - 2FM)\kappa_n + (LN - M^2) = 0 \quad \text{Equation 4.19}$$

Let suppose this quadratic equation has two real roots denoted as κ_1 and κ_2 , we can

obtain:

$$K = \kappa_1 \kappa_2 = \frac{c}{a} = \frac{LN - M^2}{EG - F^2} \quad \text{Equation 4.20}$$

$$H = \frac{1}{2}(\kappa_1 + \kappa_2) = \frac{b}{2a} = \frac{EN + GL - 2FM}{2(EG - F^2)} \quad \text{Equation 4.21}$$

Hence, we can simplify equation 21 to:

$$\kappa_n^2 - 2H\kappa_n + K = 0$$

The two real roots can be represented in terms of K and H:

$$\kappa_1 = \kappa_{\max} = H + \sqrt{H^2 - K}$$

$$\kappa_2 = \kappa_{\min} = H - \sqrt{H^2 - K} \quad \text{Equation 4.22}$$

The κ_1 and κ_2 are the maximum and minimum curvatures respectively at location (u, v) on the surface. $K = \kappa_1 \kappa_2$ is defined as Gaussian curvature and $H = \frac{1}{2}(\kappa_1 + \kappa_2)$ is named as Mean curvature of the surface at location (u, v). In the case where $\kappa_1 = \kappa_2 = H$, this local area is a part of spherical surface.

According equation 4.18, we can develop a quadratic equation of η :

$$(FN - GM)\eta^2 + (EN - GL)\eta + (EM - FL) = 0$$

Let η_{\max} and η_{\min} denote the direction of κ_{\max} and κ_{\min} respectively, we have:

$$\eta_{\max} + \eta_{\min} = -\frac{EN - GL}{FN - GM}$$

$$\eta_{\max}\eta_{\min} = \frac{EM - FL}{FN - GM}$$

According to equation 4.6, we can calculate the angle θ between two tangent vectors of two curves, which $\mathbf{r}_1 = \mathbf{r}(u_1(t), v_1(t))$ and $\mathbf{r}_2 = \mathbf{r}(u_2(t), v_2(t))$:

$$\begin{aligned} \cos \theta &= \frac{\dot{\mathbf{r}}_1 \cdot \dot{\mathbf{r}}_2}{|\dot{\mathbf{r}}_1| |\dot{\mathbf{r}}_2|} \\ &= \frac{Edu_1 du_2 + F(du_1 dv_2 + dv_1 du_2) + Gdv_1 dv_2}{\sqrt{Edu_1^2 + Fdu_1 dv_1 + Gdv_1^2} \sqrt{Edu_2^2 + Fdu_2 dv_2 + Gdv_2^2}} \\ &= E \frac{du_1}{ds_1} \frac{du_2}{ds_2} + F \left(\frac{du_1}{ds_1} \frac{dv_2}{ds_2} + \frac{dv_1}{ds_1} \frac{du_2}{ds_2} \right) + G \frac{dv_1}{ds_1} \frac{dv_2}{ds_2} \end{aligned}$$

If the two tangent vectors are orthogonal, then the above expression should satisfy following condition:

$$\begin{aligned} Edu_1 du_2 + F(du_1 du_2 + dv_1 du_2) + Gdv_1 dv_2 \\ = E + F(\eta_{\max} + \eta_{\min}) + G(\eta_{\max} \eta_{\min}) = 0 \end{aligned}$$

Let expression of η_{\max} and η_{\min} plug into the above equation, we can attain:

$$\begin{aligned} E + F(\eta_{\max} + \eta_{\min}) + G(\eta_{\max} \eta_{\min}) \\ = \frac{1}{EN - GM} [E(FN - GM) - F(EN - GL) + G(EM - FL)] \\ = 0 \end{aligned}$$

It is obvious that this equation is true. Therefore, the directions of the principal curvatures are orthogonal.

4.2.6 Gauss Map and Weingarten Map

From previous sections, we know that, at any location/point (u, v) of a smooth surface S , we can obtain its unit normal vector $\mathbf{n}(u, v)$ to indicate the tangent plane at point (u, v) .

If we transform the unit normal vector so that its starting point is origin of the coordinate, its end point must fall onto the surface of unit sphere denoted as Σ . As a result, we can find such a differentiable map $g : S \rightarrow \Sigma$, which is expressed as:

$$g(\mathbf{r}(u, v)) = \mathbf{n}(u, v) \quad \text{Equation 4.23}$$

This map is called Gauss map. Similarly, we can obtain a tangential map, defined as:

$$g_* \left(\frac{d\mathbf{r}}{dt} \right) = \frac{d\mathbf{n}(u(t), v(t))}{dt} = \mathbf{n}_u \frac{du}{dt} + \mathbf{n}_v \frac{dv}{dt}$$

$$\Rightarrow \begin{cases} g_*(\mathbf{r}_u) = \mathbf{n}_u \\ g_*(\mathbf{r}_v) = \mathbf{n}_v \end{cases} \quad \text{Equation 4.24}$$

Which project the tangent plane from point (u, v) at surface S to the unit sphere Σ . The

\mathbf{n}_u and \mathbf{n}_v can be interpreted as two tangent vectors of the unit sphere Σ at point (u, v) .

Since the tangent plane of the surface at (u, v) is parallel to the according tangent plane on the unit sphere Σ , we can regard \mathbf{n}_u and \mathbf{n}_v at Σ as tangent vectors \mathbf{r}_u and \mathbf{r}_v on the surface S . Weingarten Map is defined as such linear transformation, expressed as:

$$W = -g_* : T_p S \rightarrow T_p S \quad \text{Equation 4.25}$$

Where $T_p S$ is the tangent plane of an arbitrary point $P(u, v)$ on the surface S that is composed of tangent vectors $\mathbf{r}_u, \mathbf{r}_v$. According to the definition of the tangent vector of the surface \mathbf{r} , we can obtain:

$$\begin{aligned} W(d\mathbf{r}) &= W(\mathbf{r}_u du + \mathbf{r}_v dv) = -g_*(\mathbf{r}_u)du - g_*(\mathbf{r}_v)dv \\ &= g(\mathbf{n}_u du + \mathbf{n}_v dv) = -d\mathbf{n} \end{aligned} \quad \text{Equation 4.26}$$

And
$$\mathbf{\Pi} = -d\mathbf{n} \cdot d\mathbf{r} = W(d\mathbf{r}) \cdot d\mathbf{r} \quad \text{Equation 4.27}$$

If a non-zero tangent vector $d\mathbf{r}$ and a real number λ exist to make:

$$W(d\mathbf{r}) = \lambda d\mathbf{r}$$

We define this λ as an eigenvalue of W , and $d\mathbf{r}$ is a real eigenvector with respect to λ .

Considering the representation of normal curvature, we can acquire:

$$\kappa_n = \frac{-d\mathbf{n} \cdot d\mathbf{r}}{d\mathbf{r} \cdot d\mathbf{r}} = \frac{W(d\mathbf{r}) \cdot d\mathbf{r}}{d\mathbf{r} \cdot d\mathbf{r}} = \lambda \quad \text{Equation 4.28}$$

Which indicates that the normal curvature is precisely an eigenvalue of Weingarten map.

Let κ_1 and κ_2 denote two normal curvatures of the surface at location (u, v) , and $\{\mathbf{e}_1, \mathbf{e}_2\}$ represent the direction along κ_1 and κ_2 that form an orthogonal basis of the tangent plane at location (u, v) . According to 3.23, we can get $W(\mathbf{e}_1) = \kappa_1 \mathbf{e}_1$, $W(\mathbf{e}_2) = \kappa_2 \mathbf{e}_2$. Any unit tangent vector \mathbf{e} on the tangent plane can be indicated with the basis: $\mathbf{e} = \cos \theta \mathbf{e}_1 + \sin \theta \mathbf{e}_2$

where θ is the angle between \mathbf{e} and \mathbf{e}_1 . Therefore, we use two orthogonal normal curvatures to calculate any normal curvature on the same tangent plane:

$$W(\mathbf{e}) = \kappa_1 \cos \theta \mathbf{e}_1 + \kappa_2 \sin \theta \mathbf{e}_2$$

$$\Rightarrow \kappa_n(\theta) = \frac{W(\mathbf{e}) \cdot \mathbf{e}}{\mathbf{e} \cdot \mathbf{e}}$$

$$= (\kappa_1 \cos \theta \mathbf{e}_1 + \kappa_2 \sin \theta \mathbf{e}_2) \cdot (\cos \theta \mathbf{e}_1 + \sin \theta \mathbf{e}_2)$$

$$= \kappa_1 \cos^2 \theta + \kappa_2 \sin^2 \theta$$

Equation 4.29

This expression is defined as Euler's formula. Since the directions of the principal curvatures are orthogonal, we can also interpret κ_1 and κ_2 in 4.22 as principal curvatures.

Let us transform equation 4.24 to matrix, we can deduce such relation:

$$\begin{pmatrix} -\mathbf{n}_u \\ -\mathbf{n}_n \end{pmatrix} = \begin{pmatrix} a_{11} & a_{12} \\ a_{21} & a_{22} \end{pmatrix} \begin{pmatrix} \mathbf{r}_u \\ \mathbf{r}_n \end{pmatrix}$$

$$\Rightarrow \begin{pmatrix} -\mathbf{n}_u \\ -\mathbf{n}_n \end{pmatrix} \cdot (\mathbf{r}_u, \mathbf{r}_n) = \begin{pmatrix} a_{11} & a_{12} \\ a_{21} & a_{22} \end{pmatrix} \begin{pmatrix} \mathbf{r}_u \\ \mathbf{r}_n \end{pmatrix} \cdot (\mathbf{r}_u, \mathbf{r}_n)$$

$$\Rightarrow \begin{pmatrix} L & M \\ M & N \end{pmatrix} = \begin{pmatrix} a_{11} & a_{12} \\ a_{21} & a_{22} \end{pmatrix} \begin{pmatrix} E & F \\ F & G \end{pmatrix}$$

$$\Rightarrow \begin{pmatrix} a_{11} & a_{12} \\ a_{21} & a_{22} \end{pmatrix} = \begin{pmatrix} L & M \\ M & N \end{pmatrix} \cdot \begin{pmatrix} E & F \\ F & G \end{pmatrix}^{-1}$$

$$\begin{aligned}
&= \frac{1}{EG - F^2} \begin{pmatrix} L & M \\ M & N \end{pmatrix} \begin{pmatrix} G & -F \\ -F & E \end{pmatrix} \\
&= \frac{1}{EG - F^2} \begin{pmatrix} LG - MF & -LF + ME \\ MG - NF & -MF + NE \end{pmatrix}
\end{aligned}$$

Therefore,

$$W \begin{pmatrix} \mathbf{r}_u \\ \mathbf{r}_v \end{pmatrix} = \frac{1}{EG - F^2} \begin{pmatrix} LG - MF & -LF + ME \\ MG - NF & -MF + NE \end{pmatrix} \cdot \begin{pmatrix} \mathbf{r}_u \\ \mathbf{r}_v \end{pmatrix} \quad \text{Equation 4.30}$$

This is the matrix representation of Weingarten, also known as shape operator. The Gaussian curvature can be also calculated by the determinant of this matrix:

$$K = \det(W) = \frac{LN - M^2}{EG - F^2} \quad \text{Equation 4.31}$$

According to the representation of shape operator, we can deduce:

$$\mathbf{n}_u \times \mathbf{n}_v = \det(W)(\mathbf{r}_u \times \mathbf{r}_v) = K(\mathbf{r}_u \times \mathbf{r}_v)$$

$$\Rightarrow |\mathbf{n}_u \times \mathbf{n}_v| = |K| \cdot |\mathbf{r}_u \times \mathbf{r}_v|$$

Denote $d\sigma = |\mathbf{r}_u \times \mathbf{r}_v| dudv$ as the area of the surface, which is formed by u , $u + du$, v , and $v + dv$, whereas $d\sigma_0 = |\mathbf{n}_u \times \mathbf{n}_v| dudv$ as the area on the unit sphere Σ projected by $d\sigma$. We can redefine the value of Gaussian curvature:

$$|K| = \frac{d\sigma_0}{d\sigma} \quad \text{Equation 4.32}$$

Let D denote a small neighborhood of a point P on the surface, then the area of $g(D)$ can be obtained by equation 34 and the mean value theorem:

$$\begin{aligned} A_0(g(D)) &= \int_{g(D)} d\sigma_0 = \int_D |K| d\sigma \\ &= |K(P)| \cdot \int_D d\sigma = |K(P)| \cdot A(D) \end{aligned}$$

As a result, the Gaussian curvature at an arbitrary point P can be represented as follow:

$$|K(P)| = \lim_{D \rightarrow P} \frac{A_0(g(D))}{A(D)} \quad \text{Equation 4.33}$$

This expression explains the geometry meaning the Gaussian curvature.

4.3 Estimation of Curvatures for Discrete Surface

In 3.1 section, all the calculations are on the basis of a sufficiently differentiable (at least to support the two fundamental forms) surface. However, in virtual reality field, it is complicated to use smooth surface to represent geometries, instead polygonal meshes (discretized surface) are extensively used for 3-dimensional (3D) geometries. The type of mesh we used to represent our skull is called triangular mesh, which is composed of vertices and triangular faces that form the outline of an object. Each triangle is formed by three vertices and connected with other by its edges (each triangle has three edges), and each vertex can be connected with various triangles. These discretized meshes are linear

surfaces, where the first and second order derivatives do not exist. In order to analyze the shape of a triangular mesh, researchers generally use two approaches to approximate the differential properties. Most popular way is surface reconstruction, which fits a small area of a vertex into a parametrized surface in order to obtain differential properties (Nigam and Agrawal 2013). Some researchers estimate differential properties (usually Gaussian and Principal curvatures) directly from a set of local points and faces from discrete surface (Nigam and Agrawal 2013). In the following section, we will introduce some of popular works that contribute to curvature approximation.

4.3.1 Curvature Estimation Review

In this section, we will introduce some classic methods for curvature approximation of triangular meshes.

4.3.1.1 Circular Fitting Algorithm

In (X. Chen and Schmitt 1992) work, they first designed an algorithm to estimate n number of (at least three) normal curvatures along different tangent vectors of a vertex P on a surface mesh. In order to estimate these curvatures, n vertex triples

$\{T_l = (P, P_i, P_j) \mid P_i, P_j \in N_p, 1 \leq l \leq n\}$ are defined, each of which forms a curve on the

surface that pass through the vertex P . They selected a triple in such way that P_i and P_j are two geometrically opposite points with respect to P . A circum-circle of (P, P_i, P_j) can be easily obtained with center C_l (Faux and Pratt 1979). They estimated the normal

curvatures $\kappa_l = \frac{1}{\|C_l - P\|}$ and according unit tangent vectors $\mathbf{n}_l = \frac{C_l - P}{\|C_l - P\|}$ by Meusnier

theorem: $\kappa_n = \kappa_l \cos \theta$, where θ is the angle between \mathbf{n}_l and

the unit normal vector \mathbf{N}_P of P.

From Euler formula 3.46 ($\kappa_n = \kappa_1 \cos^2 \theta + \kappa_2 \sin^2 \theta$) we have discussed in section 3.1, it is easy to calculate the normal curvature along any tangent direction with respect to the coordinate system formed by principal curvatures. Contrarily, (X. Chen and Schmitt 1992) transformed this expression to be representation of principal curvatures with respect to an arbitrary coordinate system on the tangent plane of P:

$$\xi_l = \frac{\cos \phi}{\sqrt{|\kappa_{n_l}|}}, \eta_l = \frac{\sin \phi}{\sqrt{|\kappa_{n_l}|}}$$

$$A\xi_l^2 + 2B\xi_l\eta_l + C\eta_l^2 = \pm 1$$

Where A, B and C are expressions with respect to κ_1 and κ_2 , $\{\xi_l, \eta_l\}$ represents coordinates of the new system, and ϕ is the angle between \mathbf{n}_l and the x-axis of the new system. They used the least square function to estimate the values of A, B and C, so as to obtain the principal values:

$$\kappa_1 = \frac{1}{2} \left(A + C + \sqrt{(A - C)^2 + 4B^2} \right)$$

$$\kappa_2 = \frac{1}{2} \left(A + C - \sqrt{(A - C)^2 + 4B^2} \right)$$

4.3.1.2 Iso-surface Construction Algorithm

(Taubin 1995) in his paper proposed an approach to estimate the tensor of the curvature of a surface, which is a measurement of the directional curvature $\kappa_p(T)$ at location P along unit tangent direction T:

$$\kappa_p(T) = u^T K_p u = \begin{pmatrix} n \\ t_1 \\ t_2 \end{pmatrix}^T \begin{pmatrix} 0 & 0 & 0 \\ 0 & \kappa_p^1 & 0 \\ 0 & 0 & \kappa_p^2 \end{pmatrix} \begin{pmatrix} n \\ t_1 \\ t_2 \end{pmatrix}$$

Where $T = nN + t_1T_1 + t_2T_2$ is a vector indicated by an orthogonal system $\{N, T_1, T_2\}$, $\kappa_p^1 = \kappa_p(T_1)$ and $\kappa_p^2 = \kappa_p(T_2)$ (Carmo 1976; Thorpe 1994). Note that $(0, \kappa_p^1, \kappa_p^2)$ are eigenvalues of the symmetric matrix K_p .

In order to estimate this curvature tensor, Taubin defined a symmetrical matrix M_p , which has the same eigenvector as K_p :

$$M_p = \frac{1}{2\pi} \int_{-\pi}^{+\pi} \kappa_p(T_\theta) T_\theta T_\theta^t d\theta, \quad T_\theta = \cos(\theta)T_1 + \sin(\theta)T_2$$

Which can be factorized as:

$$M_p = T_{12}^t \begin{pmatrix} m_p^{11} & m_p^{12} \\ m_p^{21} & m_p^{22} \end{pmatrix} T_{12}$$

According $\kappa_p^1 = M_p(T_1)$ and $\kappa_p^2 = M_p(T_2)$, it is easy to obtain such relations:

$$\begin{aligned}
m_p^{12} &= m_p^{21} = 0 \\
\kappa_p^1 &= 3m_p^{11} - m_p^{22} \\
\kappa_p^2 &= 3m_p^{22} - m_p^{11}
\end{aligned}$$

Let v denotes a vertex on a surface and $(v_j \mid j = 1, \dots, m)$ denotes m number of vertices within the neighborhood of v . To estimate M_p , Taubin first estimated a Matrix that with unknown coordinate system:

$$\tilde{M}_v = \sum_{v_j} \omega_{ij} \kappa_{ij} T_{ij} T_{ij}^t$$

Where T_{ij} is the tangent vector of the curve formed by v_i and v_j , κ_{ij} is curvature along T_{ij} , and ω_{ij} is the weight that is defined as the area (associated with v_i and v_j) proportioned to the total area of the neighborhood. In order to restrict this matrix in an orthogonal basis (but not $\{N, T_1, T_2\}$), Taubin utilized the Householder matrix:

$$Q_v^t \tilde{M}_v Q_v = \begin{pmatrix} 0 & 0 & 0 \\ 0 & \tilde{m}_v^{11} & \tilde{m}_v^{12} \\ 0 & \tilde{m}_v^{21} & \tilde{m}_v^{22} \end{pmatrix}$$

$$Q_v = I - 2W_v W_v^t, W_v = \frac{E_1 \pm N_v}{\|E_1 \pm N_v\|}$$

Where Q_v is a 3×3 matrix which first column is the normal vector of v , the rest two column represents orthogonal vectors \tilde{T}_1 and \tilde{T}_2 on the tangent plane of v . The final task is to rotate this system so that the matrix $Q_v^t \tilde{M}_v Q_v$ can be diagonalized.

4.3.2 Gauss Bonnet Scheme

(Meyer et al. 2003) proposed a method to estimate the mean and Gaussian curvatures utilizing only one-ring neighborhood of a vertex v . According Euler-Lagrange equation, Meyer gave such definition about mean curvature normal:

$$K = 2\kappa_H \mathbf{n} = \lim_{diam(A) \rightarrow 0} \frac{\nabla A}{A}$$

Where A is the area of neighborhood of a point P on a surface while the diameter of A is infinitely small, and ∇ is the gradient of the area (Gray 1997). Consequently, he gave the expression of the mean curvature normal operator with respect to the Vertex v and vertices v_j within the one-ring neighborhood:

$$K(v) = \frac{1}{2A_{Mixed}} \sum_{j \in N_1(v)} (\cot \alpha_j + \cot \beta_j)(v - v_j)$$

Where α_j and β_j are two angles indicated in Figure, and $N_1(v)$ is the vertices in the one-ring neighborhood of vertex v , and A_{Mixed} is calculated by Voronoi areas around v (Meyer).

We have also mentioned the geometry meaning of Gaussian curvature in 3.53:

$$\kappa_G = \lim_{diam(A) \rightarrow 0} \frac{A^G}{A}$$

Meyer approximated the Gaussian curvature on the triangular mesh:

$$\kappa_G(v) = (2\pi - \sum_{f_i \in N_1(v)} \theta_i) / A_{Mixed}$$

Where f_i is faces that within the one-ring neighborhood of the vertex v , and θ_i is the angle associated with the vertex v in f_i .

4.3.3 Algorithm of Curvature Estimation

In this section, we will discuss the algorithm of principal curvature estimation for triangular meshes in details, which plays a key role in our skull shape analysis (Dong and Wang 2005). Their first step is to approximate the unit normal vector of each vertex on the mesh. Next, the normal curvatures of each vertex will be estimated, in order to calculate the principal curvatures.

4.3.3.1 Vertex Normal

Consider a surface mesh $G = (V, F)$, where V represents a set of vertices in the surface and F defines triangular faces that link those vertices together. For each triangular face f , it is easy to obtain the unit normal vector \mathbf{n}_{f_i} . The normal vectors of all the faces are pointed to one side of the surface. To find the tangent plane of a vertex in the mesh, Dong and Wang took advantage of the faces in the vicinity of this vertex, which could be k -ring faces around the vertex. Let $v \in V$ be a vertex on the mesh G , and f_i denotes faces in one-ring neighborhood of v . The normal vector \mathbf{n}_v of vertex v can be averaged by weighted normal vectors of faces that are in the one-ring neighborhood of v :

$$\mathbf{n}_v = \frac{\sum_{i=1}^m w_i \mathbf{n}_{f_i}}{\left\| \sum_{i=1}^m w_i \mathbf{n}_{f_i} \right\|}, \quad w_i = \frac{1}{\|c_{f_i} - v\|} \quad \text{Equation 4.34}$$

Where \mathbf{n}_{f_i} is the unit normal vector of face f_i and c_{f_i} is the coordinate of the centroid of face f_i . The method to define the weight of face f_i was proposed by (S.-G. Chen and Wu 2004).

4.3.3.2 Normal Curvature Estimation

Let $r(s)$ denote a parametrized curve passing through vertex v , where s is the arc length of the curve that satisfies $r(0) = v$. If $\mathbf{N}(s)$ defines the normal vector of $r(s)$, then we can attain such expression according to the definition of normal curvature:

$$\kappa_n = - \left. \frac{\langle dr, d\mathbf{N} \rangle}{ds^2} \right|_{s=0}$$

Therefore, we can further obtain such relationship:

$$\kappa_n = - \frac{\langle dr, d\mathbf{N} \rangle}{\langle dr, dr \rangle} = - \lim_{\|\Delta r\| \rightarrow 0} \frac{\langle \Delta r, \Delta \mathbf{N} \rangle}{\|\Delta r\|^2}$$

For each vertex v , there are a series of vertices v_j ($j = 1, 2, 3 \dots m$) surrounded it in the area of one-ring neighborhood. Let assume the distance between v_j and v is small enough, and is therefore we have:

$$\kappa_n(\mathbf{t}_j) = -\frac{\langle v_j - v, \mathbf{n}_{v_j} - \mathbf{n}_v \rangle}{\|v_j - v\|^2} \quad \text{Equation 4.35}$$

Where \mathbf{t}_j indicate the tangent vector of the curve that forms v_j and v . We can interpret this tangent vector \mathbf{t}_j as the projection of vector $(v_j - v)$ on the tangent plane of v .

Therefore,

$$\mathbf{t}_j = \frac{(v_j - v) - \langle v_j - v, \mathbf{n}_v \rangle \mathbf{n}_v}{\|(v_j - v) - \langle v_j - v, \mathbf{n}_v \rangle \mathbf{n}_v\|} \quad \text{Equation 4.36}$$

4.3.3.3 Approximation of Principal, Gaussian and Mean Curvatures

(Dong and Wang 2005) introduced the least square method from (X. Chen and Schmitt 1992) to estimate principal curvatures. In this section, we will explain this method in detail. From previous discussion, we know that normal curvatures of a vertex v has such relation $\kappa_n = \kappa_1 \cos^2 \theta + \kappa_2 \sin^2 \theta$, where κ_1 and κ_2 are principal curvatures, and θ is the angle between κ_1 and κ_n . Since the direction of κ_1 and κ_2 are unknown, (Dong and Wang 2005) proposed to select an arbitrary coordinate system $\{\hat{e}_1, \hat{e}_2\}$ on the tangent plane. Let θ_0 denote the angle between the direction of κ_1 and \hat{e}_1 , and θ_j denote the angle between the direction of \mathbf{t}_j and \hat{e}_1 . Therefore, the Euler formula can be converted to:

$$\kappa_n(\mathbf{t}_j) = \kappa_1 \cos^2(\theta_j - \theta_0) + \kappa_2 \sin^2(\theta_j - \theta_0)$$

$$= a \cos^2(\theta_j) + b \cos(\theta_j) \sin(\theta_j) + c \sin^2(\theta_j) \quad \text{Equation 4.37}$$

Where the constants a, b, c can be represented with respect to κ_1 , κ_2 and θ_0 :

$$\begin{cases} a = \kappa_1 \cos^2 \theta_0 + \kappa_2 \sin^2 \theta_0 \\ b = 2(\kappa_2 - \kappa_1) \cos(\theta_0) \sin(\theta_0) \\ c = \kappa_1 \sin^2 \theta_0 + \kappa_2 \cos^2 \theta_0 \end{cases}$$

If we use the maximum normal curvature κ_{\max} among $\kappa_n(\mathbf{t}_j)(j = 1, \dots, m)$ to build the coordinated system $\{\hat{e}_1, \hat{e}_2\}$, where the direction of κ_{\max} is \hat{e}_1 , it is easy to obtain

$a = \kappa_{\max}$. Therefore, b and c can be estimated as:

$$b = \frac{\omega_{13}\omega_{22} - \omega_{23}\omega_{12}}{\omega_{11}\omega_{22} - (\omega_{12})^2}, c = \frac{\omega_{11}\omega_{23} - \omega_{12}\omega_{13}}{\omega_{11}\omega_{22} - (\omega_{12})^2}$$

Where:

$$\omega_{11} = \sum_{j=1}^m \cos^2(\theta_j) \sin^2(\theta_j), \omega_{12} = \sum_{j=1}^m \cos(\theta_j) \sin^3(\theta_j)$$

$$\omega_{21} = \omega_{12}, \omega_{22} = \sum_{j=1}^m \sin^4(\theta_j)$$

$$\omega_{13} = \sum_{j=1}^m (\kappa_n(\mathbf{t}_j) - a \cos^2(\theta_j)) \cos(\theta_j) \sin(\theta_j)$$

$$\omega_{23} = \sum_{j=1}^m (\kappa_n(\mathbf{t}_j) - a \cos^2(\theta_j)) \sin^2(\theta_j)$$

(Dong and Wang) also gave the relationship between the constants and the curvatures :

$$\kappa_G = \kappa_1 \kappa_2 = ac - b^2 / 4, \kappa_H = (\kappa_1 + \kappa_2) / 2 = (a + c) / 2$$

$$\kappa_{1,2} = \kappa_H \pm \sqrt{\kappa_H^2 - \kappa_G} \quad \text{Equation 4.38}$$

Where κ_G is the Gaussian curvature, κ_H is the Mean curvature, and $\kappa_{1,2}$ are the Principal curvatures.

In summary, the above algorithm for calculating the Principal curvatures of a vertex utilized one-ring neighborhood of faces and vertices. Alternatively, it is implementable to involve k-ring neighborhood in this algorithm if necessary. In our work, we choose two-ring neighborhood, trying to smooth local noises during mesh simplification meanwhile to keep Δr (distance between v and v_j) as small as possible for accuracy. In addition, we would only take advantage of the maximum curvature κ_1 in our evaluation tool.

4.4 Skull Shape Evaluation Tool utilizing Statistical Modeling

In this section, we will delve into how we developed the statistical model so as to assess the deformity of the skull shapes. As shown in Figure 4.1, the flow chart summarizes the whole modelling procedures, and which steps will be followed for each set of head scans. All the results will be plotted onto a two dimensional Figure with respect to two parameters, which we believe to best depict a skull shape. One of the variable is Cranial Index ($CI = \frac{skull_width}{skull_length} \times 100$), which is a traditional method in clinics to generally evaluate a skull shape, and the other one is the summarization of a curvature distribution, which

characterizes the local variance of the skull. Since the cranial index is a constant for each head scan, therefore, the key role in our modelling is to investigate a proper way to summarize the curvature distribution. A set of training data, which includes typical cases from each type of craniosynostosis, will be carefully selected to explore the best solution to differentiate curvature distributions among the types. Within the procedures, we believe there are three steps indicated by $\omega_{1,2,3}$ that could influence our final result. We proposed several options to implement each of the steps. With more data studied, we will adjust our simplification method ω_1 , skull normalization ω_2 , and the way to explain the curvature distribution ω_3 in order to make the result patterns as obvious as possible. More details for each step will be elaborated in the following sections.

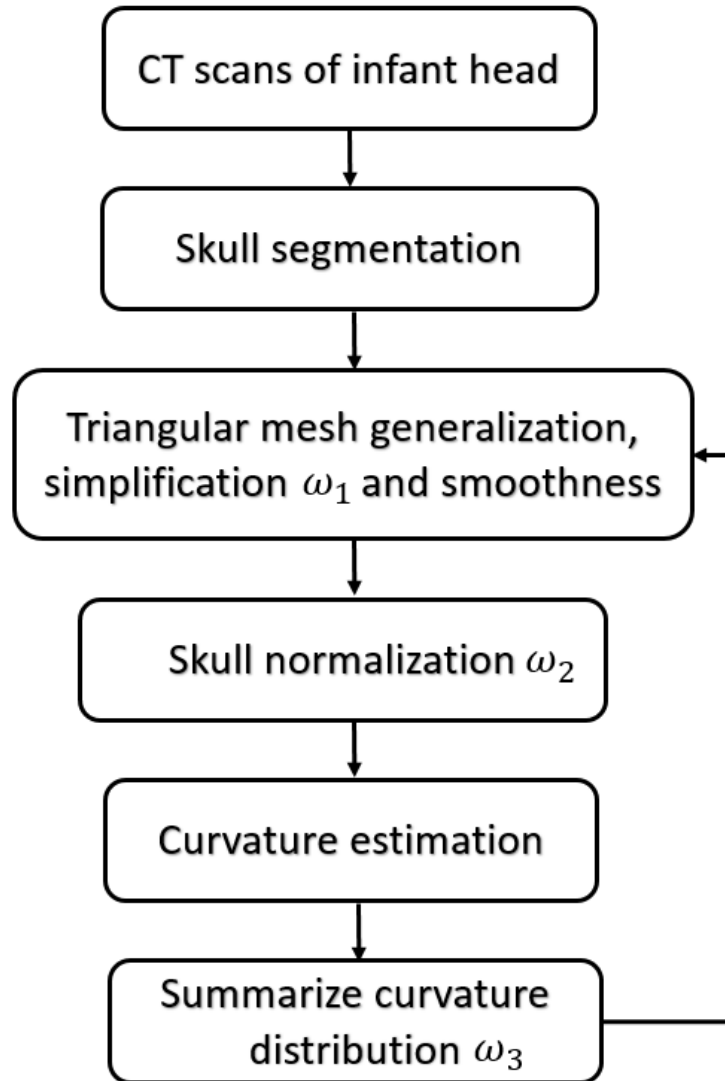


Figure 4.1: This is the flow chart of our statistical modeling, where $\omega_{1,2,3}$ will be adapted while more input data are involved in the training.

4.4.1 Material Preparation

The first task of developing a model is to collect CT scans of infant's head. We were able to review a certain number of CT scans of Craniosynostosis patients (in the format of

DICOM) from our university hospital database with ages from newborn to one-year-old (age when diagnosed) between years 2003 – 2012. In addition, we have a set of CT images from a normal baby with three-week-old, which shape will be considered as our golden standard normal shape in the following analysis. Patients that suffered from scaphocephaly, trigonocephaly, brachycephaly and plagiocephaly were selected to be differentiated from the normal in our system. CT scans, which voxel size is bigger than $0.4\text{mm} \times 0.4\text{mm} \times 2.0\text{mm}$ were excluded. Finally, we obtained five scaphocephaly patients, six trigonocephaly patients, two brachycephaly patients and two plagiocephaly patients as quantified data in total. In this paper, we will only use the preoperative head scans from these patients, to form a set of training data and another set of test data. Our training data includes two scaphocephaly cases, one trigonocephaly case, and two brachycephaly cases, which were selected carefully in order to best capture the shape features. The rest of the data formed our test data in order to validate our optimum system that adapted by the training data.

4.4.2 Skull segmentation and surface generation

In order to obtain 3D representation of the skull shapes, we segmented each set of our CT images with a software called Amira (Amira 5 User's Guide), which is a platform that allows to visualize, manipulate medical 3D images. With voxel labeling method in Amira, we labeled image intensities that are higher than 100 Hounsfield Units (HU) as cranial bones. As mentioned in the previous section, the cranial bones that associated with surgical correction are membranous bones, including left/right frontal bones, left/right parietal bones, planum occipital, and flat part of temporal bone according to infant's skull anatomy.

Therefore, the rest of the bone structures that have been labelled in the segmentation view were unselected. We stopped labelling the left/right frontal bones when the left/right orbital cavity starts to display, and we erased the portion of temporal bones, in which the structure is more complicated than a curved plane. The planum occipitale, which is the squama part of the occipital bone, contributed to our skull shape models until the occipital bone reached to the foramen magnum structure.

With the desired skull structures labelled, we proceeded to construct the surface outline of the skull shape. We picked the “existing weights method” from surface generation tools found in Amira, to extract the two-layered skull shape with triangular meshes. One layer represented the outer surface, the part of the skull that is in touch with skin, the other layer indicated the inner surface that encloses the brain. In order to mitigate time-consuming analysis and in the meantime preserve enough details of the shape, a fast but constrained simplification method (the parameter distance was set to 3) supplied in Amira was adopted.

Since the curvature estimations for a discrete surface depends on the construction of vertices and faces, which compose the skull surface, we therefore designed four ways by which to acquire the simplified skulls in order to investigate the best solution for the rest of the shape analysis. The first approach was to continually simplify the skull models until the number of faces in the mesh ceased to decrease any further. The second method was to simplify all the skulls to a certain number of faces, in our case, 50,000. Alternatively, we halved the total number of triangular faces by four times for each skull. The final approach was to set the number of vertices in the skull meshes of a specific type of craniosynostosis at the same level (± 500).

Surface smoothing was applied subsequently to attenuate disturbances resulting from simplification. For the smoothing parameters requested from Amira, we assigned 0.6 for the diffuse factor and 20 for the iteration times.

4.4.3 Intracranial Volume Normalization

While head shapes vary in everybody, there is a general shape for Caucasians, or Africans, or Asians. In addition, even if two babies have similar skull shapes but with different intracranial volume (again head circumference varies at birth), the curvature distributions would be different as well, and the baby who has a larger volume tends to have a lower curvature distribution. Although our evaluating system attempted to catch the differences among skull shapes, this was not possible for this case. As a result, we planned to normalize the intracranial volume. With two similar skull shapes, if we uniformly scale one of them so that its skull width was the same as the other one, its intracranial volume would be close to the other with a similar range of curvature values. With such a standpoint, our normalization task became to find the skull width and length for each patient, where the skull length was for the calculation of cranial index.

We developed an algorithm to semi-automatically search for the skull width and length, and we set our only normal skull as a reference. The algorithm required that we recognized the orientation of the skull model, and therefore we decided to manually define the sagittal plane of the skull. Since at least three points were needed to define a plane, we picked the center of the skull as a contribution, and two other locations that would be manually selected on the skull mesh. The skull centroid was calculated with the weighted average of face locations on the mesh:

$$cen = \sum_{i=0}^n \frac{A_{f(i)}}{A_0} * Pos_{fcen(i)}, Pos_{fcen(i)} = \sum_{j=0}^2 Pos_{v(j)} \quad \text{Equation 4.39}$$

where n is the total number of faces in a skull model, $Area_{face(i)}$ is the area of the i^{th} face, $Pos_{fcen(i)}$ is the centroid of this i^{th} triangular face, and $Pos_{ver(j)}$ is the position of j^{th} vertex from a triangular face.

The second point we selected was at the bottom of the frontal suture of our model, which should have been close to the nasion (the intersection of the frontal bone and the two nasal bones). The third point was chosen at the external occipital protuberance, which is a protruding point located at the middle of the squamous part of occipital bones. Then it was easy to obtain the normal of this sagittal plane:

$$\mathbf{n} = \frac{\mathbf{v}_{p21} \times \mathbf{v}_{p22}}{|\mathbf{v}_{p21}| |\mathbf{v}_{p22}|} \quad \text{Equation 4.40}$$

Where v_{p21} is the vector pointing from the centroid to the second point, and v_{p31} is the vector pointing from the centroid to the third point.

With the normal of the sagittal plane, it was then easy to find such a line along this normal direction through the centroid of the skull, intersecting with both the left and right side of the skull. We took the distance between these two intersected points as the skull width.

To calculate the skull length, we first explored the farthest position of the skull mesh that was within the sagittal plane from the center point. We determined whether a vertex was within the sagittal plane in such a way:

$$\frac{\mathbf{n} \cdot \mathbf{v}_{ci}}{|\mathbf{v}_{ci}|} < \tau \quad \text{Equation 4.41}$$

Where \mathbf{v}_{ci} was the vector from the centroid of the skull to the center of the i^{th} face and the value of the tolerance in our case was 0.0001. The second investigation that followed was to find another vertex in this sagittal plane that had the longest distance from the previous location. The distance between these two locations was defined as the skull length.

4.4.4 Curvature Distribution for One Skull Shape

We decided to use curvature to characterize the shape of skull, since it is an intrinsic property of a geometry. It describes if a local area on a surface tends to spread as a plane (small value) or wrap as a sphere (large value). The algorithms of curvature estimation for discretized surface was elaborated in 4.3.3 section. We chose this method since it is robust and implementable to involve vertices in k-ring neighborhood. One curvature value we obtained from above algorithm is only a representation for one vertex on a surface mesh since it only depicts the local changes. Each skull mesh is composed of a huge amount of vertices, and therefore, we obtained a series of curvature values for each skull shape.

We used curvature distribution to render the set of curvature values on a 2D Figure, which x-axis represented curvature values and y-axis indicated the percentage of vertices in a mesh that have the same curvature values. If a smooth object tends to be spherical, the distribution should be narrow and tall, whereas the distribution of an ellipsoidal skull shape should be shorter but wider. We expected that similar skull shapes in the same scale should have similar distributions, so that we could capture the different types of the skull shapes by the different patterns of curvature distributions. However, for discretized manifolds with

lots of noises, it was hard to obtain exactly the same curvature values for even two vertices in a mesh. Therefore, we need to divide the range of this set of vertices into segments.

Since the shape of a normalized skull was close to ellipsoid, the range of curvatures can be decided. We set the range of curvature values that we were interested to be 0 to 0.08, then further divided this range into small bins, each of which should have the same value (e.g. bin=0.001 or 0.005). As a result, each bin represented a smaller range of curvature values within (0, 0.08). The curvature value of a vertex that falls into any curvature range should contribute to the y-axis (percentage of vertices) of the corresponding bin. Figure 4.2 indicates some curvature distributions of some of our patients, each of which is from a type of skull shapes. We can see that most of the vertices from the normal skull (black line) fall into the curvature range between 0.25 to 0.30, whereas most of the vertices from the brachycephaly patient (blue line) fall into the range between 0.03 to 0.04. The curvature distribution of both scaphocephaly and trigonocephaly patients are rather fat and short, and the distribution of the trigonocephaly patient (red line) leans on the right while the one of the scaphocephaly patient (green line) shifts toward left.

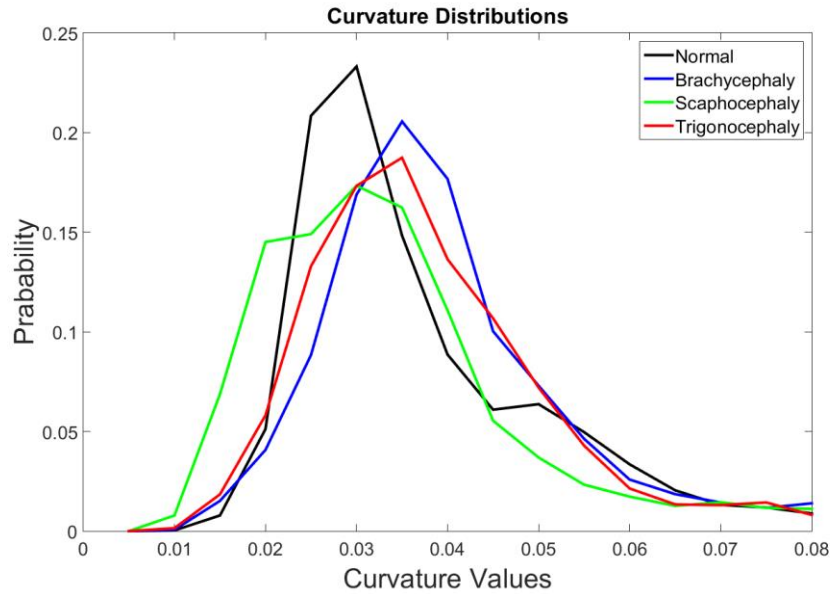


Figure 4.2: Curvature distributions of patients that from various types of skull shapes.

4.4.5 Statistical Modeling

In order to study the pattern of different types of skull shape, we designed to use two parameters as contributions. One parameter is cranial index that roughly describe the scale of the skull volume, the other is curvature distribution of a skull. However, curvature distribution is a curve that represents how curvature values of a mesh behave within a certain range. The pattern of curvature distribution is variant depending on different types of shape. Therefore, our task now is to find a way to summarize the pattern of curvature distribution into one variable.

It is known that in statistics, moment is a common way to quantify the shape of a distribution curve or a set of points. There are four significant moments called mean (1st

moment), variance (2nd moment), skewness (3rd moment) and kurtosis (4th moment) respectively.

Mean is also called raw moment, which is the weighted average of any possible value

$$\bar{x} = \sum xp(x) \quad \text{Equation 4.42}$$

where the possible values in our case are the curvature values within the interested range and the weight is the percentage of vertices with respect to a possible value. Variance evaluates how the other values deviate from the mean value. The formula to calculate the variance is:

$$\mu_2 = \sum (x - \bar{x})^2 p(x) \quad \text{Equation 4.43}$$

The skewness is the standardized third moment, which measures the asymmetry and imbalance from the mean value of a distribution:

$$s = \frac{\mu^3}{(\mu^2)^{3/2}} = \sqrt{n} \frac{\sum (x - \bar{x})^3}{(\sum (x - \bar{x})^2)^{3/2}} \quad \text{Equation 4.44}$$

Where the normalization allows its independency of any linear change of scale. If the value is 0, the distribution will be symmetry from the mean value, whereas other values indicates if a distribution is lean on either left (positive value) or right (negative value) side. The kurtosis is defined as normalized fourth moment:

$$k = \frac{\mu_4}{(\mu_2)^2} = n \frac{\sum (x - \bar{x})^4}{(\sum (x - \bar{x})^2)^2} \quad \text{Equation 4.45}$$

It measures the weight of the tail for a distribution. If the value of k is 3, the distribution is a normal distribution. If the value is higher, then the distribution tends to have long and fat tails, whereas the distribution tends to have short tails when the kurtosis is lower than three.

Considering the geometrical meanings of these significant moments, we decided to utilize kurtosis to measure the shape of the distributions. In order to adapt to our algorithm, we further adjusted this kurtosis method as follow:

$$\begin{aligned} \mu &= \sum_{i=1}^n \log_{10} i * \log_{10}(p_i) \\ m_2 &= \sum_{i=1}^n (\log_{10} i - \mu)^2 * \log_{10}(p_i) \\ m_4 &= \sum_{i=1}^n (\log_{10} i - \mu)^4 * \log_{10}(p_i) \\ nrk &= n * \frac{m_4}{m_2^2} \end{aligned} \quad \text{Equation 4.46}$$

We defined this adjusted method as normalized relative kurtosis (NRK).

4.5 Results of Evaluating System

In the previous sections, we have elaborated the procedures to statistically develop an evaluating system for skull shape measurement, which allows neurosurgeons to see how much a skull deviates from the normal shape. This skull assessment system was built with the concept of learning machine algorithm, exploring a best option among all the

possible values of parameters with a training data and using test data for validation. In the following section, we will demonstrate results from our investigation and the results from testing data. After validation, we will apply our evaluating system for surgical cases, showing the difference between preoperative and postoperative results.

4.5.1 System Optimization

The shapes of skull are variant, however, for each type craniosynostosis, the skull shapes tend to be similar. Statistically, normal babies tend to have ellipsoid-like skulls, scaphocephaly patients have long boat-shape skulls, and triangular skull shapes should be trigonocephaly. Therefore, we first attempted to classify the deformity indices of the skull shapes by types. Due to the limitation of clinical data, we selected six patients from different types of skull shapes, including one normal baby, two brachycephaly, two scaphocephaly and one trigonocephaly. We chose these patients because they all had typical shapes of their corresponding type of craniosynostosis, without other synostosis combined.

We have also discussed in chapter four that in the system, there are several steps that might affect the final result, which are mesh simplification, skull normalization, and the value of bin. In the following content, we will demonstrate how these steps affect the performance of our system. For each step, we designed several options to implement respectively and we tried every combination of these features to explore the optimum system. In the following sections, we will illustrate the results obtained from the potential methods of each feature.

4.5.1.1 Mesh Simplifications

We designed four ways of mesh simplification for investigation. The first method was to make all the surface meshes the same number of faces. The second approach was to reduce the faces until they cannot anymore. The third way was to halve the number of surface meshes four times. The last one was to maintain the number of vertices of meshes that were the same type in the same range (allows ± 500 difference). All the other parameters are maintained the same. The iteration value for surface smoothness was set to 20, all the skulls were normalized and the bin value was 0.005. We represented a skull shape with both cranial index and normalized relative kurtosis (NRK) of its curvature distribution.

Figure 4.3 indicates various skull shapes, which were all composed of 50000 triangular faces. The black dot is from a normal baby, the two green dots indicate scaphocephaly cases, the blue dots represent two Brachycephaly cases, and the red one is from a trigonocephaly patient. From the x-axis, we can see that scaphocephaly patients have obviously lower values than others, the trigonocephaly skull was close to normal shape, and the values of the two brachycephaly cases are relatively higher than the others. However, the shape indices are not distributed as we expected, and should be differentiated by types. One brachycephaly patient was at the same level as the normal patient, and one scaphocephaly case has the highest value while the other scaphocephaly case has the lowest NRK.

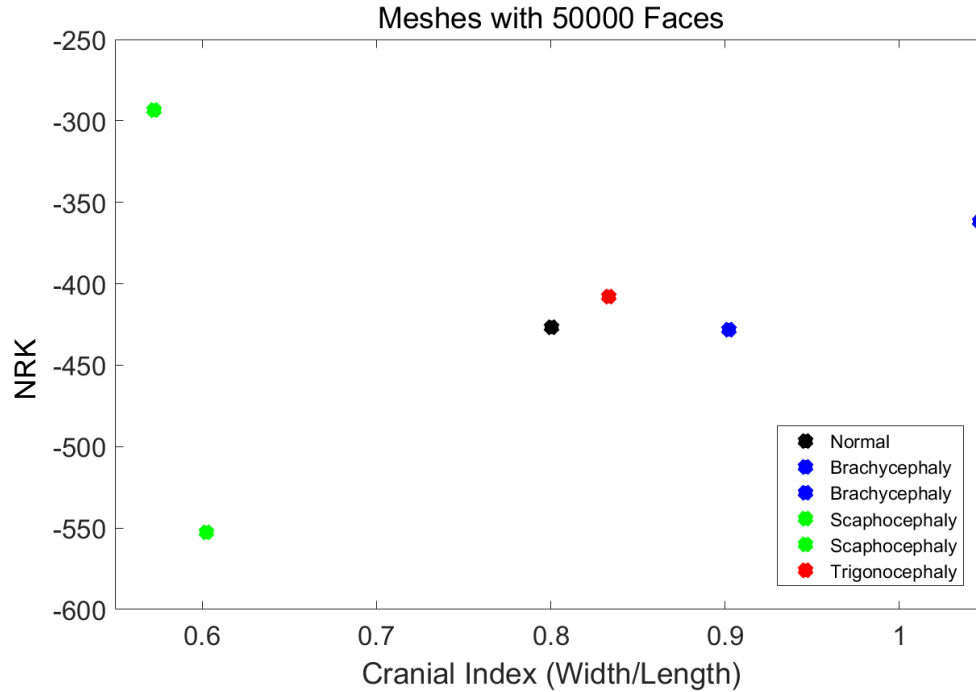


Figure 4.3: Results from training data, which the number of faces of each surface mesh is 50000.

Figure 4.4 represents skull meshes that were simplified until the number of faces stopped changing. The x-axis still shows the same values as previously, but the shape indices changed. The NRK of the normal skull was separated from pathological cases; however, one value related to scaphocephaly was higher than the trigonocephaly and brachycephaly patients; meanwhile the NRK of the other scaphocephaly case was the lowest. Therefore, this method was not able to classify the types of skull shapes well.

Figure 4.5 demonstrates skull meshes, whose number of faces were all halved four times. On the basis of previous method, we further manipulate the skull meshes with similar numbers of vertices (allowing ± 500 difference), which result is shown in Figure 4.6. Under both simplification methods, the types of craniosynostosis were able to be differentiated

according to similar patterns. The normal skull is indicated with the lowest NRK, whereas the trigonocephaly skull has a relatively higher value. The shape indices of the brachycephaly patients are higher than the trigonocephaly patient's, and the scaphocephaly cases have the highest value. The values for scaphocephaly deviate furthest from the normal case, which makes sense given that this type of skull is deformed the most. In addition, the value for trigonocephaly is the closest to normal while the shape of this type of skull is similar to the normal shape except that the forehead and the cranial index are in the same range as normal.

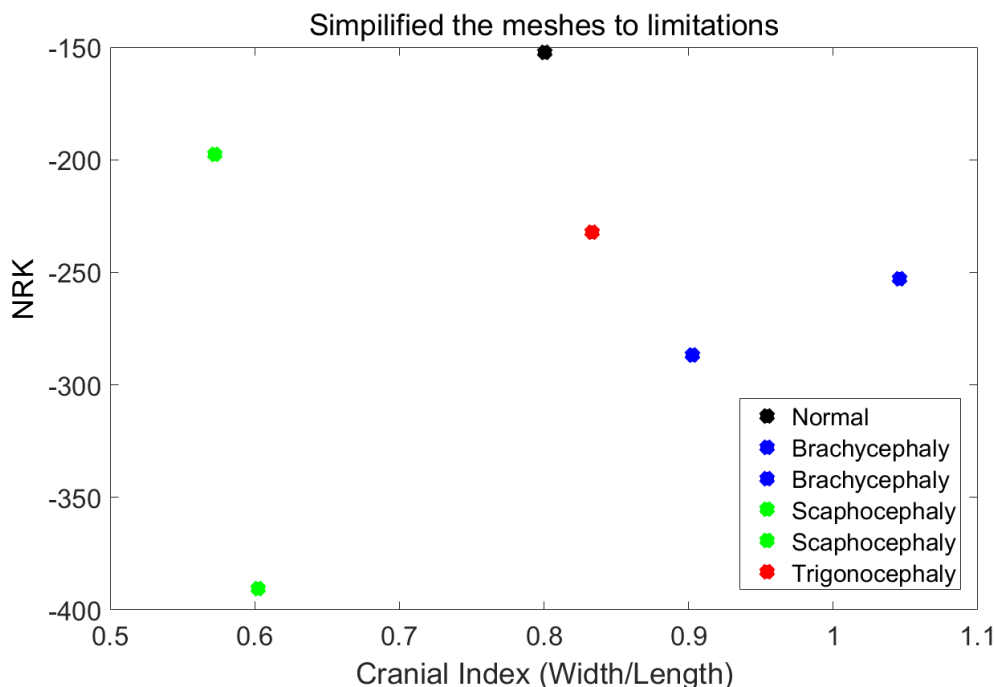


Figure 4.4: Quantified results with the second mesh simplification method, which reduces the number of faces to the limitations.

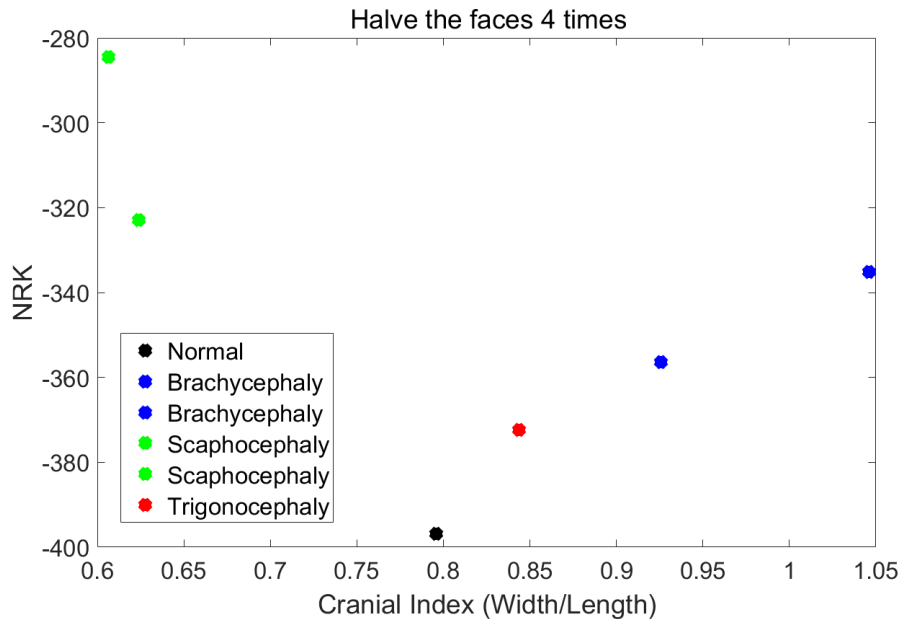


Figure 4.5: NRK vs cranial index with different skull shapes, which number of faces were halved four times

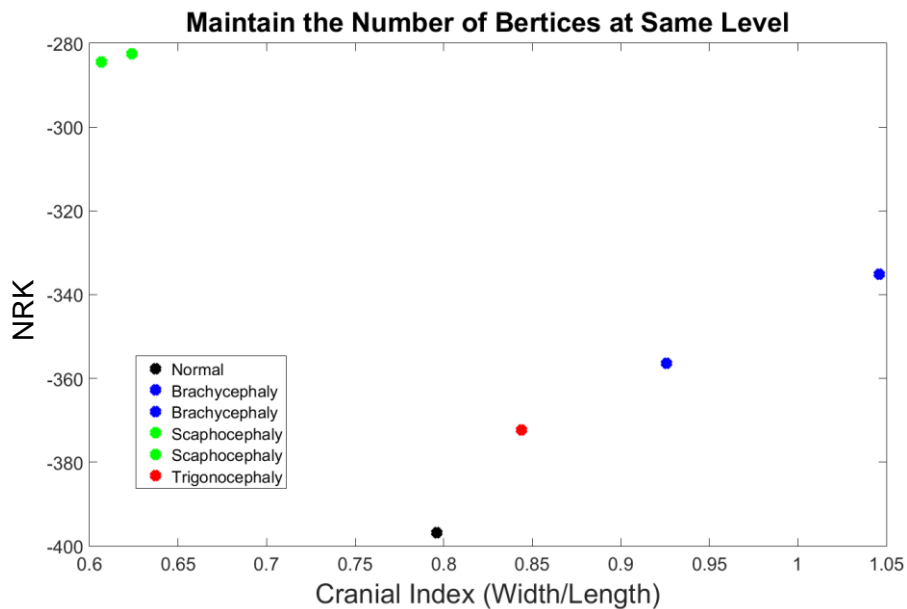


Figure 4.6: NRK vs cranial index with different skull shapes, which number of vertices were at the same level.

4.5.1.2 Skull Normalization

With a selected mesh simplification method, we attempted to test if skull normalization is necessary or not. With the optimized simplification method and $\text{bin} = 0.005$, we inputted the training data into our system without normalization as displayed in Figure 4.7. The NRK of the trigonocephaly skull is higher than the indices of the brachycephaly cases, and the value of one of the scaphocephaly cases is at the same level as the trigonocephaly one. Therefore, without skull normalization, the scaphocephaly and trigonocephaly shapes cannot be differentiated well. In addition, the NRK of the trigonocephaly skull is unexpectedly higher than the brachycephaly cases. As a result, we decided to continue with skull normalization in the following experiments.

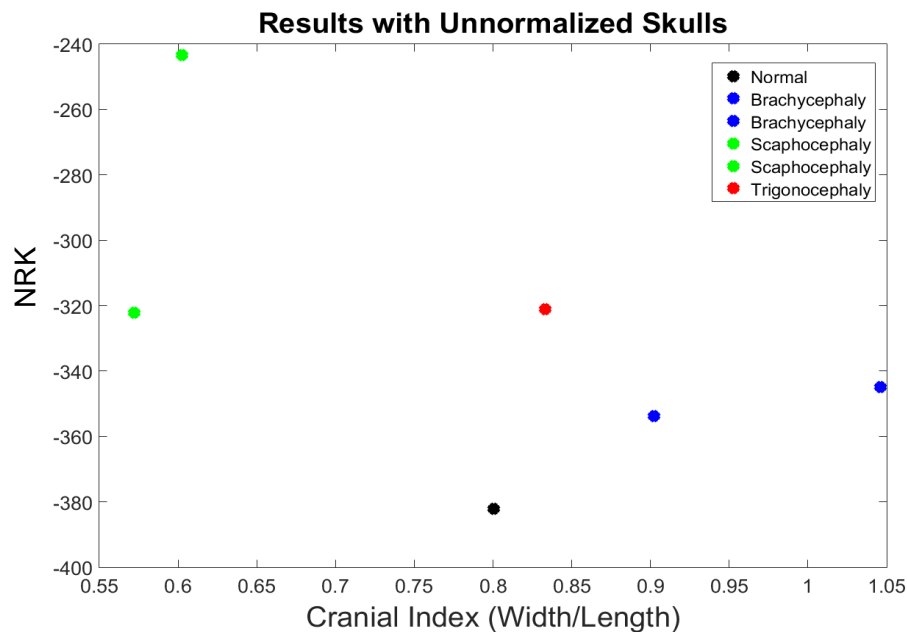


Figure 4.7: Skulls without normalization.

4.5.1.3 The Bin Values

In this section, we will indicate our exploration of an optimal value of bin in order to better classify the types of skull shapes. We tried bin values from 0 to 0.01, increasing 0.0005 every time.

From Figure 4.8 to 4.10, we indicate the results with different values of bin, which are 0.0005, 0.001 and 0.01. At these values, the results from the skull shapes could not enable our characterization of the types of craniosynostosis from normal, because the values of brachycephaly patients all overlapped with the values of trigonocephaly cases.

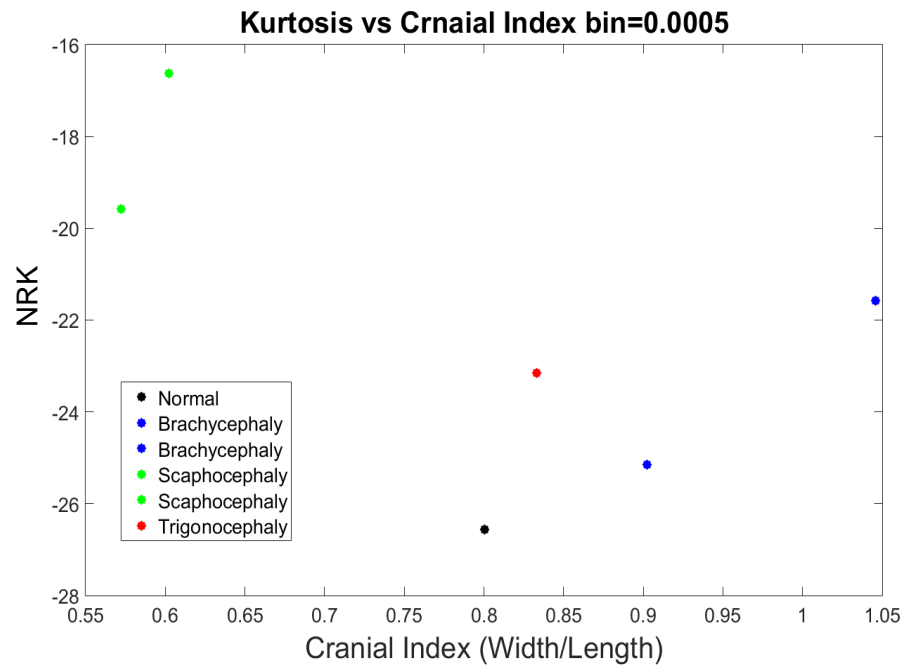


Figure 4.8: The measurements of skull shapes with bin=0.0005.

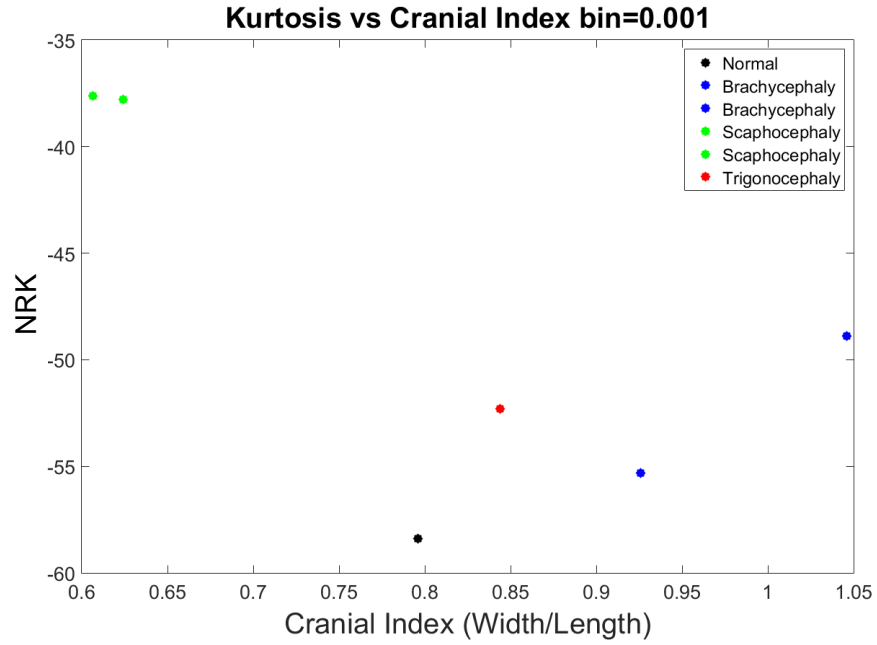


Figure 4.9: The measurements of skull shapes with bin=0.001.

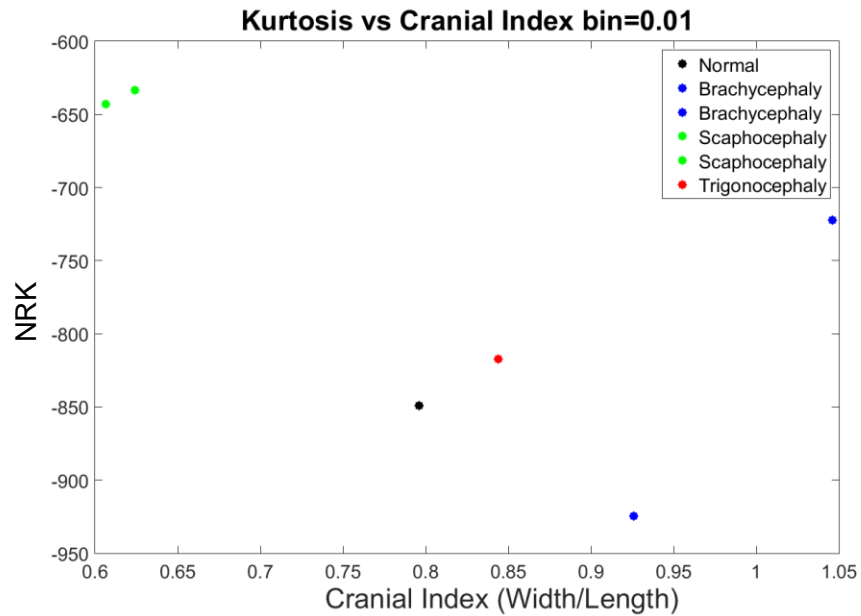


Figure 4.10: The measurements of skull shapes with bin=0.01.

From Figure 4.11 to 4.14, we indicate the results with other values of bin, which are 0.004, 0.005, 0.006 and 0.008. With these values respectively, our system was able to demonstrate the types of craniosynostosis well, from which we could see that both Figures 4.12 and 4.14 best differentiate the craniosynostosis types, but these types are indicated with different patterns, where the shape indices of the brachycephaly cases are higher than the trigonocephaly case in Figure 4.11, whose pattern is inverted in Figure 4.13. Since we hope that with a closer cranial index to the normal case, the NRK should be closer to normal, we preferred bin = 0.005 as the most appropriate value.

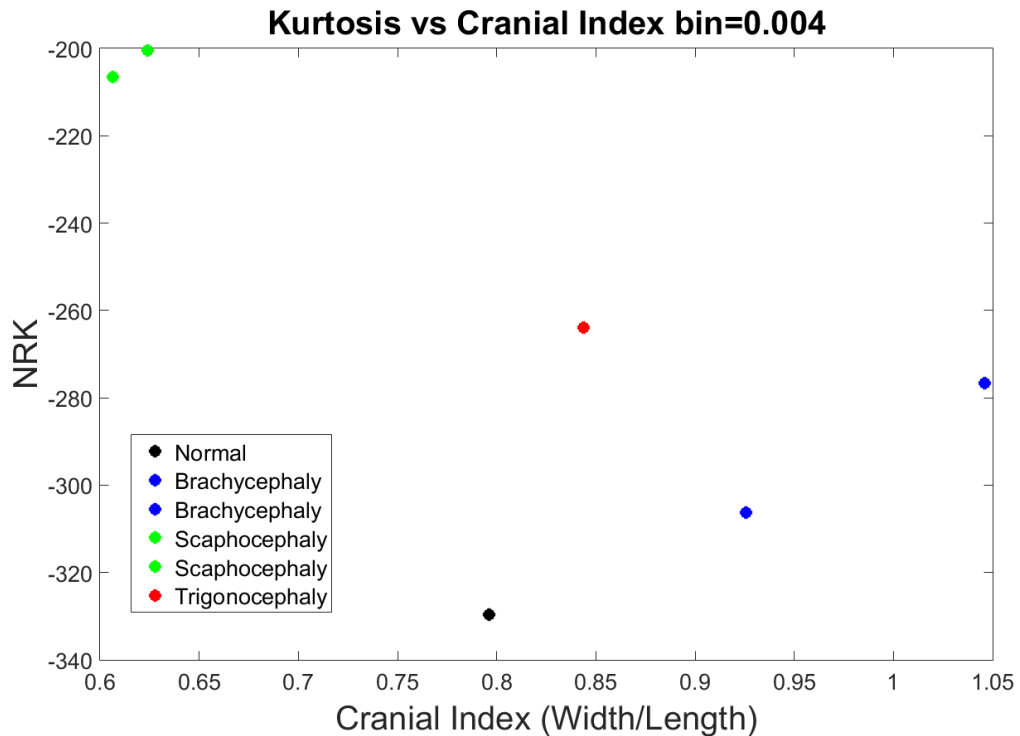


Figure 4.11: The measurements of skull shapes with bin=0.004.

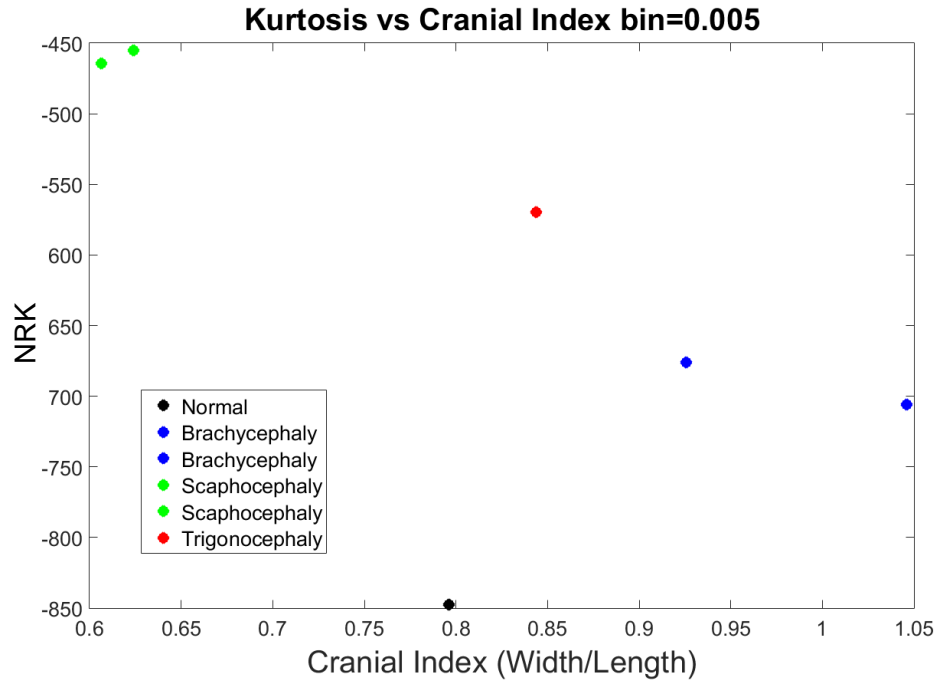


Figure 4.12: The measurements of skull shapes with bin=0.005.

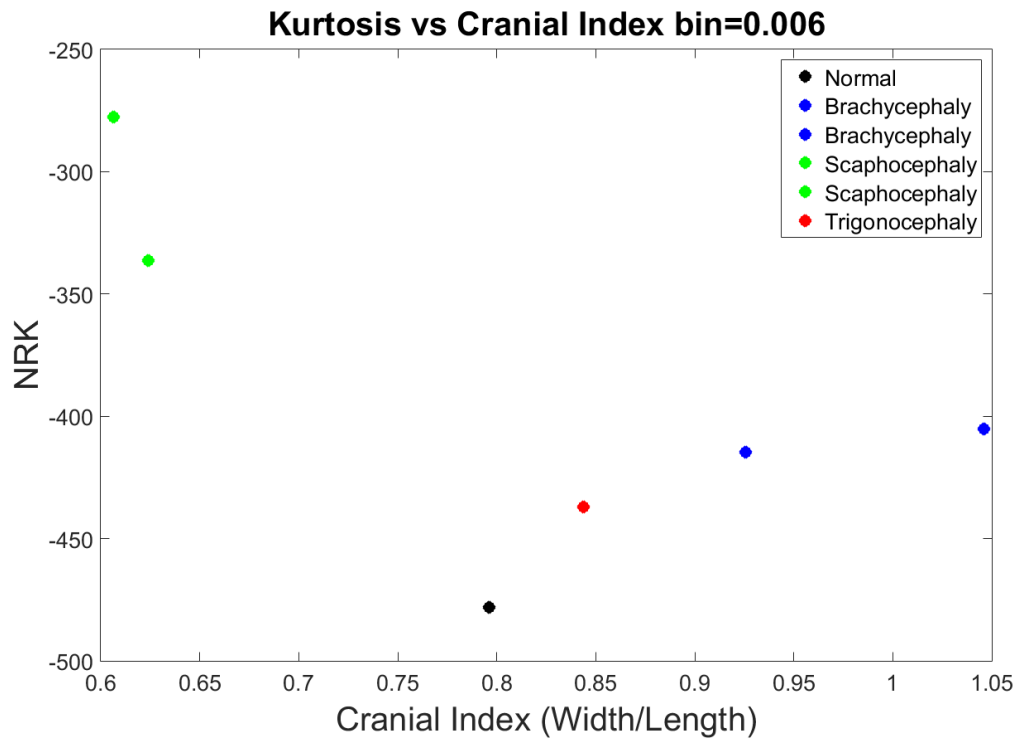


Figure 4.13: The measurements of skull shapes with bin=0.006.

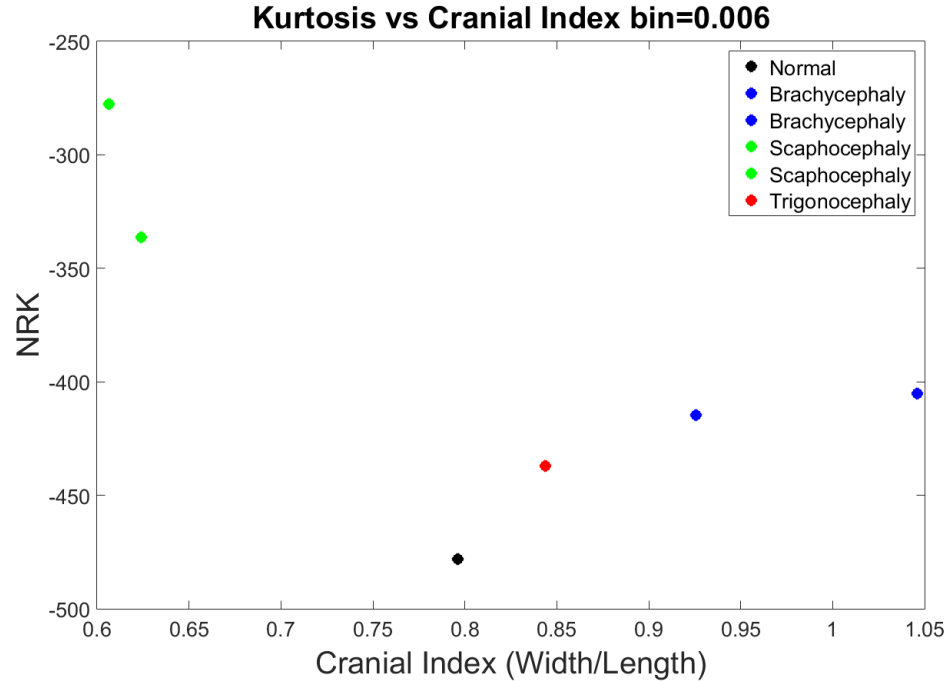


Figure 4.14: The measurements of skull shapes with bin=0.008.

4.5.1.4 System Testing

We added test data into our system to investigate its stability. To compare, we also provided the results with bin=0.008, which is a good indication between types of craniosynostosis without training data (shown in previous section). In Figure 4.15 to 4.16, we added three scaphocephaly and four trigonocephaly patients, which bin values are 0.005 and 0.008 respectively. The results shown in Figure 4.16 (bin=0.008) classify the types of craniosynostosis well except the two scaphocephaly cases that overlapped with the values of trigonocephaly cases. Again, although the trigonocephaly cases obtain very similar shape indices, they were still unexpectedly higher than brachycephaly cases. We confirmed that bin=0.005 was optimum in our evaluating system since the skull shapes spread in the

Figure in a manner that generally, the further a cranial index deviates from the normal case, the further the corresponding NRK deviates from the value of normal.

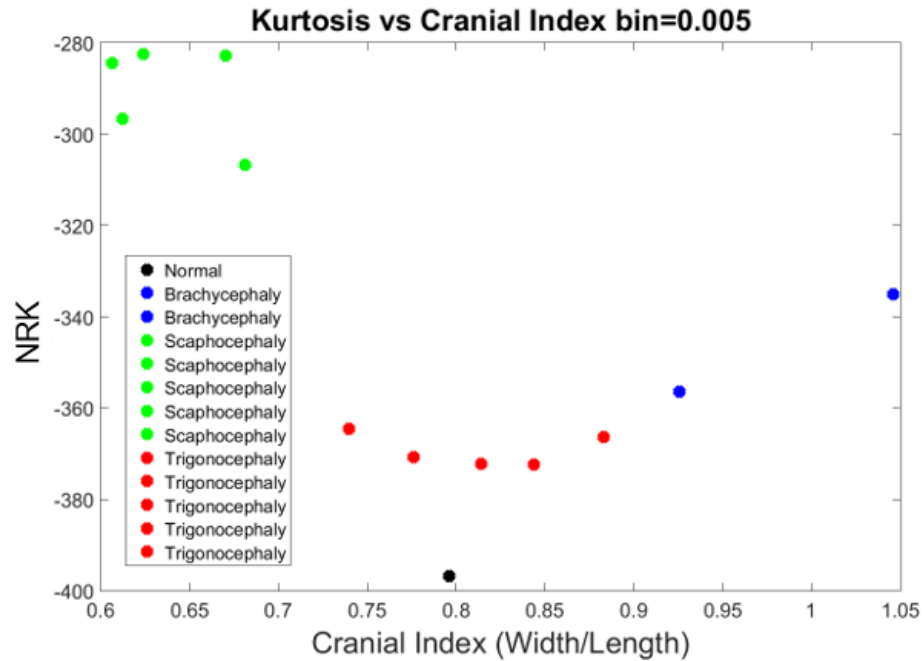


Figure 4.15: The measurements of skull shapes from test data with bin=0.005.

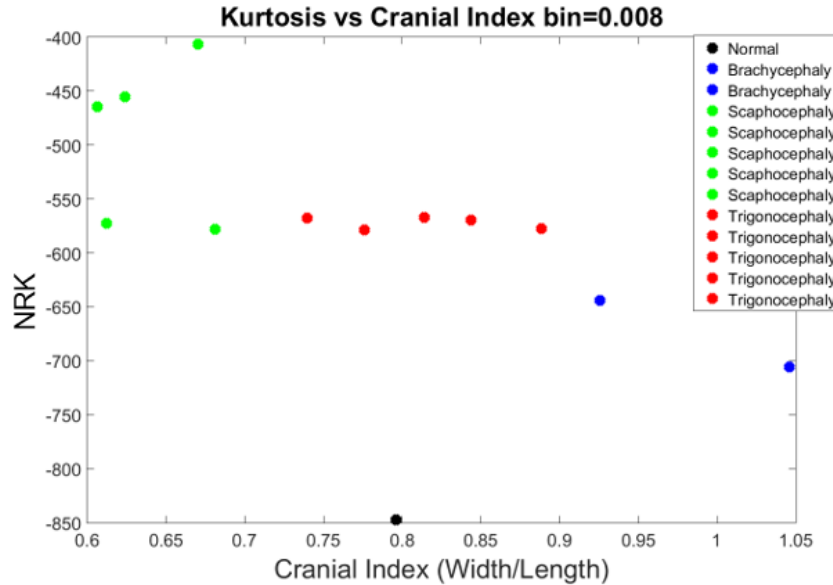


Figure 4.16: The measurements of skull shapes from test data with bin=0.008.

With the confirmation of system with bin=0.005, we further added one untypical trigonocephaly and two anterior-plagiocephaly patients. In Figure 4.17, the red dot that is pointed by a blue arrow was the untypical trigonocephaly patient. We also provided a top view of this skull on the right side of Figure 4.18, compared with a typical trigonocephaly skull shown in the left side of the same Figure. We know that a typical trigonocephaly patient should have a triangular forehead as seen in the left skull image of Figure 4.18, whereas the forehead of the skull on the right side of Figure 4.18 looks normal. We can only see the deformity from the side view of this skull in Figure 4.19, and the neurosurgeon diagnosed this skull as a mild trigonocephaly. Looking back to Figure 4.17, the cranial index of this patient is 0.812, which is considered in the normal range, and the NRK is lower than the values of the typical trigonocephaly cases. Therefore, our evaluating system indicated this case as a mild trigonocephaly case which matched the truth.

The purple dot, which was close to one of the brachycephaly skull shapes (blue dots), was denoted as “plagiocephaly case one”. Figure 4.20 shows the top view of this skull shape, whereas the left side is from the brachycephaly patient (blue dot) that is very close to the plagiocephaly case in Figure 4.17. We can see from Figure 4.20 that both skulls have similar shapes, which are both flat and short. In addition, these two skulls have similar cranial index values indicated in Figure 4.17, and therefore their shape indices are anticipated to be close.

The skull measurements of the second plagiocephaly patient (the other purple dot) can be found in the trigonocephaly region, surrounded by the red dots in Figure 4.17. We provide the top view of this skull shape in the right side of Figure 4.21, and the top view of the first plagiocephaly skull shape at the left side. To compare, we can see the level of deformity of this second plagiocephaly skull is much less severe than the first one, and the value of cranial index is 0.83 that is close to our normal case. As a result, it makes sense that the NRK of this patient is lower than the first plagiocephaly case and much closer to the normal patient.

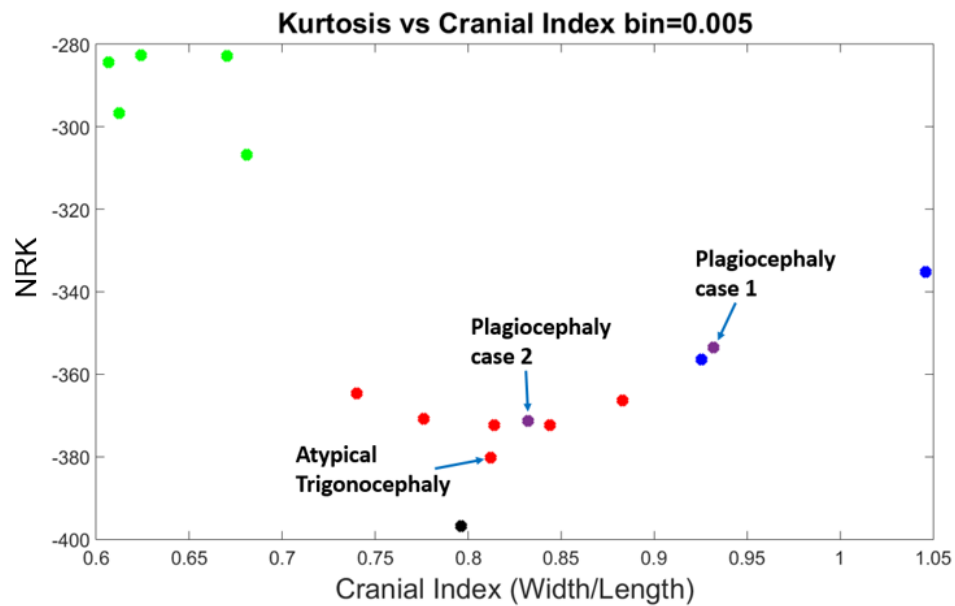


Figure 4.17: The quantified results of skull shapes with new data added.

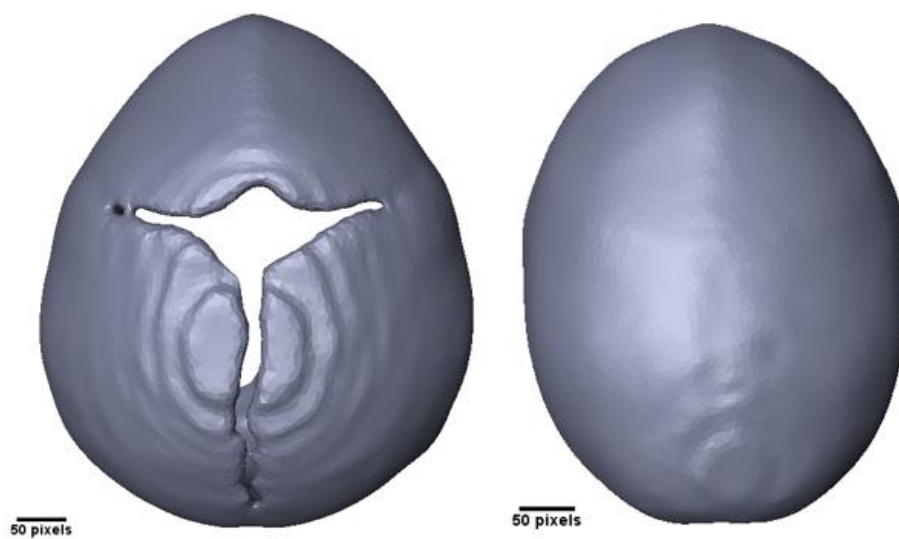


Figure 4.18: Top view of trigonocephaly skulls, the left one is a typical shape and the right one is an untypical case.

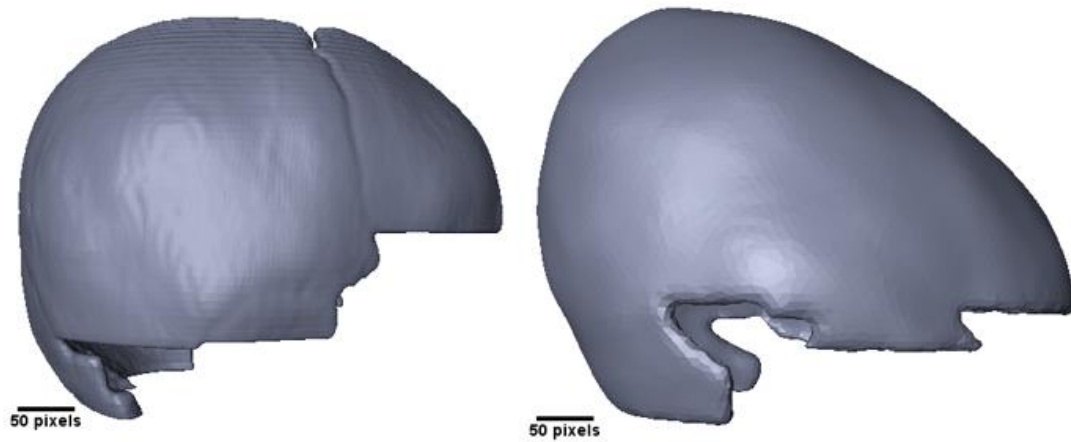


Figure 4.19: Side view of trigonocephaly skulls, the left one is a typical shape and the right one is an untypical case.

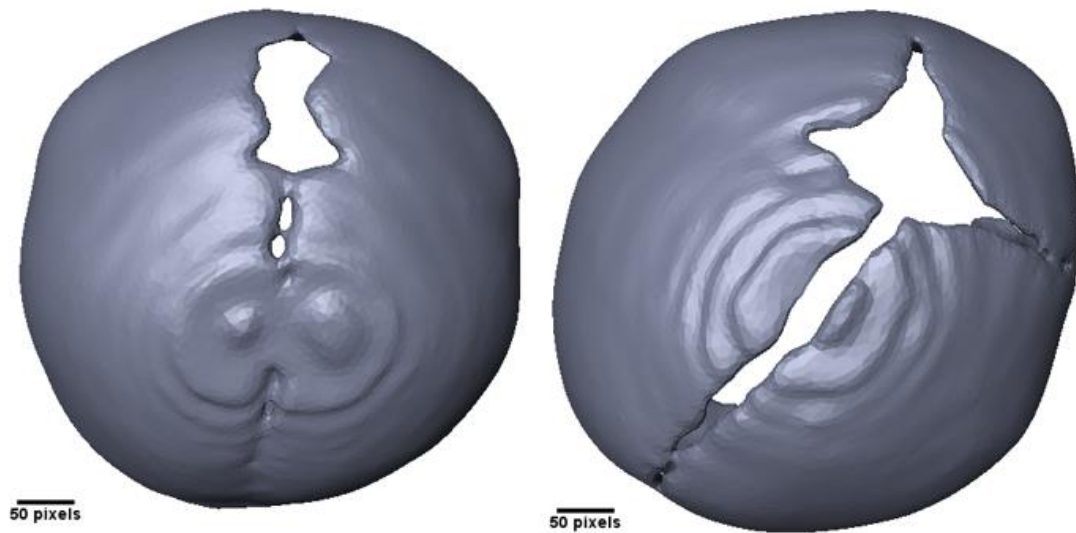


Figure 4.20: Comparison of skull shapes from top view, the left one is from a brachycephaly patient and the right one is from plagiocephaly case 1.

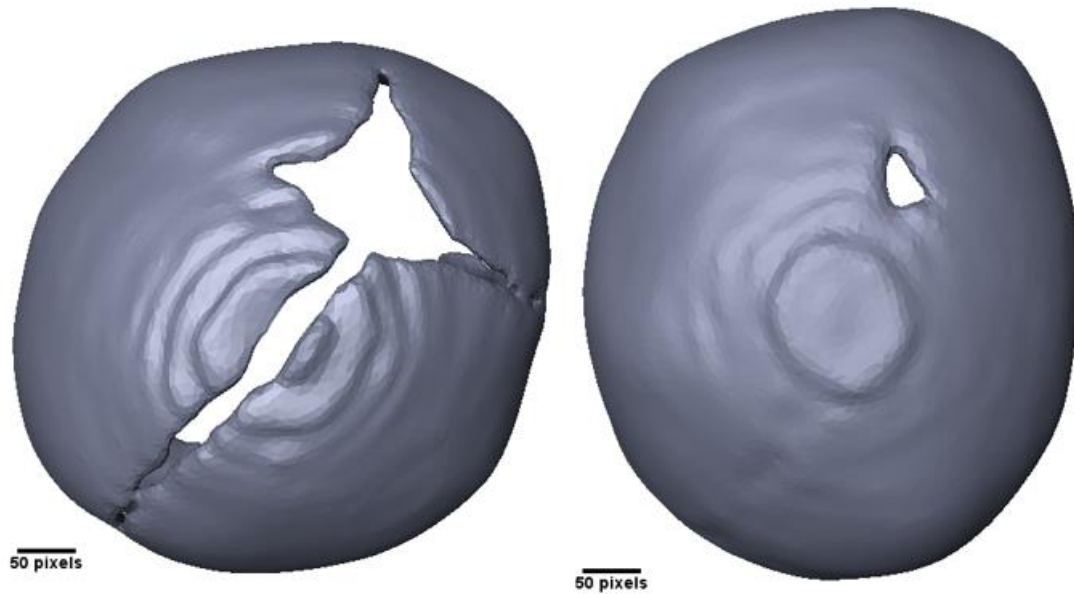


Figure 4.21: Comparison of skull shapes from top view, the left one is from plagiocephaly case 1 and the right one is plagiocephaly case 2.

4.5.2 Result Discussions

(M. M. Cohen and MacLean 2000) categorized skull shapes into four types on the basis of CI: dolichocephaly if $CI \leq 75.9$; mesocephaly while CI is between 76.0 and 80.9; CI from 81.0 to 85.4 is defined as brachycephaly; hyper-brachycephaly if $CI \geq 85.5$. a typical head shape for scaphocephaly (long head) would most likely be dolichocephaly, and the CI of a typical brachycephaly head ought to be higher than 85.5. This validated our algorithm to calculate CI from Figure 4.22, where the CI of all the scaphocephaly cases was lower than 0.7 and the CI of the two brachycephaly cases was higher than 0.9.

On the other hand, not all the shapes that are categorized into dolichocephaly, brachycephaly and hyper-brachycephaly are pathological head shapes. An average CI of

81.45±7.98 (4-6 months) and 83.15±7.98 (7-12 months) were obtained respectively by (Likus et al. 2014) from 35 (4-6 months) and 53 (7-12 months) Polish children, who were diagnosed as having normal head shapes. They claimed that according to their research, although mesocephaly is the dominant head shape among children with normal head development, other head types present as well, especially brachycephaly. (Hummel and Fortado 2005) had similar statistical results from US infants to (Likus et al. 2014). (Wolański et al. 2013) stated in their paper that the CI for infants between newly born to 6 months is 83.75±7.25, whereas (Dekaban 1977) concluded the average CI for infants within 12 months is 78.36. In addition, some skull shapes may combine several types of features, such as a trigonocephaly patient with brachycephaly head shape (the red dot in Figure 4.22 with CI of 0.88). As a consequence, for each type of skull shape (for CI values), we would expect an area on our 2D output Figure distributed by diverse cases of one type of craniosynostosis, which reasonably overlaps with areas of other types (dashed ellipses in Figure 4.22). With more data added, we expect each area will be enlarged.

Although we only have one normal case in our database, this normal head shape was a mesocephaly that is the most common head shape. As the middle point among all the CI values, we considered this normal head to be our standard head shape. Ideally, if any pathological head restores back to this shape, we regarded the associated surgery as very effective for this patient. We would expect that other normal shapes would probably be distributed around within the black dashed circle shown in Figure 4.22.

The shape indices in our research were interpreted as the summary of a head's local shapes, and the level of deformity of a skull shape from our normal shape. Generally, we assumed that the further the CI value deviates from our normal case, the higher level of deformity

in the skull. The results in Figure 4.22 validated our assumption, which also matches the research from (Ruiz-Correa et al. 2006), which measured the severity of scaphocephaly heads. They found that the CI statistically has positive linear correlation with their severity measurement of scaphocephaly head shapes. Therefore, the overlapped regions could also be explained in that some skull shapes might be very similar although from different types of craniosynostosis, or the same level of deformity but with different head shape.

However, the shape indices could fluctuate given some factors. Let's take two scaphocephaly cases as an example, which are indicated by Case 1 and Case 2 respectively in Figure 4.22. The CI of these two cases were very close, but the shape indices had a gap between. We provided the curvature distributions on these two skulls in Figure 4.23 with a color map of curvature, showing from blue as 0 to red as higher than 0.1. From the top view, Case 1 had a short and wide forehead and the width started to decrease at the back part, whereas the width of Case 2 basically the same across the skull. Therefore, the difference of local shapes could result in the discrepancy of shape indices while the CI values are the same. In addition, Case 1 had more high values (more yellow and red color) of curvatures than Case 2, especially along the edges of open areas and on the middle line. We excluded curvature values that were higher than 0.1 from our shape quantification algorithm. As a result, less curvature values in Case 1 contributed to the skull shape evaluation, also leading to a higher NRK than it should have been. However, these two situations can not be controlled.

In summary, for each common type of skull shape, we evaluated the level of deformity of a skull shape in such a way that the further a cranial index deviates from the normal patient, the further its NRK deviates from the normal. From another perspective, with similar

cranial index and the same type of shape, the shape indices are varied by the local shapes and the length of skull edges (caused by open areas). With this evaluating algorithm, we are able to evaluate a craniostylosis surgery by inputting the skull measurements of a patient from different periods in that patient's life. Ideally, we anticipate that an effective surgery should have such a pattern that for postoperative skull shapes of the patient, the corresponding shape indices and/or cranial indices should be shifted closer and closer to our golden standard normal shape over time compared to his/her preoperative skull shape.

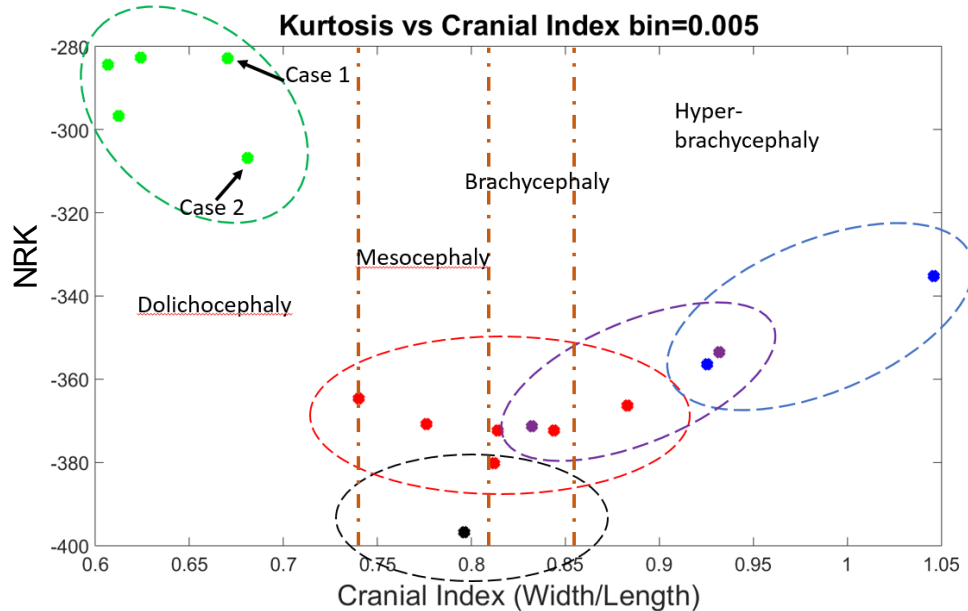


Figure 4.22: An indication of expected areas of shape results for each type of skull shapes.

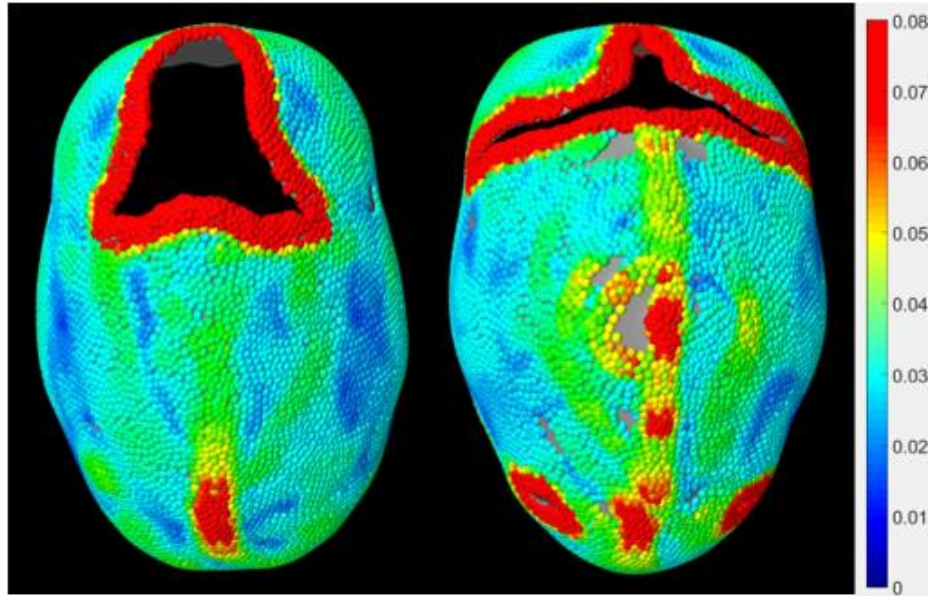


Figure 4.23: A comparison of local shapes between two scaphocephaly patients (right is case 1 and left is case 2), indicated by color map of curvature values showing from blue as 0 to red as higher than 0.1.

4.5.3 Surgical Assessments

Mentioned in the discussion of previous section, we anticipate to compare a series of CT scans (ideally three) for one patient in order to evaluate a surgery of craniosynostosis, which would involve one preoperative and two postoperative CT images. However, in our database, the voxels of the CT images that took right after the surgery were too big to develop to a smoothed surface mesh, which usually were $0.49\text{mm} \times 0.49\text{mm} \times 5\text{mm}$. Therefore, in this section, we only compared two skull shapes for each patient, which were one preoperative and one postoperative (with approximately one-year skull development) CT scans. All the results from our system were consistent with an expert neurosurgeon's opinion.

4.5.3.1 Scaphocephaly Surgeries

From the database we have, there were two scaphocephaly patients with available postoperative CT scans (one year after surgery), which we used to evaluate the surgery with our algorithm.

In Figure 4.24, we indicate this patient with magenta color, where the “*” shape represents the preoperative skull shape and the “+” shape denotes the postoperative skull shape. We kept all the preoperative results in our database especially the normal case for comparison. Preoperatively, the cranial index of this patient is 0.61 and the NRK value is -296.7, whereas postoperatively, the cranial index rise to 0.72 and the NRK drop to -363.7. It indicates a very good sign for this surgery that both cranial index and shape indices are shifted toward the normal shape. Therefore, we conclude by our evaluating system that this surgery for this patient is effective.

In Figure 4.25, we show an evaluation of another scaphocephaly surgery, which postoperative skull shape also moves toward to normal shape. The value of cranial index moves from 0.68 to 0.71 and the NRK becomes to -326.8 from -308.6. However, it is obvious that the postoperative skull only moves a relative small distance compared to previous surgery. Therefore, we conclude that the surgery for the first patient is much effective than the surgery for the second scaphocephaly patient.

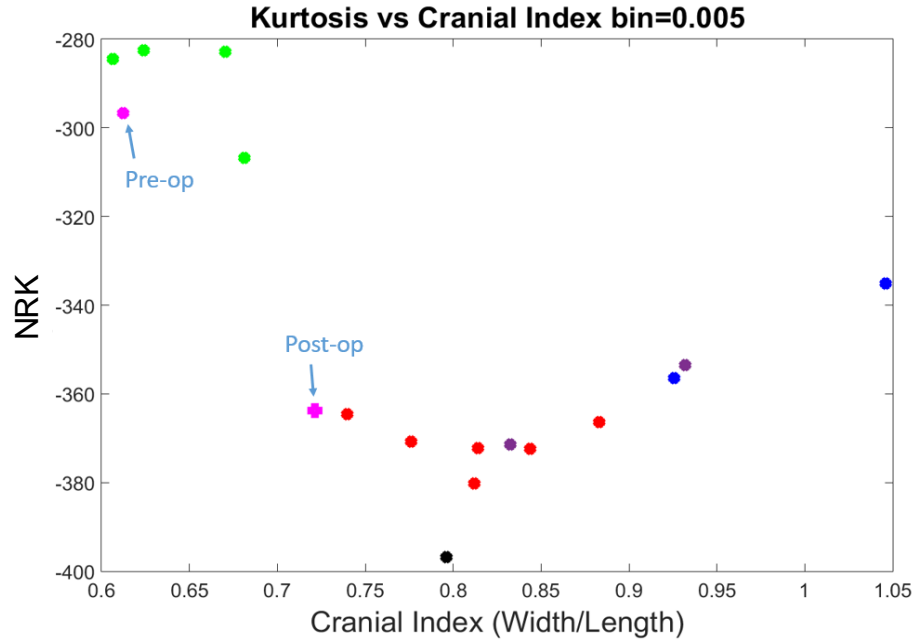


Figure 4.24: Surgical evaluation of a scaphocephaly case with one preoperative and one postoperative skull shapes.

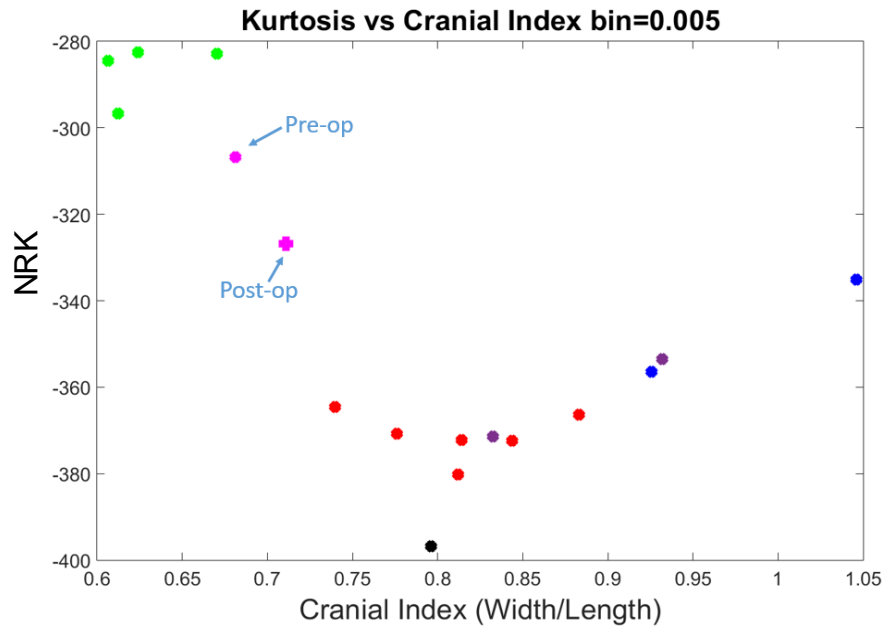


Figure 4.25: Surgical evaluation of another scaphocephaly patient with one preoperative and one postoperative skull shapes.

4.5.3.2 A Trigenocephaly Surgery

Figure 4.26 denotes our assessment of a trigonocephaly surgery through our evaluating system. The value of cranial index is 0.8 and the NRK is -362.8 preoperatively, whereas the cranial index decreases to 0.78 and the NRK drops to -381.2 postoperatively. The cranial index is kept in the range of normal values and the NRK shifts toward to normal value. The result demonstrates that this surgery restored the skull shape back normal shape to a level that the trigonocephaly became mild.

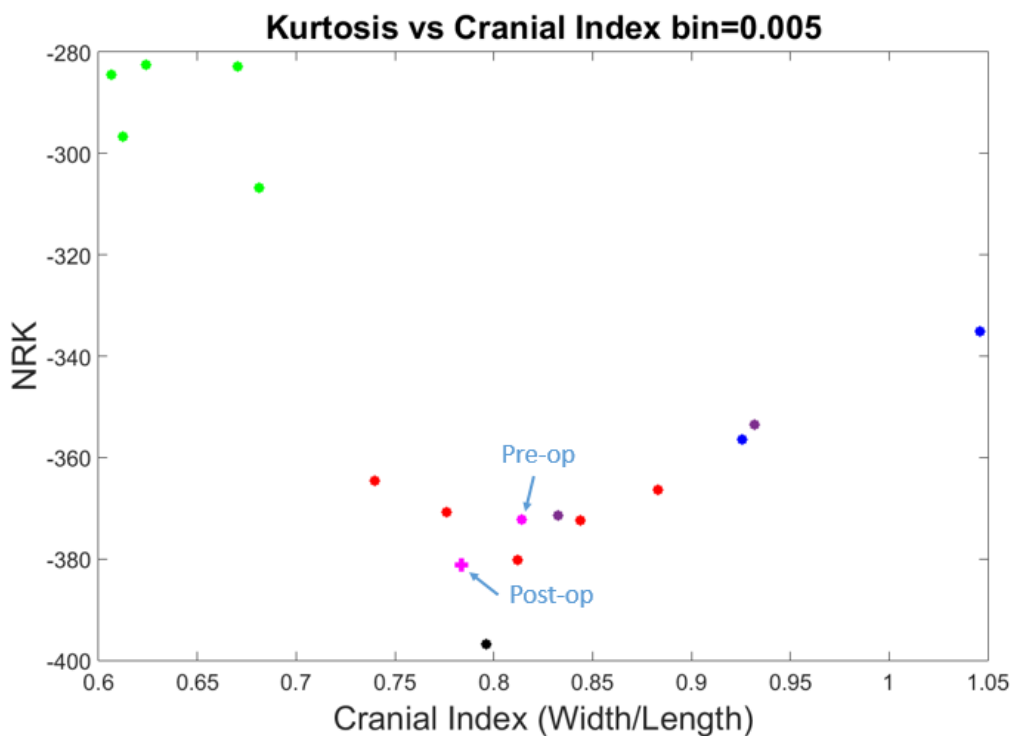


Figure 4.26: Surgical evaluation of a trigonocephaly patient with one preoperative and one postoperative skull shapes.

4.5.3.3 A Brachycephaly Surgery

Figure 4.27 indicates a surgery to treat a brachycephaly patient. The cranial index of this patient changes a lot from 0.92 to 0.82, which falls back to normal range. The NRK falls to -377.1 from -356.4, which also shifts toward our standard normal shape. As a result, we can conclude that this surgery is effective to this brachycephaly patient.

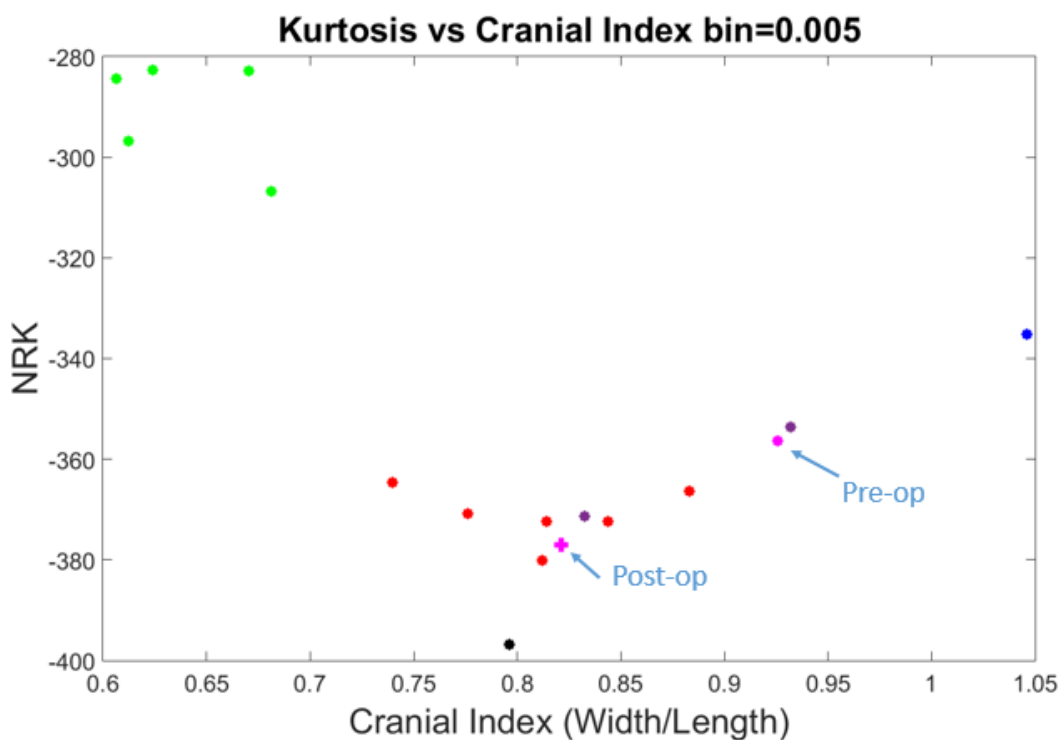


Figure 4.27: Surgical evaluation of a brachycephaly patient with one preoperative and one postoperative skull shapes.

4.5.3.4 Anterior Plagiocephaly Surgeries

Figure 4.28 indicates a surgery for a mild anterior plagiocephaly patient. Preoperatively, the skull shape of this patient is with 0.83 of the cranial index and -371.4 of the NRK.

One year after surgery, the cranial index becomes to 0.79 and the NRK shifts to -385.9, which is much closer to the normal point compared to the preoperative point.

Consequently, this surgery is considered as ideal to this patient.

On the contrary, Figure 4.29 demonstrates that the postoperative skull shape has higher level of deformity compare to preoperative skull. The value of cranial index of the postoperative skull does not change a lot while the NRK goes up sharply. We looked at the 3D images of both skulls to validate our result and confirmed with expert. This surgery did result to worse skull deformity. Even though the tilted forehead has been corrected (Figure 4.30), but the skull shape ended up with another form of deformity. The forehead was shorter than before, and the back of the skull became flatter.

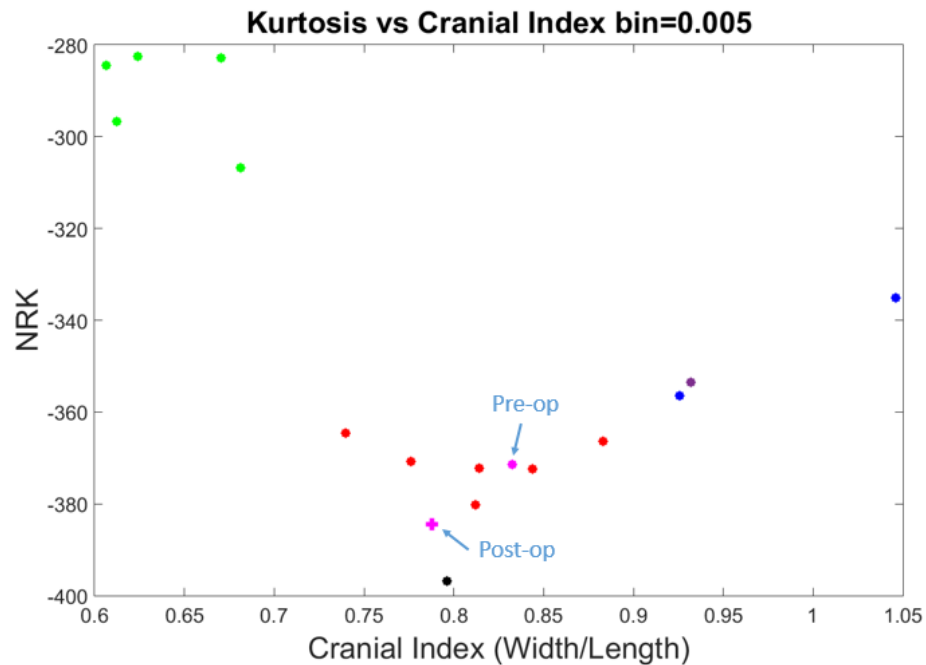


Figure 4.28: Surgical evaluation of a plagiocephaly patient with one preoperative and one postoperative skull shapes.

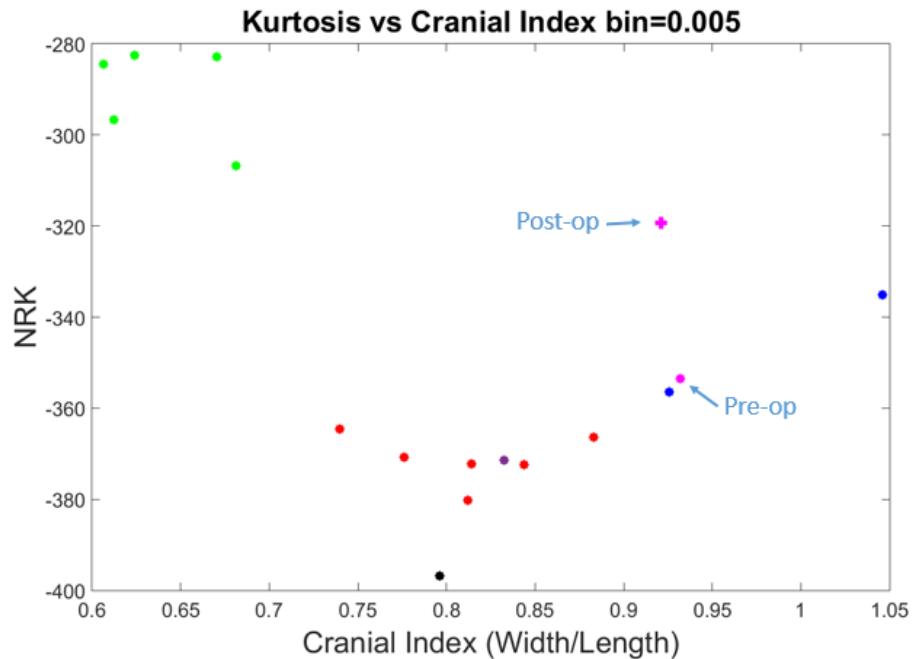


Figure 4.29: Surgical evaluation of another plagiocephaly patient with one preoperative and one postoperative skulls.

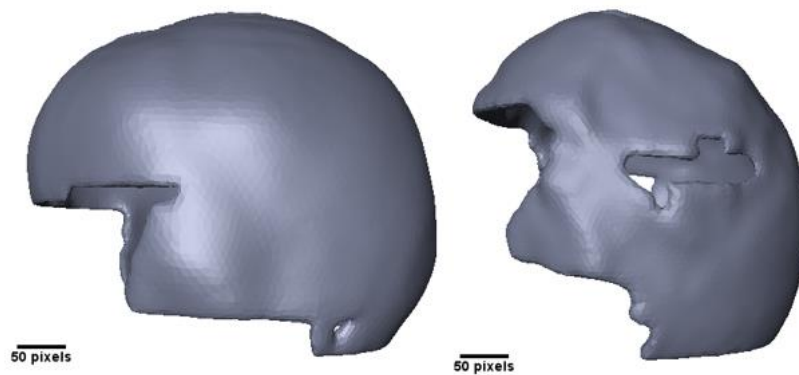


Figure 4.30: Skull shapes with color map of curvature values, showing from blue as 0 to red as higher than 0.1. The left skull was taken preoperatively and the right one was postoperative.

4.5.4 Conclusions and Future Work

The key idea of our modeling presented herein measurement is to calculate a full curvature distribution function based on local curvature across the skull model, which was based on the structure and distribution of vertices and faces of the surface mesh. Therefore, the way that how a surface mesh of a skull model was constructed plays a significant role in curvature calculation. We designed several algorithms of mesh simplification, attempting to represent all the skull shapes similarly, where the area of the faces distributed on the skull plates should be normalized to the same magnitude. With experiments, we found that maintaining the number of vertices of the skull shapes in the same type of craniosynostosis was the optimal way to characterize the difference between each types.

However, there are some issues that might generate noises in our results. Figure 4.31 indicates two scaphocephaly skulls taken from different patients. The left one has a huge open area on the frontal bone whereas the right skull has no open area at all. Although these two skull were modeled with similar number of vertices, but more vertices in the left skull were contributed to the skull edges (red dots), which were excluded from our calculation. This finally lead to a difference between the number of available vertices in our calculation. In addition, the skull surface of the left one was less smooth than the right one, resulting from the resolution of the CT images. This made the curvature values of the left skull higher than unexpected, which also increased the error of the measurement of the skull shape. This is also the reason that we obtained an unexpected high NRK for the postoperative skull shape shown in Figure 4.31.

Despite the resolution of the CT images, a lot of postoperative skulls were rough since the skull was regrouped by pieces, which lead to discontinuous curvature values while calculating the distribution. Furthermore, there were a lot empty spaces on some postoperative skull, which were left on purpose to allow proper brain expansion. All of these produce modeling noise and uncertainty on the skull surface that might affect the evaluation of skull shapes. Amira software provide tools to smooth the surface, which was only able to filter high frequency noises. The low frequency noises were maintained or even amplified after smoothness.

In addition, we used tools supported in Amira software to simplify and smooth our skull models, which can only be reduced by the number of faces. Therefore, it is complex to maintain the number of vertices of a mesh since we cannot control it directly.

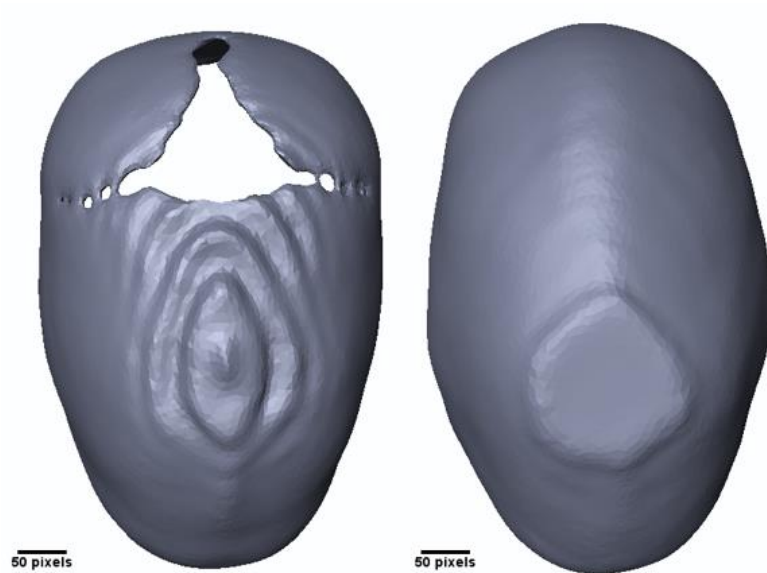


Figure 4.31: Top view of two scaphocephaly skull model.

The discontinuities in the skull shapes impedes uniform construction of vertices and faces of a surface mesh. If we can fill all the open area of the skulls in a smooth way, then we are able to uniformly construct all the skull shapes effectively. We plan to use an existing skull model (no open area) as a reference, which vertices were able to be manipulated to fit other skull shapes. For the open areas on the target skull, we should find a way to fit vertices of our reference skull onto these areas continuously and smoothly. In this way, the number of available vertices will be easily kept on the same level, further more, we will improve the uniformity of skull modeling. As a result, searching for a better mesh smoothness algorithm might be a fruitful direction to improve our system.

Another issues of our current statistical model is that we did not have enough amount of patients in our database, especially patients with normal skull development. Although the shape of our normal case in our evaluation system is representative of a large population, it is critical to analyze the different abnormal modes of skull growth, with the goal of characterizing these abnormalities parametrically. As more normal cases are studied, we can better draw the area that represent diverse normal shapes, from which we might shorten the distance between a postoperative skull shape and normal. With more craniosynostosis data, we can further explore the optimum evaluating system.

Chapter 5

5 Conclusion

5.1 Overview

Craniosynostosis is a pathology in infants and in many cases requires surgery for treatment. The difficulty for neurosurgeons, who design and perform these surgeries, is that the evaluation of craniosynostosis not only depends on skull shape immediately following the surgery, but also depends on the skull development over subsequent years. Since each case is unique, it is hard to predict which skull shape will result from any specific surgical plan. Currently, some research groups have been developing automatic diagnostic systems for craniosynostosis types. No group, however, studied how to predict surgical results. In our paper, we have discussed two projects: First, the simulation of postoperative skull developments in order to predict surgical results, and second, to quantify skull shapes for surgical assessment.

5.2 The Simulation of Head Development

We aimed to develop a tool that neurosurgeons could use to evaluate the effect of alternative surgical plans on a model of a patient's skull generated by CT scans. We sought to simulate postoperative head development for surgical plan to predict surgical outcomes. In this way, craniofacial surgeons (usually a team of plastic and neurosurgeons) would be able to safely experiment with every possible surgery and choose the most appropriate one for each specific patient without ethical concern.

We have developed a normal head model from a set of CT scans of a three-week-old baby, including skull, suture and brain, which were directly associated to skull development. We used surface mesh to generate skull plates, which were considered as rigid bodies, and volumetric mesh for sutures and brain model. Mathematical models have been also developed to simulate the growth of the brain and the skull plates and the interactions between the objects.

This normal head model was able to be modified by closing any of the suture so as to simulate a specific type of craniosynostosis. We fused the frontal suture for the simulation of trigonocephaly development, the sagittal suture for scaphocephaly simulation, and one side of coronal suture for anterior plagiocephaly. Alternatively, we developed a force based simulation algorithm to substitute the brain model, reducing the simulation time from one week to a few minutes. In addition, the results of normal and abnormal head development with this algorithm were qualitatively closer to facts than our initial pressure based model.

We chose to simulate both normal and abnormal skull development in order to validate our simulation algorithms by comparing the simulation results with clinical data.

Normally, clinics use cranial index (skull width over skull length) to evaluate a skull shape, and we found one paper (Dekaban 1977; Likus et al. 2014) that provide statistics of normal skulls with cranial index. This paper collected cranial index from different patients with ages ranged from newborn to one-year-old, which gave us a perspective that how cranial index develop during the first year of human life. We were able to compare the changes of our simulation of normal head development with the data in this paper, in order to evaluate our simulation system. We did not found clinical data for pathological

skull development, but we were able to qualitatively characterize the typical skull shapes of each type of craniosynostosis, which were helpful to evaluate corresponding simulation results.

We realized that our simulation results of craniosynostosis generally matched real cases well, but the growth ratio of cranial index of our normal simulation was higher than the averaged real cases. We concluded that the major problem caused by the rigidity of our skull plates, which should have some deformity in fact. As a result, we plan to generate a deformable model, which combined all the skull plates and sutures as a whole. Different material properties will be distributed on different elements to differentiate the skull plates and sutures. We will also use another simulation platform SOFA to implement the animation of head development.

With a stabilized simulation system, we will finally apply to postoperative head development, in order to help neurosurgeons to choose an optimal surgical plan for a craniosynostosis patient.

5.3 Skull Shape Measurements

With an appropriate algorithm to quantitatively measure the skull shapes, we are able to help surgeons to evaluate any craniosynostosis surgery using a qualitative set of metrics based on the characteristic curvature distribution function. Consequently, we utilized CT images of the patients and statistical modeling to develop such an evaluation tool. While displaying the result, we would also display the results of typical normal shapes and

common types of craniosynostosis shapes, as the purpose of knowing the difference between the current result and other skull shapes.

Curvature is an intrinsic feature to describe local shape of a surface, therefore, calculating the curvature values of a skull has been decided to be the key procedure in our evaluation system. Surface mesh, which is composed of triangular faces and vertices, was adopted to generate each skull model. In addition, each vertex on the skull mesh has a curvature value according to the distribution of its neighbourhood (including vertices and faces). For each skull model, we obtained a set of curvature values, which construct the curvature distribution. We developed NRK to quantify the curvature distribution in order to discriminate the range of pathologies spanning craniosynostosis. In order to help surgeons to better view the results, we used 2D graphics to represent the results, which need two variables: NRK cranial index.

There were several steps in our algorithms that could affect the values of curvatures, including the way to simplify the skull shape, the volume of the skulls, and the bin values to construct the curvature distribution. We selected several skull shapes from different types as training data (including normal and common types of craniosynostosis), which were repeatedly inputted into our evaluating system with different approaches for those steps, in order to find a best way to quantify the difference between those skull shapes.

Our system is robust and stable if the inputted skulls have small open areas or relative short edges, which cannot be promised in a lot of cases, especially for postoperative skulls. In the future, we will try to find a method to smoothly fill the open area of a skull in order to get the result as accurate as possible. Further more, we should add more

clinical data in our training data to further tune our evaluating algorithms. With more data added, we expected that the region for each type will be expanded. Finally, we will safely apply this algorithm to evaluate surgeries by comparing preoperative and postoperative skull shapes to normal cases, to see whether and how far the postoperative skull shape shifts toward to our ideal normal shape.

References

- Aviv, R. I., E. Rodger, and C. M. Hall. 2002. "Craniosynostosis." *Clinical Radiology* 57 (2): 93–102. doi:10.1053/crad.2001.0836.
- Barone, C. M., and D. F. Jimenez. 1999. "Endoscopic Craniectomy for Early Correction of Craniosynostosis." *Plastic and Reconstructive Surgery* 104 (7): 1965-1973-1975.
- Baumer, Timothy G., Brian J. Powell, Todd W. Fenton, and Roger C. Haut. 2009. "Age Dependent Mechanical Properties of the Infant Porcine Parietal Bone and a Correlation to the Human." *Journal of Biomechanical Engineering* 131 (11): 111006–111006. doi:10.1115/1.4000081.
- Bushberg, Jerrold T. 2002. *The Essential Physics of Medical Imaging*. Lippincott Williams & Wilkins.
- Carmo, Manfredo P. Do. 1976. *Differential Geometry of Curves and Surfaces*. 1 edition. Englewood Cliffs, N.J: Prentice-Hall.
- Chen, Sheng-Gwo, and Jyh-Yang Wu. 2004. "Estimating Normal Vectors and Curvatures by Centroid Weights." *Computer Aided Geometric Design* 21 (5): 447–58. doi:10.1016/j.cagd.2004.02.003.
- Chen, Xin, and Francis Schmitt. 1992. "Intrinsic Surface Properties from Surface Triangulation." In *Computer Vision—ECCV'92*, 739–743. Springer. http://link.springer.com/content/pdf/10.1007/3-540-55426-2_83.pdf.
- Claessens, Maurice, Fons Sauren, and Jac Wismans. 2016. "Modeling of the Human Head Under Impact Conditions: A Parametric Study." Accessed June 23. <http://papers.sae.org/973338/>.
- Clemente, Carmine. 1985. *Gray's Anatomy of the Human Body*. 30 Revised & Enlarged edition. Philadelphia: Lea & Febiger.
- Coats, Brittany, and Susan S. Margulies. 2006. "Material Properties of Human Infant Skull and Suture at High Rates." *Journal of Neurotrauma* 23 (8): 1222–32. doi:10.1089/neu.2006.23.1222.
- Cohen, Meyer Michael, and Ruth E. MacLean. 2000. *Craniosynostosis: Diagnosis, Evaluation, and Management*. Oxford University Press.
- Cohen, Steven R., Ralph E. Holmes, Hal S. Meltzer, and Peter Nakaji. 2002. "Immediate Cranial Vault Reconstruction with Bioresorbable Plates Following Endoscopically Assisted Sagittal Synostectomy." *The Journal of Craniofacial Surgery* 13 (4): 578-582-584.

- Couper, Z. S., and F. G. Albermani. 2005. "Biomechanics of Shaken Baby Syndrome: Physical Testing and Numerical Modeling." In , 1:213–18. A A Balkema. <http://espace.library.uq.edu.au/view/UQ:101485>.
- Dekaban, Anatole S. 1977. "Tables of Cranial and Orbital Measurements, Cranial Volume, and Derived Indexes in Males and Females from 7 Days to 20 Years of Age." *Annals of Neurology* 2 (6): 485–491.
- Desai, Y. M. 2011. *Finite Element Method with Applications in Engineering*. Pearson Education India.
- Desbrun, Mathieu, Mark Meyer, Peter Schröder, and Alan H. Barr. 1999. "Implicit Fairing of Irregular Meshes Using Diffusion and Curvature Flow." In *Proceedings of the 26th Annual Conference on Computer Graphics and Interactive Techniques*, 317–324. ACM Press/Addison-Wesley Publishing Co. <http://dl.acm.org/citation.cfm?id=311576>.
- Dommelen, J. A. W. van, T. P. J. van der Sande, M. Hrapko, and G. W. M. Peters. 2010. "Mechanical Properties of Brain Tissue by Indentation: Interregional Variation." *Journal of the Mechanical Behavior of Biomedical Materials* 3 (2): 158–66. doi:10.1016/j.jmbbm.2009.09.001.
- Dong, Chen-shi, and Guo-zhao Wang. 2005. "Curvatures Estimation on Triangular Mesh." *Journal of Zhejiang University SCIENCE* 6 (Suppl. I): 128–36. doi:10.1631/jzus.2005.AS0128.
- Duffy, A. J., N. J. Hogle, H. McCarthy, J. I. Lew, A. Egan, P. Christos, and D. L. Fowler. 2004. "Construct Validity for the LAPSIM Laparoscopic Surgical Simulator." *Surgical Endoscopy And Other Interventional Techniques* 19 (3): 401–5. doi:10.1007/s00464-004-8202-9.
- Dye, Frank. 2000. *Human Life Before Birth*. 1 edition. Amsterdam: CRC Press.
- Edelsbrunner, Herbert. 2001. *Geometry and Topology for Mesh Generation*. Cambridge Monographs on Applied and Computational Mathematics 6. Cambridge ; New York: Cambridge University Press.
- Ellis, Harold, and Vishy Mahadevan. 2010. *Clinical Anatomy: Applied Anatomy for Students and Junior Doctors*. 12 edition. Chichester, West Sussex ; Hoboken, NJ: Wiley-Blackwell.
- Faux, I. D., and Michael John Pratt. 1979. *Computational Geometry for Design and Manufacture*. Horwood.
- Fels, Sidney, Florian Vogt, Kees Van Den Doel, John Lloyd, Ian Stavness, and Eric Vatikiotis-Bateson. 2006. "Artisynth: A Biomechanical Simulation Platform for the Vocal Tract and Upper Airway." In *International Seminar on Speech Production, Ubatuba, Brazil*.

- Florindo, João B., André R. Backes, and Odemir M. Bruno. 2010. "Leaves Shape Classification Using Curvature and Fractal Dimension." In *Image and Signal Processing*, edited by Abderrahim Elmoataz, Olivier Lezoray, Fathallah Nouboud, Driss Mammass, and Jean Meunier, 456–62. Lecture Notes in Computer Science 6134. Springer Berlin Heidelberg.
http://link.springer.com/chapter/10.1007/978-3-642-13681-8_53.
- Ghazanfari, A., M. P. Rodriguez, E. Vigmond, and A. Nygren. 2014. "Computer Simulation of Cardiac Propagation: Effects of Fiber Rotation, Intramural Conductivity, and Optical Mapping." *IEEE Transactions on Biomedical Engineering* 61 (7): 2041–48. doi:10.1109/TBME.2014.2311371.
- Gilbert, Scott F., and Susan Singer. 2006. *Developmental Biology, Eighth Edition*. 8th edition. Sunderland, Mass: Sinauer Associates Inc.
- Gray, mary. 1997. *Modern Differential Geometry of Curves and Surfaces with Mathematica, Second Edition*. CRC Press.
- Gzik, M., W. Wolański, D. Tejszerska, B. Gzik-Zroska, M. Koźlak, D. Larysz, and M. Mandra. 2009. "Application of 3D Modeling and Modern Visualization Technique to Neurosurgical Trigenocephaly Correction in Children." In *World Congress on Medical Physics and Biomedical Engineering, September 7-12, 2009, Munich, Germany*, 68–71. Springer.
http://link.springer.com/chapter/10.1007/978-3-642-03889-1_19.
- Hartwig, Walter Carl. 2008. *Fundamental Anatomy*. Lippincott Williams & Wilkins.
- "Head Circumference for Boys, Birth to 36 Months." 2016. Accessed June 23.
<http://www.chartsgraphsdiagrams.com/HealthCharts/head-circum-birth-36-boys.html>.
- Hermann, Christopher D., Megan A. Richards, Rene Olivares-Navarrete, Joseph K. Williams, Robert E. Guldberg, Oskar Skrinjar, Zvi Schwartz, and Barbara D. Boyan. 2012. "Algorithm to Assess Cranial Suture Fusion with Varying and Discontinuous Mineral Density." *Annals of Biomedical Engineering* 40 (7): 1597–1609. doi:10.1007/s10439-012-0520-9.
- Hua, Zhen, Zilong Huang, and Jinjiang Li. 2015. "Mesh Simplification Using Vertex Clustering Based on Principal Curvature." *International Journal of Multimedia and Ubiquitous Engineering* 10 (9): 99–110. doi:10.14257/ijmue.2015.10.9.11.
- Hummel, Pat, and Dana Fortado. 2005. "Impacting Infant Head Shapes." *Advances in Neonatal Care: Official Journal of the National Association of Neonatal Nurses* 5 (6): 329–40. doi:10.1016/j.adnc.2005.08.009.
- Jimenez, D. F., and C. M. Barone. 1995. "The Sunrise Technique: The Correction of Occipital Plagiocephaly Using Bandeau Occipital Plate and Radial Osteotomies." *Pediatric Neurosurgery* 22 (3): 162–66. doi:10.1159/000120895.

- Jimenez, David F., Constance M. Barone, Cathy C. Cartwright, and Lynette Baker. 2002. "Early Management of Craniosynostosis Using Endoscopic-Assisted Strip Craniectomies and Cranial Orthotic Molding Therapy." *Pediatrics* 110 (1): 97–104.
- Johnson, David, and Andrew O. M. Wilkie. 2011. "Craniosynostosis." *European Journal of Human Genetics* 19 (4): 369–76. doi:10.1038/ejhg.2010.235.
- Kahn, Charles E., John A. Carrino, Michael J. Flynn, Donald J. Peck, and Steven C. Horii. 2007. "DICOM and Radiology: Past, Present, and Future." *Journal of the American College of Radiology: JACR* 4 (9): 652–57. doi:10.1016/j.jacr.2007.06.004.
- Kawata, Yoshiki, Noboru Niki, Hironobu Ohmatsu, Masahiko Kusumoto, Ryutaro Kakinuma, Kiyoshi Mori, Hiroyuki Nishiyama, Kenji Eguchi, Masahiro Kaneko, and Noriyuki Moriyama. 1999. "Curvature-Based Characterization of Shape and Internal Intensity Structure for Classification of Pulmonary Nodules Using Thin-Section CT Images." In , 3661:541–52. doi:10.1117/12.348610.
- Kheir, Naim. 1995. *Systems Modeling and Computer Simulation, Second Edition*. CRC Press.
- Krishnamoorthy, C. S. 1995. *Finite Element Analysis: Theory and Programming*. Tata McGraw-Hill Education.
- Larsen, William J. 2002. *Anatomy: Development, Function, Clinical Correlations: Saunders Text and Review Series*. Philadelphia: Saunders.
- Larysz, D., W. Wolański, M. Gzik, and E. Kawlewska. 2011. "Virtual Planning of the Surgical Treatment of Baby Skull Shape Correction." *Modelling and Optimization of Physical Systems*, no. z. 10: 49--52.
- Likus, Wirginia, Grzegorz Bajor, Gruszczyńska, Katarzyna Ska, Jan Baron, Jarosław Markowski, et al. 2014. "Cephalic Index in the First Three Years of Life: Study of Children with Normal Brain Development Based on Computed Tomography, Cephalic Index in the First Three Years of Life: Study of Children with Normal Brain Development Based on Computed Tomography." *The Scientific World Journal, The Scientific World Journal* 2014, 2014 (February): e502836. doi:10.1155/2014/502836, 10.1155/2014/502836.
- Liu, Lu, David Raber, David Nopachai, Paul Commean, David Sinacore, Fred Prior, Robert Pless, and Tao Ju. 2008. "Interactive Separation of Segmented Bones in CT Volumes Using Graph Cut." *Medical Image Computing and Computer-Assisted Intervention: MICCAI ... International Conference on Medical Image Computing and Computer-Assisted Intervention* 11 (Pt 1): 296–304.
- Lloyd, John E., Ian Stavness, and Sidney Fels. 2012. "ArtiSynth: A Fast Interactive Biomechanical Modeling Toolkit Combining Multibody and Finite Element

- Simulation.” In *Soft Tissue Biomechanical Modeling for Computer Assisted Surgery*, 355–394. Springer.
http://link.springer.com/chapter/10.1007/8415_2012_126.
- Margulies, Susan S. 2000. “Infant Skull and Suture Properties: Measurements and Implications for Mechanisms of Pediatric Brain Injury.” *Journal of Biomechanical Engineering* 122 (4): 364. doi:10.1115/1.1287160.
- McCarthy, J. G., S. B. Glasberg, C. B. Cutting, F. J. Epstein, B. H. Grayson, G. Ruff, C. H. Thorne, J. Wisoff, and B. M. Zide. 1995. “Twenty-Year Experience with Early Surgery for Craniosynostosis: II. The Craniofacial Synostosis Syndromes and Pansynostosis--Results and Unsolved Problems.” *Plastic and Reconstructive Surgery* 96 (2): 284-295-298.
- Mendoza, Carlos S., Nabile Safdar, Kazunori Okada, Emmarie Myers, Gary F. Rogers, and Marius George Linguraru. 2014. “Personalized Assessment of Craniosynostosis via Statistical Shape Modeling.” *Medical Image Analysis* 18 (4): 635–46. doi:10.1016/j.media.2014.02.008.
- Meyer, Mark, Mathieu Desbrun, Peter Schröder, and Alan H. Barr. 2003. “Discrete Differential-Geometry Operators for Triangulated 2-Manifolds.” In *Visualization and Mathematics III*, 35–57. Springer.
http://link.springer.com/chapter/10.1007/978-3-662-05105-4_2.
- Miller, Karol, and Kiyoyuki Chinzei. 2002. “Mechanical Properties of Brain Tissue in Tension.” *Journal of Biomechanics* 35 (4): 483–90. doi:10.1016/S0021-9290(01)00234-2.
- Miller, Karol, Kiyoyuki Chinzei, Girma Orssengo, and Piotr Bednarz. 2000. “Mechanical Properties of Brain Tissue in-Vivo: Experiment and Computer Simulation.” *Journal of Biomechanics* 33 (11): 1369–76. doi:10.1016/S0021-9290(00)00120-2.
- Moore, Keith L., T. V. N. Persaud, and Mark G. Torchia. 2011. *The Developing Human: Clinically Oriented Embryology with Student Consult Online Access, 9th Edition*. 9th edition. Philadelphia, PA: Saunders.
- Moss, M. L. 1954. “Growth of the Calvaria in the Rat; the Determination of Osseous Morphology.” *The American Journal of Anatomy* 94 (3): 333–61.
 doi:10.1002/aja.1000940302.
- Nigam, Sachin, and Vandana Agrawal. 2013. “Review: Curvature Approximation on Triangular Meshes.” *International Journal of Engineering Science and Innovative Technology (IJESIT)* 2 (3): 330–339.
- Noetzel, M. J., J. L. Marsh, H. Palkes, and M. Gado. 1985. “Hydrocephalus and Mental Retardation in Craniosynostosis.” *The Journal of Pediatrics* 107 (6): 885–92.

- Oliveira, M. Elias de, H. Hallila, A. Ritvanen, P. Büchler, M. Paulasto, and J. Hukki. 2010. "Postoperative Evaluation of Surgery for Craniosynostosis Based on Image Registration Techniques." In *2010 Annual International Conference of the IEEE Engineering in Medicine and Biology*, 5620–23. doi:10.1109/IEMBS.2010.5626798.
- Opperman, L. A. 2000. "Cranial Sutures as Intramembranous Bone Growth Sites." *Developmental Dynamics: An Official Publication of the American Association of Anatomists* 219 (4): 472–85. doi:10.1002/1097-0177(2000)9999:9999<::AID-DVDY1073>3.0.CO;2-F.
- O'Toole, Robert V., Robert R. Playter, Thomas M. Krummel, William C. Blank, Nancy H. Cornelius, Webb R. Roberts, Whitney J. Bell, and Marc Raibert. 1999. "Measuring and Developing Suturing Technique with a Virtual Reality Surgical simulator1." *Journal of the American College of Surgeons* 189 (1): 114–27. doi:10.1016/S1072-7515(99)00076-9.
- Perktold, Karl, and Gerhard Rappitsch. 1995. "Computer Simulation of Local Blood Flow and Vessel Mechanics in a Compliant Carotid Artery Bifurcation Model." *Journal of Biomechanics* 28 (7): 845–56. doi:10.1016/0021-9290(95)95273-8.
- Pritchard, J. J., J. H. Scott, and F. G. Girgis. 1956. "The Structure and Development of Cranial and Facial Sutures." *Journal of Anatomy* 90 (Pt 1): 73–86.3.
- Rashid, Badar, Michel Destrade, and Michael D. Gilchrist. 2012. "Mechanical Characterization of Brain Tissue in Compression at Dynamic Strain Rates." *Journal of the Mechanical Behavior of Biomedical Materials* 10: 23–38.
- Reardon, null. 2000. "Craniosynostosis. Diagnosis, Evaluation and Management." *Journal of Medical Genetics* 37 (9): 727.
- Roth, Sébastien, Jean-Sébastien Raul, and Rémy Willinger. 2008. "Biofidelic Child Head FE Model to Simulate Real World Trauma." *Computer Methods and Programs in Biomedicine* 90 (3): 262–74. doi:10.1016/j.cmpb.2008.01.007.
- Ruiz-Correa, Salvador, Raymond W. Sze, Jacqueline R. Starr, Hen-Tzu J. Lin, Matthew L. Speltz, Michael L. Cunningham, and Anne V. Hing. 2006. "New Scaphocephaly Severity Indices of Sagittal Craniosynostosis: A Comparative Study with Cranial Index Quantifications." *The Cleft Palate-Craniofacial Journal* 43 (2): 211–221.
- Seixas-Mikelus, Stéfanie A., Thenkurussi Kesavadas, Govindarajan Srimathveeravalli, Rameela Chandrasekhar, Gregory E. Wilding, and Khurshid A. Guru. 2010. "Face Validation of a Novel Robotic Surgical Simulator." *Urology* 76 (2): 357–60. doi:10.1016/j.urology.2009.11.069.
- Soza, G, R Grosso, C Nimsky, P Hastreiter, R Fahlbusch, and G Greiner. 2005. "Determination of the Elasticity Parameters of Brain Tissue with Combined

- Simulation and Registration.” *The International Journal of Medical Robotics and Computer Assisted Surgery* 1 (3): 87–95. doi:10.1002/rcs.32.
- Sperber, Geoffrey H., Steven M. Sperber, and Geoffrey D. Guttman. 2010. *Craniofacial Embryogenetics and Development*. PMPH-USA.
- Steinbock, Bonnie. 2011. *Life Before Birth: The Moral and Legal Status of Embryos and Fetuses, Second Edition*. Oxford University Press.
- Stergiopoulos, N., D. F. Young, and T. R. Rogge. 1992. “Computer Simulation of Arterial Flow with Applications to Arterial and Aortic Stenoses.” *Journal of Biomechanics* 25 (12): 1477–88. doi:10.1016/0021-9290(92)90060-E.
- Taubin, Gabriel. 1995. “Estimating the Tensor of Curvature of a Surface from a Polyhedral Approximation.” In *Computer Vision, 1995. Proceedings., Fifth International Conference on*, 902–907. IEEE.
http://ieeexplore.ieee.org/xpls/abs_all.jsp?arnumber=466840.
- Thaller, Seth, James P. Bradley, and Joe I. Garri. 2007. *Craniofacial Surgery*. CRC Press.
- Thorpe, John A. 1994. *Elementary Topics in Differential Geometry*. Springer Science & Business Media.
- Tortora, Gerard J., and Mark Nielsen. 2010. *Principles of Human Anatomy*. 12 edition. Hoboken, NJ: Wiley.
- Vogt, Florian, Oliver Guenther, Allan Hannam, Kees van den Doel, John Lloyd, Leah Vilhan, Rahul Chander, et al. 2005. “ArtiSynth Designing a Modular 3D Articulatory Speech Synthesizer.” *The Journal of the Acoustical Society of America* 117 (4): 2542–2542. doi:10.1121/1.4788447.
- Walker, Marcus A, Christopher D Hermann, Joseph K Williams, Brani Vidakovic, Rene Olivares-Navarrete, Zvi Schwartz, and Barbara D Boyan. 2016. “Automated Analysis and Predictive Modeling of Craniosynostosis with Cranial Suture Measurements and Intracranial Volume Asymmetries Using the Snake Algorithm.” *Journal of Biomedical Engineering and Informatics* 2 (2). doi:10.5430/jbei.v2n2p132.
- Wijk van Brievingh, Rogier P. van, and Dietmar P. F. Möller, eds. 1993. *Biomedical Modeling and Simulation on a PC*. Vol. 6. Advances in Simulation. New York, NY: Springer New York. <http://link.springer.com/10.1007/978-1-4613-9163-0>.
- Williams, J. K., S. R. Cohen, F. D. Burstein, R. Hudgins, W. Boydston, and C. Simms. 1997. “A Longitudinal, Statistical Study of Reoperation Rates in Craniosynostosis.” *Plastic and Reconstructive Surgery* 100 (2): 305–10.
- Wolański, Wojciech, Dawid Larysz, Marek Gzik, and Edyta Kawlewska. 2013. “Modeling and Biomechanical Analysis of Craniosynostosis Correction with the

Use of Finite Element Method: MODELING AND BIOMECHANICAL ANALYSIS OF CRANIOSYNOSTOSIS CORRECTION.” *International Journal for Numerical Methods in Biomedical Engineering* 29 (9): 916–25. doi:10.1002/cnm.2506.

Zhang, Xi, Guiqing Li, Yunhui Xiong, and Fenghua He. 2008. “3D Mesh Segmentation Using Mean-Shifted Curvature.” In *Advances in Geometric Modeling and Processing*, edited by Falai Chen and Bert Jüttler, 465–74. Lecture Notes in Computer Science 4975. Springer Berlin Heidelberg. http://link.springer.com/chapter/10.1007/978-3-540-79246-8_35.

"Amira 5 User's Guide." (n.d.): n. pag. [Http://www2.udel.edu/ctcr/sites/udel.edu.ctcr/files/Amira%20Users%20Guide.pdf](http://www2.udel.edu/ctcr/sites/udel.edu.ctcr/files/Amira%20Users%20Guide.pdf). Web.

Appendices



**Western
Research**

Research Ethics

Western University Health Science Research Ethics Board HSREB Annual Continuing Ethics Approval Notice

Date: August 19, 2016

Principal Investigator: Sandrine de Ribaupierre

Department & Institution: Schulich School of Medicine and Dentistry/Clinical Neurological Sciences, Western University

Review Type: Delegated

HSREB File Number: 102918

Study Title: Retrospective chart review (2007-2012) of patients with craniosynostosis to compare pre- and post-operative intracranial skull volume changes using 3D CT co-registration

HSREB Renewal Due Date & HSREB Expiry Date:

Renewal Due -2017/08/31

Expiry Date -2017/09/06

The Western University Health Science Research Ethics Board (HSREB) has reviewed the Continuing Ethics Review (CER) Form and is re-issuing approval for the above noted study.

The Western University HSREB operates in compliance with the Tri-Council Policy Statement Ethical Conduct for Research Involving Humans (TCPS2), the International Conference on Harmonization of Technical Requirements for Registration of Pharmaceuticals for Human Use Guideline for Good Clinical Practice (ICH E6 R1), the Ontario Freedom of Information and Protection of Privacy Act (FIPPA, 1990), the Ontario Personal Health Information Protection Act (PHIPA, 2004), Part 4 of the Natural Health Product Regulations, Health Canada Medical Device Regulations and Part C, Division 5, of the Food and Drug Regulations of Health Canada.

Members of the HSREB who are named as Investigators in research studies do not participate in discussions related to, nor vote on such studies when they are presented to the REB.

The HSREB is registered with the U.S. Department of Health & Human Services under the IRB registration number IRB 00000940.

Ethics Officer, on behalf of Dr. Joseph Gilbert, HSREB Chair

Ethics Officer: Erika Basile ___ Katelyn Harris ___ Nicole Kaniki Grace Kelly ___ Vikki Tran ___ Karen Gopzel ___



Use of Human Participants - Ethics Approval Notice

Principal Investigator: Sandrine de Ribaupierre
 File Number: 102918
 Review Level: Delegated
 Approved Local Adult Participants: 50
 Approved Local Minor Participants: 0
 Protocol Title: Retrospective chart review (2007-2012) of patients with craniosynostosis to compare pre- and post-operative intracranial skull volume changes using 3D CT co-registration
 Department & Institution: Schulich School of Medicine and Dentistry/Clinical Neurological Sciences, Western University
 Sponsor:
 Ethics Approval Date: September 16, 2013 Expiry Date: August 01, 2015

Documents Reviewed & Approved & Documents Received for Information:

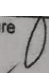
Document Name	Comments	Version Date
Revised Study End Date	The study end date has been extended to August 31, 2015 to allow for project completion.	

This is to notify you that The University of Western Ontario Research Ethics Board for Non-Medical Research Involving Human Subjects (NMREB) which is organized and operates according to the Tri-Council Policy Statement: Ethical Conduct of Research Involving Humans and the applicable laws and regulations of Ontario has granted approval to the above referenced revision(s) or amendment(s) on the approval date noted above.

This approval shall remain valid until the expiry date noted above assuming timely and acceptable responses to the NMREB's periodic requests for surveillance and monitoring information.

Members of the NMREB who are named as investigators in research studies, or declare a conflict of interest, do not participate in discussions related to, nor vote on, such studies when they are presented to the NMREB.

The Chair of the NMREB is Dr. Riley Hinson. The NMREB is registered with the U.S. Department of Health & Human Services under the IRB registration number IRB 00000941.

Signature 

Ethics Officer to Contact for Further Information

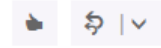
<input checked="" type="checkbox"/> Grace Kelly (grace.kelly@uwo.ca)	<input type="checkbox"/> Vikki Tran (vikki.tran@uwo.ca)	<input type="checkbox"/> Erika Basile (ebasile@uwo.ca)
---	--	---

This is an official document. Please retain the original in your files.

Permission to Use Copyrighted Material in a Doctoral/Master's Thesis



scs@scs.org
Today, 3:01 PM



Hello Jing Jin,

Yes you may have permission to use our copyrighted material for your paper.

All the best,
SCS Admin.



Jing Jin

Today, 10:56 AM

scs@scs.org



Reply all | v

Sent Items

Dear:

I am a University of Western Ontario graduate student completing my Doctoral thesis entitled "Evaluation system for craniosynostosis surgeries with computer simulation and statistical modeling". My thesis will be available in full-text on the internet for reference, study and / or copy. Except in situations where a thesis is under embargo or restriction, the electronic version will be accessible through the Western Libraries web pages, the Library's web catalogue, and also through web search engines. I will also be granting Library and Archives Canada and ProQuest/UMI a non-exclusive license to reproduce, loan, distribute, or sell single copies of my thesis by any means and in any form or format. These rights will in no way restrict republication of the material in any other form by you or by others authorized by you.

I would like permission to allow inclusion of the following pictures of my paper that published in your journal in 2013: Figure 1 to 9 in the paper titled: "Hybrid simulation of brain-skull growth."

© 2013 The Society for Modeling and Simulation International

DOI: 10.1177/0037549713516691

The material will be attributed through a citation.

Please confirm by email that these arrangements meet with your approval.

Sincerely
Jing Jin

Curriculum Vitae

Name: Jing Jin

Post-secondary Education and Degrees: Southern Medical University
Guangzhou, Guangdong, China
2005-2009 B.Eng.

Western University
London, Ontario, Canada
2011-2016 Ph.D.

Honours and Awards: Graduate Research Thesis Fund, UWO
2011-2016

NSERC CAMI Program Scholarship
2011- 2013

Western Graduate Research Scholarship, UWO
2011-2016

Related Work Experience Teaching Assistant, Western University

- Programming fundamentals for engineering 2011-2016
- Microprocessors and Microcontrollers 2014
- Human Computer Interface 2012
- Computer Architecture

Publications:

Jin, J., Shahbazi, S., Lloyd, J., Fels, S., Ribaupierre, S. de, & Eagleson, R. (2013). Hybrid simulation of brain–skull growth. *SIMULATION*, 37549713516691.
<http://doi.org/10.1177/0037549713516691>

Jin, J., De Ribaupierre, S., & Eagleson, R. (2016). Normal Brain-Skull Development with Hybrid Deformable VR Models Simulation. *Studies in Health Technology and Informatics*, 220, 150–153.

Jin, J., De Ribaupierre, S., & Eagleson, R. Skull Development with a Tensegrity Model. Submitted to “computer methods in biomechanics and biomedical engineering imaging & visualization” on July 2016.

Jin, J., Eagleson, R., & De Ribaupierre, S. Craniosynostosis Surgery Evaluation Tool with Statistical Modelling. Submitted to “computers in biology and medicine” on July 2016.

Jin, J., Eagleson, R., & De Ribaupierre, S. Assessments of Real cases from Craniosynostosis Surgeries with Skull Deformity Measurement. To be submitted.